Data-Driven Modeling and Sparse Sensing for Nuclear Energy Systems

Niharika Karnik

A dissertation
submitted in partial fulfillment of the
requirements for the degree of

Doctor of Philosophy

University of Washington

2025

Reading Committee:
Krithika Manohar, Chair
Mohammad G. Abdo
Steven L. Brunton

Program Authorized to Offer Degree:
Mechanical Engineering

University of Washington

Abstract

Data-Driven Modeling and Sparse Sensing for Nuclear Energy Systems

Niharika Karnik

Chair of the Supervisory Committee:
Krithika Manohar
Mechanical Engineering

In nuclear energy systems, the integration of computational and interpretable data-driven models is essential for ensuring the safe and efficient operation of reactors and subsystems. These models leverage real-time sensor data to reconstruct critical variables such as temperature, pressure, and velocity, enabling precise monitoring, control, and optimization. By minimizing the need for costly physical experiments, computational models allow virtual testing of designs and operational strategies while addressing uncertainties and enhancing subsystem performance. Coupled with data-driven methodologies, they form the backbone of modern nuclear engineering, facilitating real-time decision-making and ensuring robust, reliable, and efficient system operations.

Accurate reconstruction and monitoring in nuclear systems face challenges due to sensor noise and the impracticality of deploying extensive sensor arrays in harsh environments. This work addresses these limitations by introducing a data-driven framework for spatially constrained sensor placement, designed to minimize reconstruction errors and quantify noise-induced uncertainties. Using a greedy optimization algorithm, this approach ensures physically feasible configurations while maintaining high-fidelity reconstructions. These advancements are applied to critical scenarios, including fuel irradiation experiments, nuclear fuel test rod models, and steam generator subsystems, laying the groundwork for creating reliable and interpretable models for nuclear power plants (NPPs).

This work further explores the effects of power transients on reactor core coolant dynamics, developing frameworks that adapt sensor placement and sampling intervals to changing operational states. The integration of classification tools like Linear Discriminant Analysis (LDA) with DMDc enables precise identification of transient regimes, ensuring robust monitoring and control. These contributions extend beyond individual subsystems, enabling the development of comprehensive digital twins for entire NPPs. By addressing noise, spatial constraints, power perturbations and transient conditions, this work establishes a foundation for advanced monitoring and control in nuclear systems. The proposed frameworks enable proactive decision-making, enhance safety, and improve operational efficiency, contributing to a new standard for intelligent, data-driven engineering solutions in the nuclear industry.

TABLE OF CONTENTS

LIST OF FIGURES

LIST OF TABLES

ACKNOWLEDGMENTS

First and foremost, I thank my advisor, Krithika Manohar, for introducing me to data-driven techniques and guiding me throughout this journey. She opened doors to wonderful collaborations while being consistently available to discuss everything from research challenges to life's broader questions. Through her mentorship, I learned about research methodology and teaching, but more importantly, her friendship showed me that the best mentors are trusted companions who genuinely care about your growth as both a researcher and a person.

I am deeply grateful to Mohammad Abdo, who taught me research fundamentals and open-source development while inspiring my passion for data-driven techniques. He has been a constant source of support, always available to discuss both successes and setbacks throughout this journey. I am equally grateful to Andrei Klishin for his invaluable mentorship and meticulous attention to detail, from color schemes to technical writing. His enthusiasm for science is inspiring, and his consistent availability and exceptional feedback have greatly shaped my work.

The African proverb ‘ it takes a village to raise a child ’ applies equally well to research: it takes a village to produce meaningful scientific work. I thank my collaborators Samuel E. Otto, Yash Bhangale, Joshua J. Cogliati, Richard S. Skifton, Carlos E. Estrada-Perez, Jun Soo Yoo, Pattrick Calderoni, Congjian Wang, Palash K. Bhowmik, Silvino A. Balderrama Prieto, Changhu Xing, Musa Moussaoui, Charles P. Folsom, Joe J. Palmer, Piyush Sabharwall, Paul Schuck, Paul Talbot, Gabriel J. Soto Gonzalez, and Sara Ichinaga for their invaluable insights on topics ranging from greedy algorithms to thermo-hydraulic simulations. I also thank my committee members Steven L. Brunton, Santosh Devasia, Amir Taghvaei and David Shean for their timely questions and perspectives. I am forever grateful to my colleagues and lab mates Anand Krishnan, Nick Zolman, Jan Williams, Sajeda Mokbel, Prerna Patil, Doris Voina, Michelle Hickner, Sam Ahnert, Dima Tretiak, Chinmay Ratnaparkhe, and Kartik Krishna for their unwavering support, friendship, and engaging conversations spanning mathematics, science, engineering, and everything in between. Wanwisa Kisalang, Lauren Lederer, and Brenda M. Monson have been my rocks and biggest cheerleaders throughout this journey. I thank my undergraduate research advisor Dr. Pankaj Dhatrak for igniting my passion for research and continuously pushing me to excel.

The past four years in Seattle and summers in Idaho Falls have been transformative, both academically and personally. I am deeply grateful to Aditya Ashok, Nithya Chandran, Clarissa Bargellini, Uma Joshi, Aparajit Venkatesh, Srinithya Nagarajan, Priyanka Pandit, Mattia Zanotelli, Ron Gonzalez, Christa White, Nikhila Krishnan, Sushanth Kumar, Himay Nishanth, Poojita Raj, Rahul Mayuranath, Amy Santoso, Richa Asangi, Aditi Gudi, Charlie Legge, Thomas Chu, Ananya Sharma, and Kyle Miller for creating a true home away from home and for all the cherished memories we've shared together.

I owe everything to my parents, Roopak and Madhavi Karnik, for their unwavering support and for instilling in me the belief that no dream is too big. They provided me with endless opportunities to explore, fail, learn, and ultimately succeed. My grandparents, Deepak and Neeta Karnik and Parshuram and Urmila Patwardhan, have been pillars of strength throughout my life, caring for me with unconditional love and dedicating so much of themselves to my growth and well-being. To my extended family—Rohit, Dhanashree, and Eva Karnik, and Nilendra Deshpande—thank you for your constant encouragement and support. I could not have achieved this without you. Anand Krishnan, thank you for being an incredible partner through both this PhD journey and all of life's adventures.

This work was supported by the INL Laboratory Directed Research and Development (LDRD) Program through the DOE Idaho Operations Office under Contract DE-AC07-05ID14517 for LDRD-22A1059-091FP and by the NSF AI Institute in Dynamic Systems under Grant 2112085.

DEDICATION

to Baba and Momo

Chapter 1

INTRODUCTION

Sensor placement and reduced-order modeling (ROM) are critical for efficient monitoring, control, and decision-making in modern engineering systems. Optimal sensor placement ensures accurate, real-time tracking of key system variables with minimal hardware, while ROMs reduce computational complexity by approximating high-fidelity models with low-dimensional surrogates. Together, these techniques enable cost-effective, real-time system analysis and control. Their importance is magnified in nuclear engineering, where direct measurement of critical variables like reactor core temperature, coolant flow, and neutron flux is constrained by extreme conditions, limited sensor access, and safety requirements. This work develops scalable sensor placement methods for spatially constrained systems in both steady and transient regimes, incorporating uncertainty estimation from noisy sensor measurements to advance the digital twin paradigm in nuclear systems. This chapter first motivates the need for optimally placed sensors informed by data-driven reduced-order models (ROMs) within nuclear applications, and, then outlines the contributions of this work.

1.1 Motivation

Nuclear power plants (NPPs) are intricate networks of interdependent subsystems, structures, and components such as the fuel, control rods, moderators, coolants, pressurizers, heat exchangers, steam generators, and condensers. Nuclear power is inherently safety-critical, with reactor commissioning requiring rigorous testing and strict regulatory approval to ensure compliance with the highest safety standards. While non-safety system failures have minimal impact, malfunctions in critical systems can escalate if not contained. Achieving safe, optimal performance requires a comprehensive understanding of the plant's nonlinear dynamic behavior, remote monitoring, condition based maintenance, and real-time control via data streamed from physical processes, especially in advanced reactors e.g., microreactors, fission batteries, small modular reactors, and integrated energy systems. Furthermore, extreme operating conditions, high costs, limited accessibility and safety regulations, all impose significant constraints on real-world experimentation.

Modeling and simulation play a critical role in overcoming the limitations of real-world experimentation throughout the nuclear reactor lifecycle. From early design to decommissioning, computational models such as computer aided (CAD) drawings, computational fluid dynamics (CFD), structural finite element analysis (FEA), and multi-physics coupling enable the analysis of complex phenomena that physical prototypes cannot replicate. Dynamic system control, driven by these models, stabilizes operations and reduces risks by adjusting actuators based on sensor data to maintain key process variables within setpoints [1]. These simulations support failure analysis, inform safety protocols, and enhance efficiency, safety, and decision-making at every stage.

Physics-based simulations are too slow for real-time predictive maintenance, decision-making, control, and risk assessment. Fortunately, the behaviors exhibited by many complex physical systems, including neutronics, fluid flows, and structural mechanics, are dominated by coherent spatiotemporal patterns. By leveraging the natural low-dimensional patterns in these systems, high-dimensional, multi-physics simulations can train reduced-order models (ROMs) that capture essential system behavior with minimal computational effort. Furthermore, data from the entire product lifecycle is invaluable in augmenting these physics-based simulations, enabling the training of ROMs on both simulation outputs and real-world data. This highlights the critical role of data-driven techniques in bridging the gap between simulation and reality, enhancing predictive accuracy and supporting efficient decision-making. These accurate and computationally efficient models of physical systems enable critical engineering and scientific tasks, including forecasting system behavior, real-time state estimation using sensor data, control and decision-making to achieve specific objectives, solving inverse problems to determine unknown parameters, optimizing system design for performance improvement, and identifying essential system measurements required for these tasks [2].

A digital twin of a nuclear application is a high-fidelity, virtual representation of a nuclear system or process that integrates real-time data, physics-based models, and data-driven algorithms to simulate, monitor, predict, and optimize its behavior throughout its lifecycle. Reduced-order models (ROMs) power the digital twin paradigm by creating computationally efficient virtual replicas of physical systems, enabling real-time sensor data integration for predictive maintenance, operational optimization, and risk assessment. Two-way communication between digital twins and physical systems relies on sensor data to monitor key fields like reactor core temperature, coolant levels, and steam generator pressure. This data enables real-time control, anomaly detection, and accident response. Achieving a fully functional digital twin requires accurate, real-time sensor input to compare with reduced-order models (ROMs) for diagnostic insights. However, in nuclear systems, sensor capacity and real-time data streaming are often limited, especially for critical process variables like neutron distribution, pressure, and power fields, posing a significant challenge to real-time monitoring and control.

In general, sensor placement optimization is NP-hard and cannot be solved in polynomial time. There are $\binom{n}{p} = n!/((n-p)!p!)$ possible combinations of choosing p sensors from an n-dimensional state. Optimal sensor placement approaches typically optimize an objective, such as information criteria [3, 4], over feasible sets of sensor configurations, framing sensor placement as a submodular selection problem [5]. Such problems can be efficiently optimized for hundreds or thousands of candidate locations using convex [4, 6] or greedy submodular optimization approaches [5]. Sensor placement in linear time-invariant systems have been optimized using gradient descent methods with similar computational complexity [7]. However, modern nuclear and fluid simulations have millions of grid points, making such techniques computationally intractable. Leveraging ROMs to optimize sensor placement, by exploiting low-dimensional patterns in data, drastically reduces the number of sensors required for accurate reconstruction of full fields [8, 9, 10, 11, 12]. Empirical ROM interpolation methods have been successfully adapted for optimizing sensor placement to minimize reconstruction error [13, 14, 15], including under greedy cost constraints [16]. However, these methods do not admit hard constraints within reactors or predict reconstruction uncertainty under a given sensor configuration with measurement noise.

Existing heuristics are increasingly unable to address the complex constraints and requirements of sensor placement in nuclear systems. These constraints include restrictions on the regions where sensors can be placed, minimum allowable distances between sensors, and accommodating pre-existing sensor placements. Additionally, understanding sensor noise levels and the resulting estimation errors is crucial for reliable system monitoring. If input perturbations cause changes in measurable quantities, it becomes essential to identify these perturbations using only sensor readings and to select sensor configurations that capture and reconstruct system behavior accurately across all such perturbations. In this thesis, we develop scalable, efficient, and data-driven sensor placement algorithms that incorporate these constraints while leveraging compressive dimension reduction and matrix factorization techniques to optimize sensor locations and performance. These methods address the limitations of downsampled domain discretizations by preserving localized dynamics and fully utilizing the available data.

1.2 Contributions

This thesis explores reduced order models and sensor placement in spatially constrained settings for nuclear energy systems. Optimal point sensors are discovered using the singular value decomposition and matrix QR pivoting trained on computational models and data. An overview of our proposed approach, which determines optimal sensor placements efficiently by leveraging dimensionality reduction of data, is given in Figure 1.1. This figure illustrates one of the central examples explored in this thesis: a fuel test prototype, which simulates the interaction between coolant flow and a fuel element. Interactions between the nuclear fuel element and the coolant, particularly under conditions where the coolant boils or fails to adequately remove heat, can lead to catastrophic outcomes, as seen in some of the worst nuclear accidents caused by overheating, core damage, and radioactive release. It is vital to analyze the gravity-driven advection of the coolant to study heat transfer through the capsule and avoid nucleate boiling through optimized sensor locations. For safety and practicality, an electric heating element is used in this setup, as testing nuclear fuel interactions with the coolant would pose significant safety risks and violate regulatory standards.

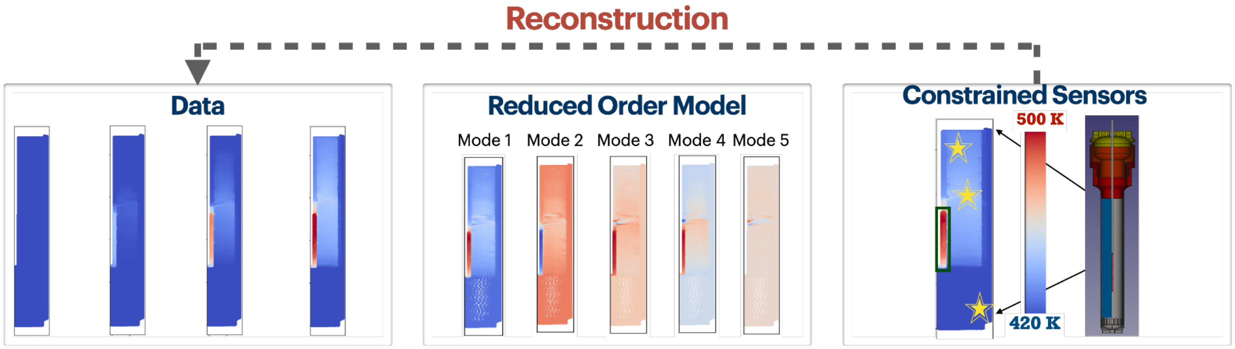

Figure 1.1: This work leverages dimensionality reduction techniques on high-dimensional data to efficiently optimize sensor placement in the presence of spatial constraints for signal reconstruction, estimation, and control. This figure illustrates the sensor placement on a fuel test prototype designed to simulate the interaction between coolant flow and a fuel element where at most one sensor is allowed in the fuel region. (adapted with permission from [13])

In Chapter 2, we delve into the critical role of computational models in the nuclear industry, particularly for simulating safety-critical systems such as the coolant-fuel interactions described earlier. The chapter also introduces advanced methodologies, including data-driven reduced-order modeling for high-dimensional nuclear datasets, innovative sensing techniques, digital twin frameworks, and approaches for uncertainty estimation, all aimed at enhancing the accuracy and reliability of these simulations. Chapter 3 presents our data-driven optimization approach for sensor placement in the fuel test prototype, addressing spatial constraints such as restricted sensor regions, minimum sensor proximities, and pre-existing placements. The fuel test prototype is electrically heated to emulate the neutronic effect of nuclear fuel and supports transient loss-of-coolant accident simulations, aiding qualification of an identical rig at Idaho National Laboratory (INL). This chapter introduces a sensor placement strategy based on modal decomposition and D-optimal design criteria, optimizing reconstruction accuracy and uncertainty under noisy measurements. Empirical and theoretical validation demonstrates near-optimal performance compared to exhaustive enumeration for low-dimensional systems. Applied to high-dimensional scenarios, including 2D heat diffusion and the fuel test prototypes temperature fields with up to 40,510 candidate locations, the optimized sensor configurations achieve superior accuracy and uncertainty estimation compared to random placements, ensuring robust performance under spatial and measurement constraints.

Chapter 4 expands the application of constrained sensor placement algorithms to the entire nuclear power plant (NPP), addressing component-specific constraints across fuel capsules, fuel rods, and steam generators. The developed approach optimizes sensor layouts for multiple fields of interest while adhering to spatial and operational limitations inherent to each subsystem. This chapter demonstrates the methodology using computational models of NPP subsystems. For steam generators, constrained sensor layouts derived from 1D simulations achieve high accuracy in capturing multiple fields of interest and provide interpretable models for boiling regime analysis. In 3D CFD simulations, temperature variations due to changing primary coolant mass flow rates are reconstructed using thermocouples placed on the shell and a single instrumented tube. For nuclear fuel irradiation experiments, sensors positioned on the graphite holder outside the fuel accurately reconstruct internal temperatures with minimal uncertainty. Similarly, during accident scenario testing of fuel rods, the approach captures transient temperature variations while restricting sensors to regions outside the heater adjacent area. By placing the minimal number of sensors in critical or obstructive locations, such as nuclear fuel regions or steam generator tubes, the method achieves accurate reconstructions with as few as three intrusive sensors. These optimized layouts minimize reconstruction errors, provide statistical bounds for noise-induced uncertainties, and are demonstrated to be invaluable for safety analysis, licensing, accident scenario testing, and reliability analysis across high-dimensional NPP applications.

Chapter 5 focuses on advancing our methodology to improve reconstruction accuracy under transient conditions, classification of transient regimes and power perturbations, addressing critical challenges in dynamic and complex systems. We address the effects of power transients on reactor core coolant temperature. Leveraging reduced-order models (ROMs), including dynamic mode decomposition with control (DMDc), we have uncovered the underlying dynamics of power perturbations of the nuclear fuel rod. Our methodology adapts to transient conditions by optimizing sensor locations and sampling intervals. This approach has revealed the influence of various ROMs on sensor placement and flow reconstruction performance. Integrating techniques such as linear discriminant analysis (LDA) and DMDc has enabled classification of transient regimes, ensuring accurate monitoring of dynamic operational states.

The work presented in Chapters 3, 4 of this thesis have resulted in the following peer-reviewed publications. The majority of textual and visual content in these chapters are reproduced with permission from these manuscripts:

> **Karnik N**, Abdo MG, Estrada-Perez CE, Yoo JS, Cogliati JJ, Skifton RS, Calderoni P, Brunton SL, Manohar K. Constrained optimization of sensor placement for nuclear digital twins. IEEE Sensors Journal. 2024 Feb 28.
>
> **Karnik N**, Wang C, Bhowmik PK, Cogliati JJ, Balderrama Prieto SA, Xing C, Klishin AA, Skifton R, Moussaoui M, Folsom CP, Palmer JJ., Sabharwall P, Manohar K, Abdo MG, Leveraging Optimal Sparse Sensor Placement to Aggregate a Network of Digital Twins for Nuclear Subsystems. Energies (19961073). 2024 Jul 1;17(13).

The thesis concludes by outlining promising future research directions, including the investigation of nonlinear sensor measurement scenarios where variance-based optimization methods may prove inadequate, and the extension of these methodologies to enable real-time control of digital twin systems.

Chapter 2

BACKGROUND ON DATA-DRIVEN SENSING

Computational and reduced-order models (ROMs) are essential in nuclear subsystem analysis and design due to their ability to handle complex, nonlinear, multiphysics phenomena while maintaining computational efficiency. These models enable detailed simulations for predictive analysis, design optimization, and safety assessment, significantly reducing the need for costly and time-consuming physical experiments. Given the stringent safety constraints in nuclear systems, computational models are often the only viable approach for analyzing operations and accident scenarios, as real-world testing of failures or accidents is impractical and hazardous. Integration of sensor data with computational models enhances testing fidelity and enables predictive maintenance, allowing for preemptive action before faults escalate. Furthermore, sensor-informed modeling ensures precise reliability assessments and supports regulatory compliance by providing detailed, data-backed safety evaluations. To capture accurate data to validate models, monitor system health, and detect anomalies early, it is critical to optimize senor locations. In the following sections we examine reduced-order models, sensing techniques, and nuclear digital twins.

2.1 Data-Driven Reduced Order Modeling

High-dimensional systems, such as those in fluid dynamics, epidemiology, neuroscience, and power grids, often exhibit dominant coherent structures that evolve on low-dimensional attractors. A reduced-order model (ROM) is a simplified mathematical representation of these complex, high-fidelity systems that retain its essential dynamics and key features while significantly reducing computational complexity. In today's world, vast amounts of data are generated from fluid, thermal, and nuclear models, simulations and experiments even before a system is physically realized. In a data-driven approach, these high-fidelity models are used to identify or learn the underlying dynamics that forms the basis for reduced-order models, enabling efficient representation and analysis of the system's behavior. ROMs are powerful tools for design optimization, control, multiphysics and multiscale modeling, parameter estimation and uncertainty quantification. The success of modern machine learning largely hinges on identifying and leveraging patterns and features within high-dimensional data, often building on reduced-order models (ROMs) to efficiently extract essential dynamics and enable scalable, data-driven insights for complex systems.

Reduced-order models (ROMs) are also key enablers of digital twins that compress high-fidelity, high-dimensional simulations into low-dimensional surrogate models with fewer degrees of freedom, significantly reducing computational burden while still capturing the characteristics of the relevant process [17, 18]. Nuclear applications require this ability to accurately simulate high-dimensional fields with minimal computational resources and without the complexity of full-order models [19, 20]. Projection-based ROMs, which represent high-fidelity physics using low-rank/data-driven modal decompositions, have been widely adopted for modeling fluids and turbulence [21, 22, 23, 24, 25] and nuclear core composition [26, 27, 28]. Such modal decompositions are closely related to empirical orthogonal functions for surrogate models in atmospheric sciences [29, 30], electrodynamics [31, 32] and heat transfer [33, 34]; as well as model reduction of stochastic processes [35] and balanced model reduction for optimal control [36, 37].

ROMs not only provide substantial dimensionality reduction for downstream decision-making and control, but also supply valuable physical information that can be leveraged for optimizing sensor placement. Crucial to this approach is the assumption that high-dimensional states can be expressed as a linear combination of basis features using a low-dimensional model. Linear reduced order modeling techniques are excellent at this when the most energetic features also have the largest influence on the dynamics of the system. Techniques like proper orthogonal decomposition (POD), dynamic mode decomposition (DMD), and balanced truncation project the system's high-dimensional state space onto a lower-dimensional subspace, capturing these dominant features or modes. These models are particularly effective for systems with linear or near-linear behavior, such as fluid flows at low Reynolds numbers or structural dynamics in small deformation regimes. On the other hand, systems where low-energy features have a significant impact on the system's evolution over time are particularly challenging to model with linear data-driven techniques as the mechanisms through which low-energy features influence high-energy dynamics are often highly nonlinear. Techniques like manifold learning [38], Koopman operator theory [39], or nonlinear autoregressive models, and autoencoders [40] account for the underlying nonlinear structures in the data. Nonlinear ROMs are crucial for capturing the dynamics of complex phenomena, such as turbulence, combustion, or biological processes, where linear assumptions fail to represent the system's behavior accurately.

The regulatory processes of nuclear safety, overseen by bodies like the Nuclear Regulatory Commission (NRC), are rigorous and require a high degree of explainability and transparency to ensure safety and compliance. Given the complexity of nuclear systems and the potential consequences of failure, regulatory assessments demand models that not only deliver accurate predictions but also provide clear insights into how these predictions are made. To meet these demands, in this thesis, we focus on developing optimal sensing techniques based on reduced-order models that offer both uncertainty quantification and explainability. Techniques like Proper Orthogonal Decomposition (POD) and Dynamic Mode Decomposition (DMD) identify low-dimensional structures, or modes, that capture the dominant dynamics of a system. These modes represent the key features on which the flow evolves, and the overall system behavior is generally a linear combination of these modes. By analyzing these modes, we can determine which sensors are most informative for capturing the essential dynamics of the system. Sensors are strategically chosen to monitor regions where the flow is most influenced by the dominant modes, ensuring that the sensor network captures the most critical information. This approach not only aids in efficient sensor placement but also provides a clear, explainable rationale for why specific sensors are selected, grounded in the underlying flow dynamics. These ROMs allow for the efficient representation of complex system dynamics while maintaining a level of interpretability, making it easier to trace how input data influences predictions, sensor locations and field reconstructions. Furthermore, by incorporating uncertainty quantification, these models enhance reliability for digital twins, providing confidence in decision-making processes and ensuring that regulatory standards for safety and performance are met. In the following subsection, we provide a brief description of proper orthogonal decomposition mentioned above.

2.1.1 Linear Reduced Order Models

In case of prior knowledge about the signal or system the patterns within data can be explored by extracting the dominant features that make the signal. This data-driven approach relies on low-rank embeddings such as POD (Proper Orthogonal Decomposition) to form a tailored basis for a specific problem. These embeddings are used in the ROM community to select measurements in the state space that facilitate feature space reconstruction. Given a set of high dimensional states $\mathbf{x} \in \mathbb{R}^n$, POD expresses them as a linear combination of POD orthonormal modes ψ and provides a low rank embedding where $\mathbf{a}$ represents the POD coefficients. This embedding can be lifted back to the full state as $\mathbf{x}_i \approx \sum_{k=1}^{r} a_k(t_i)\psi_k(x)$

We see that POD provides a space-time separation of variables where $a_k(t_i)$ vary in time and $\psi_k(x)$ vary spatially. These POD coefficients a_k and eigenmodes ψ_k can be obtained from the Singular Value Decomposition (SVD). Given a data matrix $\mathbf{X} = [\mathbf{x}_1\ \mathbf{x}_2\ \ldots\ \mathbf{x}_m]$ the orthonormal left singular vectors $\mathbf{U}$ of $\mathbf{X}$ calculated through SVD are the eigenmodes.

$$\mathbf{X} = \mathbf{U}\mathbf{D}\mathbf{V}^T \approx U_r\mathbf{D}_r\mathbf{V}^T$$

In the above equation r is the rank truncation factor which provides the dimensionality reduction required for reduced order modelling. Matrices $\mathbf{U}_r$, $\mathbf{V}_r$ hold the first r columns of $\mathbf{U}$ and $\mathbf{V}$. Diagonal matrix $\mathbf{D}_r$ holds the first $r \times r$ block of Σ singular values. Thus the low dimensional POD coefficients vector for state $\mathbf{x}$ is given by orthogonal projection $\mathbf{a} = \mathbf{U}_r^T\mathbf{x}$. Thus, POD is a widely used dimensionality reduction technique which allows computational speedup of numerical time-stepping, parameter estimation, and control.

2.2 Digital Twins

A digital twin is a virtual representation of a physical object, system, or process that uses real-time data and simulations to model, monitor, and predict its behavior. It integrates technologies such as IoT (Internet of Things), data analytics, artificial intelligence, and machine learning to create a dynamic digital counterpart of the physical entity. As shown in Figure 2.1, a digital twin framework consists of four primary spaces: a real/physical space containing the physical assets; a virtual/digital space containing the virtual computer-aided design (CAD) replica, along with the intelligence enabling all the decisions and recommendations being made; a data space containing the data warehouse; and an action and recommendation space [41, 42].

The data space usually contains data lakes and/or data warehouses utilizing different relational databases (using structured querying language to query smaller chunks of the data), or non-relational (e.g., NoSQL or graph databases) depending on the format of the data. The accumulated sensor data from multiple systems can be decentralized on distributed servers on the cloud or centralized in a single source of truth (i.e., digital thread) and is analyzed using advanced analytics and machine learning techniques. These analyses are instrumental in identifying anomalies, categorizing potential accident scenarios, and forecasting their likelihood and timing. Machine learning algorithms, for instance, can predict component wear or detect early signs of operational failure, thereby enabling preemptive maintenance actions that enhance safety and prevent unplanned outages.

The insights gained from the data space inform the recommendations and actions space, where they are translated into actionable guidance for system operators. This conversion of data into operational strategies enables timely and informed decision-making, allowing staff to implement necessary adjustments swiftly and effectively. Continuous feedback from the virtual sensors ensures that the digital twin remains a reliable and accurate tool for decision support, thereby streamlining operations and enhancing the decision-making process. NASA defines a digital twin as [43, 44]

> “An integrated multi-physics, multi-scale, probabilistic simulation of an as-built vehicle or system that uses the best available physical models, sensor updates, fleet history, etc., to mirror the life of its corresponding flying twin.”

Digital twins are widely used across industries, including manufacturing, healthcare, aerospace, energy, and smart cities, to optimize performance, predict maintenance needs, and enhance overall system efficiency. Digital twin realizations effectively function as virtual sensors, enabling the prediction of aircraft structure lifespans and ensuring their structural integrity throughout their lifecycle [45, 46].

2.2.1 Nuclear Digital Twins

A nuclear digital twin is a digital CAD replica of a physical counterpart whose complexity can vary from that of an individual fuel rodlet, heat pipe, or nuclear reactor, to that of an integrated energy system utilizing several different energy sources (e.g., wind, solar, and nuclear). A digital twin encompasses data of a system across all phases of its product lifecycle, enabling continuous monitoring, analysis, and optimization from inception to decommissioning. The nuclear digital twin also provides a visual representation of the system, along with the locations of various sensors and actuators [47]. The nuclear industry is moving toward digital twinning architectures that operate based on real-time data flows and control decisions [48]. Potential application areas for digital twins in the nuclear industry include design and licensing, plant construction, training simulators, predictive operations and maintenance, autonomous operation and control, failure and degradation prediction, the generation of insights from historical plant data, and safety and reliability analyses. During the design of any system, it is very important to test failure modes. In the nuclear field, building a physical prototype to test for failures is both challenging and extremely expensive. Modeling and simulating various designs/controls and assessing system failure scenarios without the need for destructive experimentation is of great value.

In nuclear applications, digital twinning requires real-time, high-precision simulations

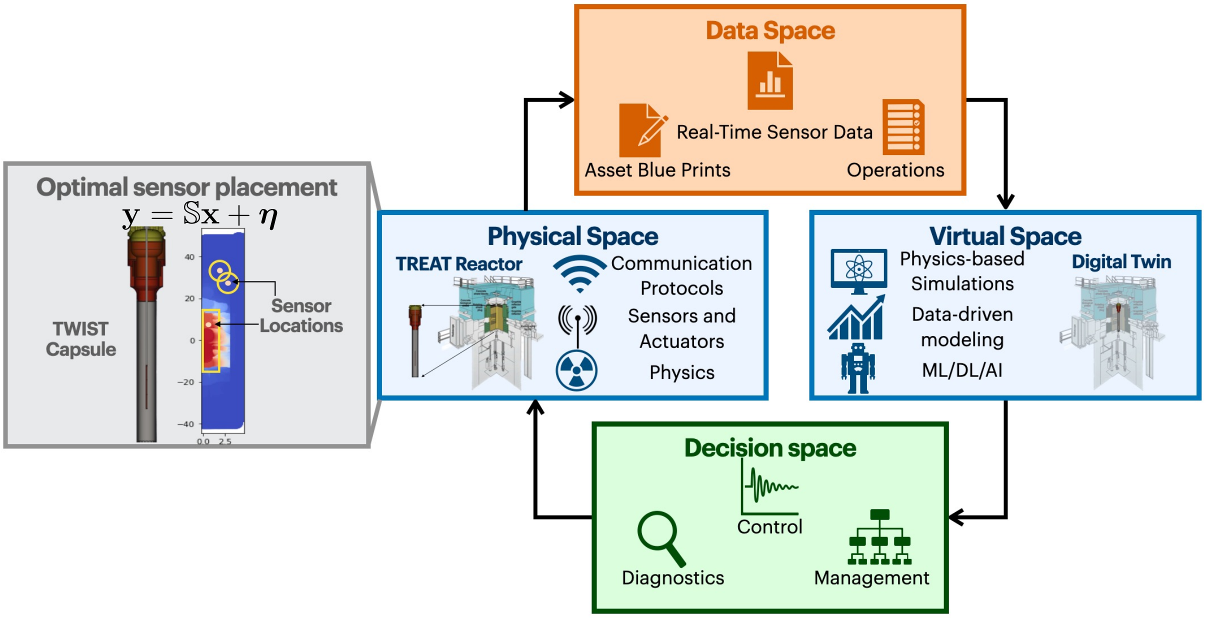

Figure 2.1: Digital twin frameworks consist of a real/physical space containing physical assets, a virtual digital space containing computer-aided design (CAD) replicas, simulations and Artificial Intelligence (AI), a data space and a decision space [41, 42]; all of which are enabled by sensors providing two-way communication between the virtual (ROMs and simulations) and the physical spaces. This digital twin characterizes the lifecycle of OPTI-TWIST (Out-of-Pile Testing and Instrumentation Transient Water Irradiation System) capsule, which is inserted into the TREAT (Transient Reactor Test Facility) reactor at Idaho National Laboratory to test fuel compositions.

featuring online autonomous calibration to real data via machine learning (ML) (e.g., using k-means clustering and artificial neural networks [49]). Evaluating the effect of uncertainty in the digital twin, as simulated by ML models on reactor instrumentation [50], and establishing (through sensors) a real-time two-way connection between the physical and the virtual spaces are crucial considerations for the success of digital twins [51].

Real-time sensor data streaming through communication protocols within private channels or the Industrial Internet of Things is indispensable for creating digital twin architectures for nuclear applications (see Figure 2.1). The sensors provide continuous self-validation of the ML/AI models which not only reflect the current state of the dynamical system but also predict, in real time, future states of the dynamics. Current sensor technologies in the nuclear field reflect a preference that sensors be installed in easily accessible areas. Only a few algorithms have been developed for sensor placement in nuclear reactors such as the generalized empirical interpolation method [52], reinforcement learning [53], and a directed graph approach for minimizing postulated faults with maximum imperceptibility [54].

For high-dimensional nuclear systems, it is difficult to optimally place sensors for accurate flow field reconstruction. ROMs help reveal the underlying dynamics and behavior of these complex systems—all while using minimal computational resources [55]. These ROMs facilitate the creation of digital twins. Figure 2.1 provides an overview of sensor placement for enabling digital twins within the nuclear industry and elaborates on the need for optimization of sensor locations. As Digital twins showcase **entire product lifecycles**, from design to retirement, in the first three product lifecycle phases, sensors play a crucial role in the digitized replica [56]:

1. **Design phase:** Before the physical asset is even conceptualized, the virtual prototype of the process or plant being designed is subjected to stress-strain analyses, simulation, control, and analysis for failure modes. However, few virtual prototypes utilize optimal sensing techniques to determine the best locations and number of sensors to recreate the flow fields of the physical asset. The present work contributes by optimizing sensor placement in the design phase while also accounting for the spatial constraints that arise in the physical asset. This means that, prior to physical asset production, sensor locations can be simulated on the virtual prototype so as to self-validate ML surrogate models established for control procedures.

2. **Manufacturing phase:** Virtual sensors are converted into physical sensors and validated based on experimentation. If certain constraints arise during production, optimal sensing techniques can incorporate them in real time and then suggest the next best

set of optimal sensor locations.

3. **Service phase:** Once the product/process/plant is deployed, sensors based on the maintenance and repair constraints suggested by the algorithm during the design phase can showcase their abilities. While in service, certain sensors may fail or give erroneous readings. Such obstacles that arise during service can be tackled by having the sparse sensing algorithm quantify the erroneous readings and compensate for sensor failures.

In the last phase, **retirement**, the physical asset is disassembled, re-manufactured, reused, or disposed of. Similarly, digital twins can be classified based on *realizations of the product*: prototypes, instances, and aggregates. Sensor communication among various *instances* of a product is crucial. In **digital twin aggregates**, multiple instances of either the same product (mass production) or different components form a higher-level twin. In this phase, new constraints may be imposed on sensor placement, based on the aggregation of products.

Therefore, optimal sensor technologies empower digital twins by critically enabling the integration of in-field and real-time raw data into the virtual replica of a physical prototype at any point during its product lifecycle [57].

2.3 Data-driven Sparse Sensing

Sensors play a crucial role in characterizing spatio-temporal dynamics in high-dimensional, non-linear systems such as atmospheric dynamics [58], fluid flows, manufacturing [14] and power-grid systems. Determining optimal sensor locations with respect to a desired objective is a NP-hard brute-force search among combinatorially many candidate placements. There are various high-level objectives for sensor placement such as reconstruction [4, 59, 8, 60, 13, 9, 35], classification [6, 61], reduced-order modeling [9, 10, 11, 12], control [62, 63, 64, 65, 15], and anomaly detection [66, 67, 54]. Common approaches to optimizing sensor placement include maximizing the information criteria [3, 68, 69, 70], Bayesian statistics [71, 72], compressed sensing [73, 74], heuristic methods [75] and framing sensor placement as a submodular selection problem [5]. However, some approaches based on kalman filter sensor selection are not submodular [76]. Sub-modular objectives can be efficiently optimized for hundreds or thousands of candidate locations using convex [4, 77, 78, 6] or greedy optimization approaches [5].

Sensor placement in linear dynamical systems have been optimized using gradient descent methods with similar computational complexity [7]. Sensor selection for continuous-time linear dynamical systems has also been achieved through sparsity-promoting frameworks which identify sparsity patterns of feedback gains in optimal control problems [79, 80, 81]. This approach can also be extended for optimal selection of a subset of available sensors or actuators in large-scale dynamical systems [82].

These methods do not scale well to high-dimensional system models and thus sensor selection approaches which leverage dimensionality reduction techniques such as proper orthogonal decomposition (POD) and ,empirical interpolation methods(EIM) were explored [83, 11]. Linear reconstruction of global fields through POD was initially used with random measurements, subsequent work optimized sensor locations through EIM. The pioneering physics-based approaches placed point sensors at strategic locations or extrema of the leading POD modes for flow reconstruction in a POD basis [8, 9]. These were succeeded by EIMs in projection-based reduced order modeling [11, 12] which yielded a marked improvement in reconstruction accuracy. A library of POD modes and sparse approximation has been used to classify flow environments from sparse noisy data collected by wing strain sensors in the Manduca sexta hawkmoth [84]. The accuracy of the method has been studied for varying signal to noise ratios (SNR). The connection between EIMs and optimal sensor placement was made explicit in [13], and generalized to optimal actuator placement for control [15], greedy cost constraints [85, 16], multi-fidelity sensors [86], and multi-scale physics [87]. These approaches can be further extended to provide a sensor landscape based on data-induced interactions instead of an optimal sensor configuration [88].

The above mentioned linear-theory based tools face challenges in capturing the dynamics of highly non-linear and chaotic systems [89]. As an alternative to traditional linear methods, shallow neural networks (SNNs) which are generally known as shallow decoder networks

(SDNs) are used to learn a mapping from sensor measurements to the flow field for global field reconstruction [90]. These reconstructions are less sensitive to sensor location than linear methods, however their performance can be further improved by selecting measurement locations in a principled manner [91, 92]. Convolutional neural networks (CNNs) have emerged as nonlinear alternatives to reconstruct chaotic data from sparse measurements in an efficient manner [93, 94, 95, 96, 97]. The autoencoder reduced-order representation is used for state estimation from sparse and noisy data and achieves the same accuracy as traditional methods while improving reconstruction efficiency by 70 % [98] In order to incorporate physics-constraints and reconstruct fluid flows from sparse, noisy velocity data, Bayesian deep learning techniques are used [99]. Physics informed neural networks (PINNs) overcome the large amount of data required for deep learning techniques and thus hybrid data-driven and physics-based reconstruction from sparse data helps infer unknown conditions if the physics is partially known [100, 101]. Most of the methods mentioned above develop strategies for accurate and efficient classification, reconstruction or anomaly detection with randomly placed or unorganized sensors as opposed to optimizing placement of sensors with respect to a certain objective [102, 93, 103, 104, 105].

For unknown Distributed Parameter Systems (DPSs), reinforcement learning based optimal sensor placement strategies that circumvent requirements of convexity, submodularity and need for a model have been developed [106]. Deep reinforcement learning algorithms have also been used to formulate control schemes by optimizing sensor configurations in the wake of a cylinder [64, 107]. Multi-objective optimization of sensors in Wireless Sensor Networks (WSNs) design and energy utilization through the genetic algorithm has been explored thoroughly [108, 109, 110].

2.4 Sensing and Uncertainty Analysis for Nuclear Assets

Sensing technologies play a critical role in the nuclear industry by providing real-time, accurate data to monitor the performance, safety, and integrity of nuclear systems and components throughout their lifecycle. The nuclear industry is increasingly adopting instrumen-

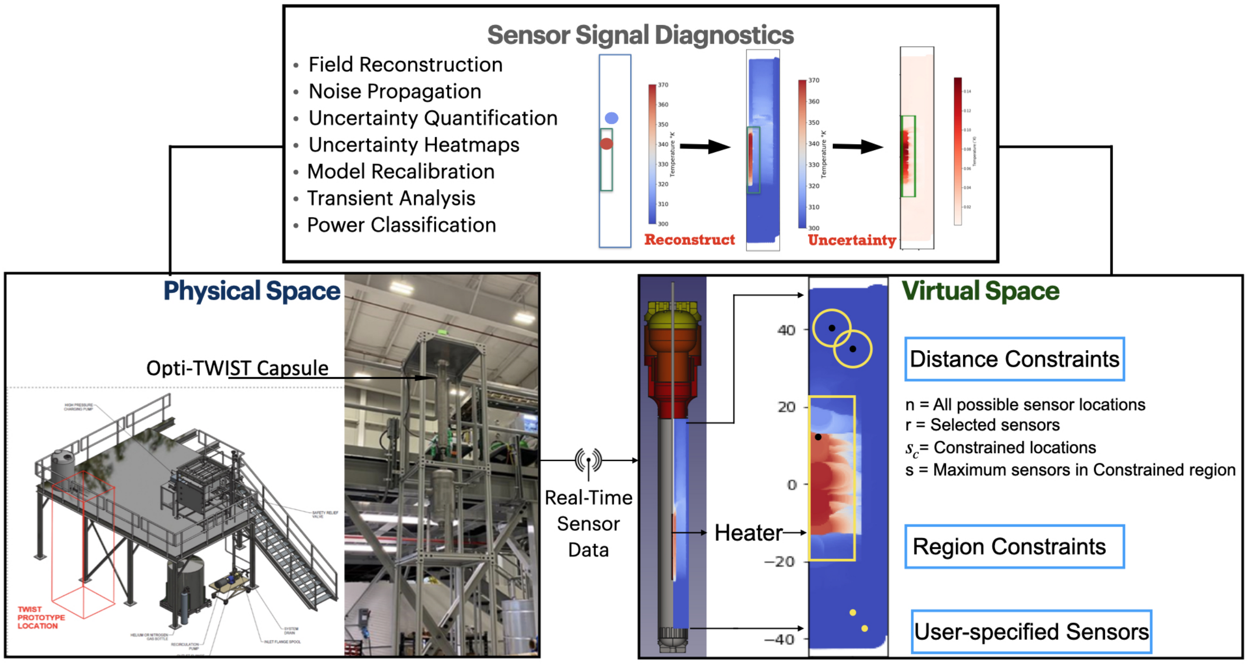

Figure 2.2: Physical sensors capture real-time data that can be seamlessly compared with virtual sensors and reduced-order models, enabling high-fidelity insights for full-field reconstruction, model validation, operational monitoring, and precise uncertainty quantification.

tation that provides real-time, accurate, spatially-resolved data on test conditions and the performance of fuels and materials during irradiation. The integration of innovative optical fiber, acoustic, and electrical impedance sensing technologies and measurement techniques are crucial to support these advancements [111]. Further, the adoption of condition-based maintenance and automation in the nuclear power industry, requires key online monitoring (OLM) applications to enhance safety, efficiency, and predictive maintenance, with an emphasis on noise analysis and integrated system requirements [112]. Traditionally, sensing and monitoring in the nuclear industry relied on manual inspections and conventional instrumentation to ensure the safety, efficiency, and performance of critical systems and components. Previous work proposes algorithms for sensor fault detection, isolation, and signal reconstruction in nuclear power plants, using anomaly detection, interquartile range-based schemes, and autoregressive models to ensure accurate readings and enhance safety [113].

Uncertainty can originate extrinsically such as uncertain inputs to a model, user-introduced errors, truncation errors, and misinterpretations. This is usually referred to as epistemic uncertainties for they can be reduced by acquiring more knowledge, adding more terms to the truncated model, or acquiring more data/samples. Uncertainty can also originate intrinsically such as inherent stochasticity, noisy telemetry data, low-resolution images, and instrumental uncertainty. This is usually referred to as aleatoric uncertainty because it cannot be reduced since it usually incorporates random probabilistic natures.

In nuclear applications, the separation between these types of uncertainties is imperative for its tight coupling to safety and regulatory aspects [114] which explains significant investments to integrate covariance cross section data in nuclear codes such as SCALE [115]. Sensor integration further enhances uncertainty quantification by providing real-time data for model validation and refinement, enabling adaptive safety mechanisms [116]. Advances in machine learning and data-driven approaches have introduced techniques to reduce computational costs while maintaining high accuracy in uncertainty estimations. Additionally, uncertainty-aware designs, such as those in reactor vessel methodologies or heat exchanger efficiency assessments [117], improve reliability and safety during both operation and decommissioning phases. These advancements collectively ensure that nuclear systems meet stringent regulatory and safety requirements in an economically viable manner.

Uncertainty in digital twin (DT) predictions propagates from sensor noise, upstream process disturbances, and modeling errors. This uncertainty, originating in the precision and noise of sensor measurements, cascades through DT subsystem components. Uncertainty quantification is crucial for verifying predicted temperatures, heat flux, and flow components within nuclear reactors. In this study, we design sensor placements to systematically minimize and characterize uncertainty from sensor-based state reconstruction in digital twin components, utilizing low-dimensional representations of simulation data.

Chapter 3

CONSTRAINED OPTIMIZATION OF SENSOR PLACEMENT FOR TEMPERATURE FIELD RECONSTRUCTION

In this chapter, we develop a data-driven optimization approach for a nuclear component prototype, incorporating spatial constraints. In certain regions of a reactor, the placement of sensors may be constrained due to limited space availability or specific requirements dictating predetermined sensor locations, restricted areas within the reactor, fixed numbers of sensors within a region, or a minimum allowed proximity between sensors. Our target application is the Out-of-Pile Testing and Instrumentation Transient Water Irradiation System (OPTI-TWIST) prototype which is electrically heated to emulate the neutronic effect of a nuclear fuel. Production version of TWIST serves as a multi-purpose test rig for surrogate fuel rodlets, and simulate transient loss of coolant accident scenarios, to assist in qualification of an identical irradiation rig for the Idaho National Laboratory (INL) Transient Reactor Test Facility (TREAT).

We adapt data-driven methods based on modal decomposition [15] to enforce these constraints during optimization, and develop placement strategies for full-field reconstruction based on sparse spatially constrained sensor measurements. Our algorithm minimizes error covariance using D-optimal design criteria, which provides an evaluation metric for a given sensor configuration and corresponding estimates of reconstruction uncertainty under noisy measurements. Using empirical and theoretical validation, the present work demonstrates the technique to be near optimal using exhaustive enumeration of all feasible sensor configurations for a low-dimensional dynamical system. The optimized sensors under constraints are demonstrated to provide highly accurate reconstruction and uncertainty estimates under noisy measurements when compared to random placements in high-dimensional 2D heat diffusion, OPTI-TWIST steady-state and transient temperature fields with up to 40510 candidate sensor locations. We detail the reconstruction of latent flow fields from sparse sensor measurements using reduced order modeling.

3.1 Sparse Sensing for Reconstruction

The core of our work is the reconstruction of latent fields $\mathbf{x} \in \mathbb{R}^n$ from p noise-corrupted sensor measurements $\mathbf{y} \in \mathbb{R}^p$

$$\mathbf{y} = \mathbb{S}\mathbf{x} + \boldsymbol{\eta}, \tag{3.1}$$

where $\boldsymbol{\eta}$ consists of zero-mean, Gaussian independent and identically distributed (i.i.d.) components, and $\mathbb{S} \in \mathbb{R}^{p\times n}$ is the desired sensor (measurement) selection operator. In nuclear applications, the number of measurements p is severely limited relative to the large dimensionality of the latent field. We encode the field dynamics as a linear combination of spatial basis modes $\boldsymbol{\psi}_k(\xi)$ weighted by time-varying coefficients

$$\mathbf{x}(t) \approx \sum_{k=1}^{r} a_k(t)\boldsymbol{\psi}_k(\xi). \tag{3.2}$$

For each field or full state $\mathbf{x}$ at a fixed t, the vector $\mathbf{a}$ composed of the r coefficients $a_k(t)$ defines a low-rank embedding of the form

$$\mathbf{x} = \boldsymbol{\Psi}_r\mathbf{a},$$

where the modes $\boldsymbol{\psi}_k$ comprise the columns of $\boldsymbol{\Psi}_r$. This basis, which can be built from spectral or data-driven decomposition methods, is typically chosen so that the embedding dimension is as small as possible, i.e., $r \ll n$.

Given this assumption, high-dimensional states can be directly recovered from measurements via the maximum likelihood estimate of the basis coefficients, $\hat{\mathbf{a}} = (\mathbb{S}\boldsymbol{\Psi}_r)^\dagger\mathbf{y}$:

$$\hat{\mathbf{x}} = \boldsymbol{\Psi}_r(\mathbb{S}\boldsymbol{\Psi}_r)^\dagger\mathbf{y}, \tag{3.3}$$

known as gappy proper orthogonal decomposition (POD) [35]. The gappy estimator is well-posed when the number of sensors equals or exceeds r. Importantly, the inherent compressibility of physical fields enables a drastic reduction in the number of sensors required for high-fidelity reconstruction. The critical enabler for *sparse sensing* is the fact that nuclear processes are strictly governed by a small set of underlying physics. As we shall see, strategic selection of sensor measurements—based on noisy flow physics—allows for an extremely small number of deployed sensors to be used.

3.2 Proper Orthogonal Decomposition

The data embedding rank dictates the minimum number of sensors required for reconstruction, necessitating a choice of basis with the lowest possible rank. Given full state data sampled from physics/CFD simulations $\mathbf{X} = \begin{bmatrix}\mathbf{x}_1 & \dots & \mathbf{x}_m\end{bmatrix}$, the proper orthogonal decomposition (POD) [83] provides the minimal rank approximation to data

$$\underset{\boldsymbol{\Psi},\mathrm{rank}(\boldsymbol{\Psi})=r}{\operatorname{argmin}} \; \|\mathbf{X} - \boldsymbol{\Psi}\boldsymbol{\Psi}^T\mathbf{X}\|_F^2, \tag{3.4}$$

where the low-rank embedding is given by the projection of the data onto orthogonal POD modes, $\boldsymbol{\Psi}_r^T\mathbf{X}$. The solution to (3.4) is computed using the singular value decomposition of the data matrix, $\mathbf{X} = \mathbf{U}\mathbf{D}\mathbf{V}^*$, where the leading r left singular vectors comprise the desired POD modes

$$\boldsymbol{\Psi}_r = \mathbf{U}_r = \begin{bmatrix}\mathbf{u}_1 & \mathbf{u}_2 & \dots & \mathbf{u}_r\end{bmatrix}. \tag{3.5}$$

The singular values (diagonal entries of $\mathbf{D}$), quantify the decreasing energy contribution of each successive mode and determine the truncation rank. Most physical data have much fewer degrees of freedom than the ambient data dimension, allowing a very small choice of r. The cumulative energy captured by the leading r modes is $\sum_{i=1}^{r} d_i / \sum_i d_i$. In practice, the smallest possible r capturing 90-99% of cumulative energy above the noise threshold is used as the model truncation rank. Therefore, POD is also the workhorse of projection-based model order reduction, used for projecting governing equation terms onto POD modes to obtain highly computationally expedient surrogate models for high-fidelity physics.

3.3 Optimal Design for Gappy Estimation

The placement of sensors is defined by a measurement selection operator $\mathbb{S} \in \mathbb{R}^{p \times n}$ that optimally recovers modal mixture $\mathbf{a}$ from sensor measurements $\mathbf{y}$. This measurement selection operator $\mathbb{S}$ encodes point measurements with unit entries in a sparse matrix

$$\mathbb{S} = \begin{bmatrix} \mathbf{e}_{\gamma_1} & \mathbf{e}_{\gamma_2} & \dots & \mathbf{e}_{\gamma_p} \end{bmatrix}^T, \tag{3.6}$$

where $\mathbf{e}_j$ are canonical basis vectors for $\mathbb{R}^n$, with a unit entry in component j (where a sensor should be placed) and zeroes elsewhere. Here, $\gamma = \{\gamma_1, \gamma_2, \dots, \gamma_p\} \subset \{1, 2, \dots, n\}$ denotes the index set of sensor locations with cardinality p. Sensor selection then corresponds to the components of $\mathbf{x}$ that were chosen to be measured:

$$\mathbb{S}\mathbf{x} = \begin{bmatrix} x_{\gamma_1} & x_{\gamma_2} & \dots & x_{\gamma_p} \end{bmatrix}^T. \tag{3.7}$$

The selection of sensors is based on the optimal estimation of the entire state vector $\mathbf{x} \in \mathbb{R}^n$ from p experiment outputs $\mathbf{y} \in \mathbb{R}^p$ with additive i.i.d. Gaussian noise $\eta_i \sim \mathcal{N}(\mathbf{0}, \beta^2)$ in each measurement $\mathbf{y}_i$:

$$\mathbf{y} = \mathbb{S}\boldsymbol{\Psi}_r\mathbf{a} + \boldsymbol{\eta}. \tag{3.8}$$

The values of $\mathbf{x}$ at unmeasured locations can be recovered by solving a linear system of equations for the basis coefficients via the Moore-Penrose pseudoinverse of $\mathbb{S}\boldsymbol{\Psi}_r$ (gappy POD (3.3)):

$$\hat{\mathbf{x}} = \boldsymbol{\Psi}_r(\mathbb{S}\boldsymbol{\Psi}_r)^{\dagger}\mathbf{y}.$$

The row indices of $\boldsymbol{\Psi}_r$ correspond to sensor locations in the state space that effectively condition the matrix inversion, enabling accurate reconstruction of the estimated state $\hat{\mathbf{x}}$.

Optimal design of experiments [118] for estimation problems involves the strategic selection of a set of experiments to gather sufficient information about the domain, enabling accurate predictions for measurements where experiments were not performed. Statistical criteria, such as A, D and E-optimality, are used to select the set which minimizes or maximizes different properties of the Fisher information matrix. Fisher information [118] measures the amount of information a random variable contains about the estimated parameter, such as its true mean or standard deviation. The Fisher information matrix defines covariance matrices associated with maximum-likelihood estimates and is $(\mathbb{S}\boldsymbol{\Psi}_r)^T(\mathbb{S}\boldsymbol{\Psi}_r)$ in our case. A-optimal designs minimize the trace of the inverse of the Fisher information matrix, whereas E-optimal designs maximize the minimum eigenvalue of the information matrix. D-optimal designs [119] minimize the generalized variance of the parameter estimates by maximizing the determinant of the Fisher information matrix [120].

Optimal design for gappy estimation involves placing sensors at limited points in the domain to accurately reconstruct flow fields over the entire domain. In contrast to classical optimal design in which each sensor can be used multiple times out of a set of candidate sensors, candidate sensors can only be used once in the gappy framework. In this setting, design of experiments aims to optimize the sensor selection $\mathbb{S}$ to optimize statistics of the estimation error $\mathbf{a} - \hat{\mathbf{a}}$, an r-dimensional random variable with zero mean and covariance

$$\boldsymbol{\Sigma} = \mathrm{Var}(\mathbf{a} - \hat{\mathbf{a}}) = \beta^2((\mathbb{S}\boldsymbol{\Psi}_r)^T(\mathbb{S}\boldsymbol{\Psi}_r))^{-1}. \tag{3.9}$$

The eigenvalues of this covariance matrix characterize the statistical and geometric measures of estimation error “size” [121], shown in Table 3.1. Generalized variance, defined by $\det(\boldsymbol{\Sigma})$, characterizes correlations among pairs of variables. When it is large, the variables have little correlation with each other; when it is small, the variables are strongly correlated. On the other hand, average variance, given by $\mathrm{tr}(\boldsymbol{\Sigma})$, is the sum of the population variances.

Measure	Formula	Geometry
Generalized variance	$\det(\boldsymbol{\Sigma}) = \Pi_i \lambda_i$	area, (hyper)volume
Average variance	$\mathrm{tr}(\boldsymbol{\Sigma}) = \sum_i \lambda_i$	linear sum
Maximal variance	$\lambda_{\max}$	maximum dispersion

Table 3.1: Statistical and geometric measures for error covariance [121]

A-optimal criteria minimize this average variance, while E-optimal criteria minimize the maximal variance of $\mathbf{\Sigma}$. The variance, which measures the uncertainty in the estimated response, should be small for minimal deviation between estimated and true values [119].

We consider D-optimal design for flow field reconstruction with information matrix $(\mathbb{S}\mathbf{\Psi}_r)^T(\mathbb{S}\mathbf{\Psi}_r)$, which depends on the selected sensors $\mathbb{S}(\gamma)$. The determinant objective maximizes the information volume via maximization of its determinant, given a budget of p sensors. The maximizing sensor set of this criterion is also the maximizer of its logarithm

$$\gamma_* = \underset{\gamma, |\gamma|=p}{\operatorname{argmax}} \; \log\det((\mathbb{S}\mathbf{\Psi}_r)^T(\mathbb{S}\mathbf{\Psi}_r)). \tag{3.10}$$

When $p = r$, Equation 5.12 is equivalent to the maximizer of $\log|\det(\mathbb{S}\mathbf{\Psi}_r)|$. Direct optimization of this criterion leads to a brute force combinatorial search. This sensor placement approach builds upon the empirical interpolation method (EIM) [10] and discrete empirical interpolation method (DEIM) [11] which select the best interpolation points for evaluating nonlinear terms in projection-based reduced order models. However, these methods do not directly optimize statistics of the error or minimize error covariance. In the next section, we develop a greedy strategy for optimizing sensor selection under constraints built upon the pivoted QR factorization [12, 13, 14, 15], and analyze the reconstruction performance with respect to D-optimal design criteria.

3.4 Column-pivoted QR Decomposition with Spatial Constraints

The QR factorization with column pivoting decomposes a matrix $\mathbf{W} \in \mathbb{R}^{m \times n}$ into a unitary matrix $\mathbf{Q}$, an upper-triangular matrix $\mathbf{R}$, and a column permutation matrix $\mathbf{\Pi}$, such that $\mathbf{W\Pi} = \mathbf{QR}$. As described above, each column index of $\mathbf{\Psi}_r^T$ corresponds to a single sensor location in the state space. We applied QR pivoting to the transpose of our basis, i.e. $\mathbf{W} = \mathbf{\Psi}_r^T$, and use the permutation matrix to store information about the sensors selected. The pivoted QR decomposition is a greedy algorithm for optimizing Equation 5.12 that, in each iteration) selects a new column pivot (sensor location) with maximal two-norm, then subtracting from every other column vector its orthogonal projection onto the pivot column

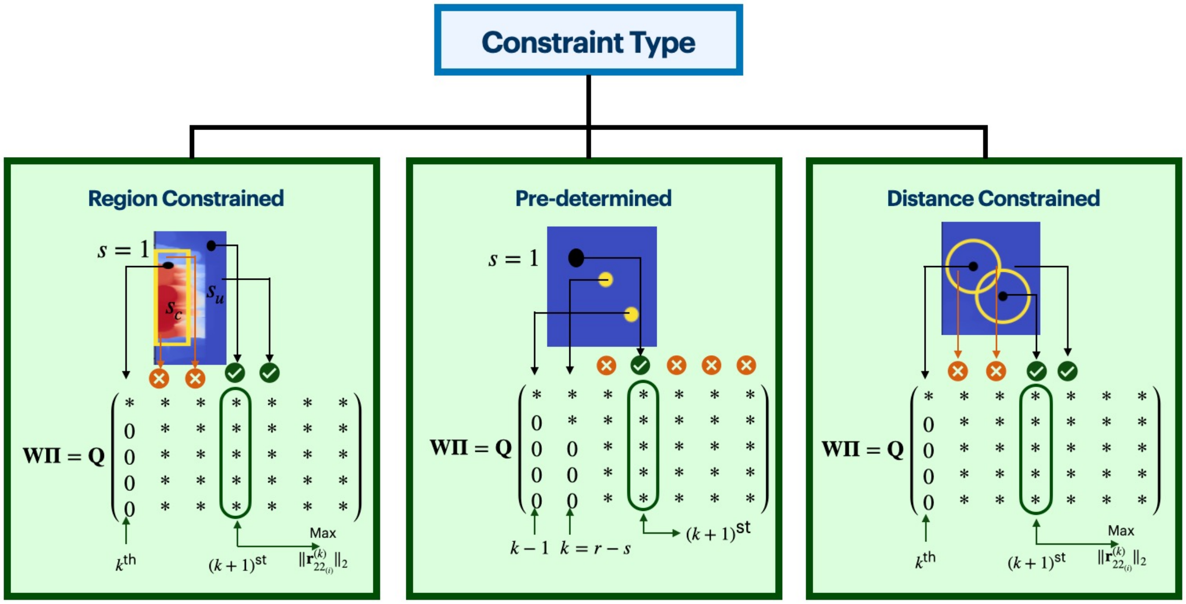

Figure 3.1: Greedy selection of the next sensor involves choosing the next pivot column of $\mathbf{\Psi}^T$ from the set of allowable sensor locations specified by the constraint.

[13, 12]. This projection is given by a Householder reflector that maps any vector $\boldsymbol{\nu}$ to $-\operatorname{sign}\nu_1\sigma\mathbf{e}_1$, where $\sigma = \|\boldsymbol{\nu}\|_2$ and ν_1 is the first component of $\boldsymbol{\nu}$

$$\mathbf{H}(\boldsymbol{\nu}) = \mathbf{I} - \frac{(\boldsymbol{\nu} + \operatorname{sign}(\nu_1)\sigma\mathbf{e}_1)(\boldsymbol{\nu} + \operatorname{sign}(\nu_1)\sigma\mathbf{e}_1)^T}{\sigma(\sigma + |\nu_1|)}. \tag{3.11}$$

Householder projections effectively zero out the subdiagonal components of column vectors in each iteration to induce upper-triangular structure in $\mathbf{W}$, constructing $\mathbf{R}$ in place. Householder reflectors can be written in the standard form $\mathbf{I} - 2\mathbf{u}\mathbf{u}^T$, where $\mathbf{u}$ has unit norm.

Consider the following partial QR factorization at the k^{th} iteration in the pivoting procedure:

$$\mathbf{W\Pi} = \mathbf{QR} = \mathbf{Q}\begin{bmatrix} \mathbf{R}^{(k)}_{11} & \mathbf{R}^{(k)}_{12} \\ 0 & \mathbf{R}^{(k)}_{22} \end{bmatrix}, \tag{3.12}$$

where $\mathbf{Q} \in \mathbb{R}^{m\times m}$ is orthogonal, $\mathbf{R}^{(k)}_{11} \in \mathbb{R}^{k\times k}$ is upper triangular, $\mathbf{R}^{(k)}_{12} \in \mathbb{R}^{k\times(n-k)}$, $\mathbf{R}^{(k)}_{22} \in \mathbb{R}^{(m-k)\times(n-k)}$, and $\mathbf{\Pi} \in \mathbb{R}^{n\times n}$ is the permutation matrix containing information about the first

k chosen sensors [122, 86, 123]. In unconstrained QR pivoting, the $(k+1)^{\text{st}}$ iteration selects a column from the submatrix $\mathbf{R}_{22}^{(k)}$ with the maximal two-norm, then swaps the selected column with the $(k+1)^{\text{st}}$ column while updating permutation indices

$$l = \underset{i=1,\ldots,n-k}{\operatorname{argmax}} \|\mathbf{r}_{22_{(i)}}^{(k)}\|_2. \tag{3.13}$$

Constraints are integrated within this step, by forcing the pivot column index to be selected from the latest set of allowable indices based on the constraints under consideration. The $k+1^{\text{st}}$ iteration in constrained optimization selects the pivot column with largest 2 norm, $\mathbf{r}_{22_{(i)}}^{(k)}$, from the constrained/unconstrained set of allowable column indices in $\mathbf{R}_{22}^{(k)}$. The QR pivoting algorithm results in the following diagonal dominance structure in $\mathbf{R}$:

$$|\mathbf{R}_{ii}|^2 \geq \sum_{j=1}^{k} |\mathbf{R}_{jk}|^2, \;\; 1 \leq i \leq k \leq r. \tag{3.14}$$

Constraints are imposed in the final $r-s$ steps of pivoting, ensuring that the largest contributing terms in the objective function expansion remained unaffected:

$$\log\det((\mathbb{S}\boldsymbol{\Psi}_{\boldsymbol{r}})^T\mathbb{S}\boldsymbol{\Psi}_{\boldsymbol{r}}) = \log\left(\prod_{i=1}^{r}\mathbf{R}_{ii}^2\right) = \log\mathbf{R}_{11}^2 + \log\mathbf{R}_{22}^2 + \cdots + \log\mathbf{R}_{(r-s)(r-s)}^2 + \cdots + \log\mathbf{R}_{rr}^2.$$

The main driver of this optimization is the point at which constraints are introduced into the pivoting procedure, as allowing upper triangularization to proceed normally in the starting iterations maximizes the leading diagonal entries of $\mathbf{R}$, ensuring that domain-specific constraints do not drastically affect the diagonal dominance property, but only the trailing $\mathbf{R}_{ii}$, which are optimized by choosing the best pivot from the allowable locations. The three types of spatial constraints handled by the algorithm (Figure 3.1) are:

1. **Region constrained:** This type of constraint arises when we can place either a *maximum* of or *exactly* s sensors in a certain region, while the remaining $r-s$ sensors must be placed outside the constraint region.

    - **Maximum:** This case deals with applications in which the number of sensors in the constraint region should be less than or equal to s. In each iteration a pivot column (sensor location) is chosen from the set of all columns until s selected pivots lie in the constrained region. Successive pivots with the largest 2-norm are selected from among the unconstrained column indices.

- **Exact:** This case deals with applications in which the number of sensors in the constraint region should equal s. The algorithm follows the same procedure as the maximum sensor placement case if the number of sensors in the constraint region equals or exceeds s. However, if there are fewer than s sensors in the constrained region, the algorithm forces the deficit of sensors to be placed in the constraint region at the end of the pivoting procedure.

2. **Predetermined:** This type of constraint occurs when a certain number of sensor locations are already specified, and optimized locations for the remaining sensors are desired. The strategy employed selects pivots from among all column indices of $\mathbf{R}_{22}^{(k)}$ until the iterate k equals $r - s$, then imposes the selection of user-specified sensor locations in the final s iterations.

3. **Distance constrained:** This constraint enforces a minimum distance d between selected sensors. Accordingly, the first pivot is the column index of $\mathbf{\Psi}_r^T$ with maximal 2-norm, the default (unconstrained) base step. The $(k+1)^{\text{st}}$ iterate now selects the pivot column with maximal 2-norm from among the remaining columns of $\mathbf{R}_{22}^{(k)}$ that are at least distance d away from the previous k selected sensors. This is an *adaptive* constraint because the set of allowable sensor indices is updated with each pivoting iteration to remove the d-neighborhood of the kth sensor.

Although we mainly consider the minimal allowable number of sensors to be $p = r$, the truncation rank of the basis, additional sensors can be added for redundancy and robustness through the oversampling optimization proposed by B. Peherstorfer et al [124].

Algorithm 1 QR Pivoting with Adaptive Constraints

```
**Input:** $\mathbf{W}$ = Input matrix, $s_c$ = Constrained/Predetermined sensor indices, $s$ = indices allowed in the constrained region/ Total predetermined sensors, CONSTRAINTS = Type of Constraint, $d$ = Distance from previous sensors
**Output:** Sensor indices
**Function Call:** $\gamma$ = CONSTRAINEDQR($\Psi_r^T$, CONSTRAINTS, $s_c$=[], $s$=[], $d$=2)
procedure CONSTRAINEDQR($\mathbf{W}$, CONSTRAINTS,$s_c$,$s$,$d$)
    $r, n \leftarrow$ SIZE($\mathbf{W}$)                                ▷ $r$ = number of desired sensors
    $\mathbf{R} \leftarrow$ COPY($\mathbf{W}$)
    $\mathbf{Q} \leftarrow eye(m)$
    $\gamma \leftarrow [1, 2, \ldots, n]$                                ▷ sensor index set
    for all $k \in 1, ...., r$ do
        $dlens \leftarrow$ COMPUTECONSTRAINTS($dlens$,$\gamma$,CONSTRAINTS, $k$,$s_c$,$s$,$d$)
        $l \leftarrow \operatorname{argmax} dlens$
        $\boldsymbol{\nu} \leftarrow \mathbf{R}[k : m, k - 1 + l]$
        SWAP($\mathbf{R}[k : m, k], \mathbf{R}[k : m, k - 1 + l]$)
        SWAP($\gamma_k, \gamma_{k-1+l}$)                              ▷ update $k$th sensor
        $u \leftarrow$ HOUSEHOLDER($\boldsymbol{\nu}$)                        ▷ compute $\mathbf{H}(\boldsymbol{\nu})$
        $\mathbf{R}[k : m, k : n] \leftarrow (I - 2uu^T)\mathbf{R}[k : m, k : n]$
        $\mathbf{Q}[:, k : n] \leftarrow (I - 2uu^T)\mathbf{Q}[:, k : n]$
    return $\gamma_{1:r}$
```

3.5 Uncertainty Estimation

Under noisy measurements, errors in estimation are transmitted into reconstruction errors. Geometrically, estimation errors are characterized by (hyper-)ellipsoids in r dimensions whose axes describe these errors. Statistically, the confidence intervals for the estimation of states

Algorithm 2 Subroutine for Constraints

```
**Input:** $s_c, s, r, d$, CONSTRAINTS (see Algorithm 1), $dlens$ = $\mathbf{R}$ column norms, $\gamma$ = sensor index set, $k$ = current sensor index
**Output:** $dlens$
**procedure** COMPUTECONSTRAINT($dlens$,$\gamma$,CONSTRAINTS,$k$,$s_c$, $s$,$r$,$d$)
    **if** CONSTRAINTS = RegionConstrainedMax **then**
        **if** $|\gamma| \in s_c < s$ **then**
            $dlens = dlens$
        **else**
            $dlens[s_c] = 0$
    **else if** CONSTRAINTS = RegionConstrainedExact **then**
        **if** $|\gamma| \in s_c < s$ **then**
            $dlens = dlens$
            **if** $r > k \geq (r - (s - |\gamma|)$ **then**
                $dlens[!s_c] = 0$
        **else**                                    ▷ Number of sensors in constrained region > $s$
            $dlens[s_c] = 0$
    **else if** CONSTRAINTS = Pre-determined **then**
        **if** $k = (r - s)$ **then**
            $dlens[!s_c] = 0$
    **else** CONSTRAINTS = DistanceConstrained
        **if** $p \in dlens$ **and** $\|p - \gamma[:]\|_2 \leq d$ **then**
            $dlens[p] = 0$
```

are characterized by the η-*confidence ellipsoid* that contains $\mathbf{a} - \hat{\mathbf{a}}$ with probability η

$$E_\alpha = \{\mathbf{z} | \mathbf{z}^T \mathbf{\Sigma}^{-1} \mathbf{z} \leq \alpha\}, \tag{3.15}$$

where $\mathbf{\Sigma}$ is the covariance matrix in Equation 3.9 and $\alpha = F^{-1}_{\chi^2_n}(\eta)$ is the cumulative distribution function of a χ-squared random variable with r degrees of freedom. An important scalar measure of the quality of estimation is the volume of this ellipsoid

$$\mathbf{vol}(\epsilon_\alpha) = \frac{(\alpha\pi)^{r/2}}{\Gamma(\frac{r}{(2+1)})} \det \mathbf{\Sigma}^{1/2} = \frac{(\alpha\pi)^{r/2}}{\Gamma(\frac{r}{(2+1)})} \det((\beta^2((\mathbb{S}\mathbf{\Psi}_r)^T(\mathbb{S}\mathbf{\Psi}_r))^{-1})^{1/2}), \tag{3.16}$$

where Γ is the gamma function. D-optimal designs minimize the volume of the ellipsoid, which is inversely proportional to the determinant of our information matrix. A small volume for the η-confidence ellipsoid implies a strong correlation between the estimation errors in each component. Under Gaussian noise assumptions, 3σ standard deviations computed from the diagonal entries of the covariance matrix Σ_{ii} measure the uncertainty in predicting the i^{th} component, establishing error bounds for reconstructing flows from noisy measurements.

The following text, for ease of notation, uses $\Theta = \mathbb{S}\mathbf{\Psi}_r$ to signify the mode measurement matrix, hence $\mathbf{\Sigma} = \Theta^T\Theta$ represents the Fisher Information. In order to quantify the uncertainty in each reconstructed component of the state under noisy measurements, we analyze the expected covariance of the full state fluctuations. Klishin et al [88] provide the following estimate of the expected state covariance for a regularized gappy estimator, which now depends on the covariance of our measurement model as follows

$$\mathbb{E}[\Delta\hat{\mathbf{x}}\Delta\hat{\mathbf{x}}^T] = \Psi_r \frac{\mathbf{\Sigma}^{-1}}{\beta^2}\Theta^T\mathbb{E}[\Delta y \Delta y^T]\Theta\frac{\mathbf{\Sigma}^{-1}}{\beta^2}\Psi_r^T, \tag{3.17}$$

where $\mathbb{E}[\Delta y\Delta y^T] = \beta^2\mathbf{I}$ for uncorrelated noise. The standard deviation in the reconstruction of each grid-point can be calculated through the diagonal entries of this matrix, providing an uncertainty heatmap of the whole reconstructed domain based on the sensor configuration $\mathbb{S}$ [88]

$$\begin{aligned} \mathbf{F} &\equiv \Psi_r\mathbf{\Sigma}^{-1}\frac{\Theta^T}{\beta^2} \\ \sigma_i &= \beta\sqrt{\sum_j (\mathbf{F}_{ij})^2}. \end{aligned} \tag{3.18}$$

Furthermore, model recalibration for digital twinning can be informed by analyzing the distribution of each component of the estimated coefficients $\hat{\mathbf{a}}$, even when the true coefficients are unavailable. The predicted mean $\mu_i = \mathbb{E}[\hat{\mathbf{a}}_i]$ is estimated by averaging measurements over the training data

$$\mathbb{E}[\hat{\mathbf{a}}_i] = \boldsymbol{\Sigma}^{-1}\frac{\Theta^T}{\beta^2}\mathbb{E}[\mathbf{y}_i] \tag{3.19}$$

where $\mathbf{y}_i$ are each component of noisy measurements with standard deviation β. Similarly, we can estimate the expected covariance in components of $\hat{\mathbf{a}}$ using the diagonal entries of

$$\mathbb{E}[\Delta\hat{\mathbf{a}}\Delta\hat{\mathbf{a}}^T] = \frac{\boldsymbol{\Sigma}^{-1}}{\beta^2}\Theta^T\mathbb{E}[\Delta y\Delta y^T]\Theta\frac{\boldsymbol{\Sigma}^{-1}}{\beta^2}. \tag{3.20}$$

The diagonal part $\mathbf{T}$ of the covariance matrix can be used to calculate the standard deviation in the distribution of the estimated POD coefficients.

$$\begin{aligned} \mathbf{T} &\equiv \boldsymbol{\Sigma}^{-1}\frac{\Theta^T}{\beta^2} \\ \sigma_i &= \beta\sqrt{\sum_j (\mathbf{T}_{ij})^2}. \end{aligned} \tag{3.21}$$

The predicted standard deviation and mean of the POD coefficients together provide statistical metrics to measure uncertainty in the reconstruction of the flow field due to noise measurements when true readings are unavailable. In nuclear digital twins these error bounds can be used to detect the divergence of sensor readings from expected values. Statistics of the error provide means to “flag” or “signal” re-calibration of the digital twin, detect anomalies and classify erroneous readings.

3.6 Results

This section demonstrates the constrained and unconstrained sensor placement algorithm on a randomly generated state space system, the 2D heat diffusion through a thin plate, and the OPTI-TWIST prototype. In the randomized system, all possible sensor placements given a fixed budget of sensors are computed to demonstrate the near optimality of our approach. Next, we investigate reconstruction of temperature fields in 2D heat diffusion with a constant heat source, a simplified model of the OPTI-TWIST heater. Uncertainty analysis is conducted on noisy measurements for varying signal-to-noise ratio (SNR). Using constrained optimized sensor placement with our approach, we reconstruct, with minimal error, the flow field inside OPTI-TWIST—in comparison to randomly selected sensor locations.

3.6.1 Discrete Random State Space System

We first demonstrate the near optimality of constrained QR pivoting by using a low-dimensional linear time-invariant (LTI) system. The dimensionality of this system is small enough to enumerate all possible placements in order to empirically compare the constrained QR placements with the optimum placements. Consider the following LTI system:

$$\dot{\mathbf{x}} = \mathbf{A}\mathbf{x} + \mathbf{B}\mathbf{u} \qquad \mathbf{x} \in \mathbb{R}^n, \mathbf{u} \in \mathbb{R}^q \tag{3.22a}$$

$$\mathbf{y} = \mathbf{C}\mathbf{x} \qquad \mathbf{y} \in \mathbb{R}^p \tag{3.22b}$$

with randomly generated system $\mathbf{A}$, measurement $\mathbf{C}$, and actuation $\mathbf{B}$ matrices sampled i.i.d. from a normal distribution, $n = 25$ states and $p = q = 25$ randomized measurements and actuators, respectively. $\mathbf{x}$, $\mathbf{u}$, and $\mathbf{y}$ represent the state, input, and output vectors, respectively. We empirically studied the optimality of our proposed algorithm by computing all possible $r = 7$ sensor selections, leading to a brute force search of $\binom{n}{r} = 480,700$ choices of $\mathbb{S}$. The log determinant of $\mathbb{S}\boldsymbol{\Psi_r}$ was evaluated for all possible combinations of the seven sensors, then binned into the histogram shown in Figure 3.2a. This computation is only tractable for a small state dimension—as even for $n = 100$, the brute-force search results in $O(10^{10})$ complexity. The optimization outcome (determined via Equation 5.12) for sensors selected using the QR pivoting approach is represented by the solid black line in Figure 3.2a. This sensor selection is observed to be nearly D-optimal, exceeding 99.74% of all candidate placements.

We studied region-constrained pivoting by allowing only $s \leq 2$ sensors to be selected from the first $s_c = 5$ components of the state (the constraint region). A brute-force search across all possible combinations of s sensors in the constraint region (and $r - s$ elsewhere) was carried out, resulting in $\frac{(n-s_c)!}{(n-s_c-(r-s))!(r-s)!}\frac{s_c!}{(s_c-s)!s!} = 155,040$ possible combinations in selecting the seven sensors binned in Figure 3.2b. Figure 3.2b compared our first strategy

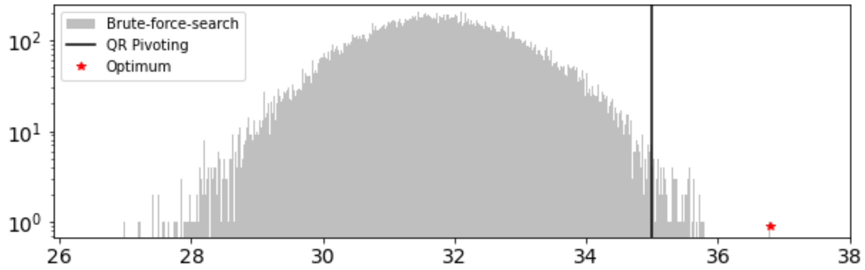

(a) Unconstrained QR pivoting

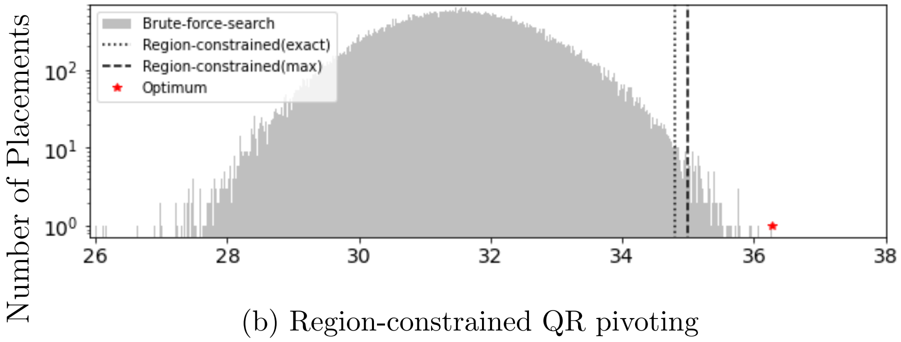

(b) Region-constrained QR pivoting

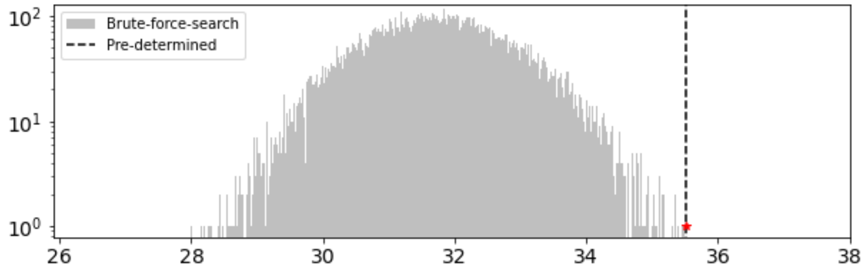

(c) User-specified QR pivoting

Figure 3.2: Enumeration of $\log\det(\mathbb{S}\boldsymbol{\Psi_r})^T(\mathbb{S}\boldsymbol{\Psi_r})$ (X-axis) over all possible placements of 7 out of 25 candidate locations (100,000-500,000 possible placements binned into histograms). The introduction of constraints into QR optimization results in a log determinant that is near optimal (optimum shown in red) for the three types of constraints.

(i.e., placing exactly $s = 2$ sensors in the constraint region in the first two iterations of pivoting (dotted line)) with another strategy in which a maximum of two sensors were allowed in the constraint region throughout the pivoting procedure (dashed line). Our exact approach has a log determinant exceeding 99.78% of all possible region-constrained sensor placement options, while the max approach is observed to exceed 99.87% of all possible combinations. Thus, both approaches provide a near-optimal subset of region-constrained sensors for reconstruction.

In predetermined sensor placement, a specified number s of sensors were selected in advance, leaving the algorithm to optimize those that remain. Our strategy runs unconstrained QR pivoting to select the first $r - s$ pivots (sensors), then selects the predetermined sensors in the remaining s pivoting iterations. The results of the log determinant objective evaluated for our optimization strategy (dashed line) are compared against a brute force search across all possible candidate placements that contain the two predetermined sensors reflected in Figure 3.2c. Our strategy outperforms 99.99% of all possible placements, exhibiting near-optimal solutions. These results show that the introduction of constraints results in minimal distance to the true optimum. We analyze the negligible effect of this distance on the reconstruction error

$$\text{Relative reconstruction error}(\epsilon) = \frac{\|\mathbf{x} - \mathbf{\Psi}_r(\mathbb{S}\mathbf{\Psi}_r)^{\dagger}\mathbf{y}\|_2}{\|\mathbf{x}\|_2} \times 100. \tag{3.23}$$

We compared the reconstruction achieved via each set of constrained QR sensors with sensor placements sampled from the mean of the $\log\det$ distributions. (These represent the most likely sub-optimal sets to be chosen at random.) The reconstruction error for each of these randomly placed sensors was then calculated (see the blue violin plots in Figure 3.3, where the green square and circle reflect the reconstruction error of the QR-selected sensor locations for the different constraint cases). Random sensor placements with a sub-optimal $\log\det$ objective fall between 31 and 32, resulting in a highly inaccurate relative reconstruction error (ϵ) between 30 and 350. The QR-optimized strategy for unconstrained/constrained sensor placement results in significantly lower reconstruction error $\epsilon \sim \mathcal{O}(10^{-15})$:

We conclude that the proximity between the brute-force optimum and our greedy placements produces negligible loss in reconstruction performance. Vastly sub-optimal random

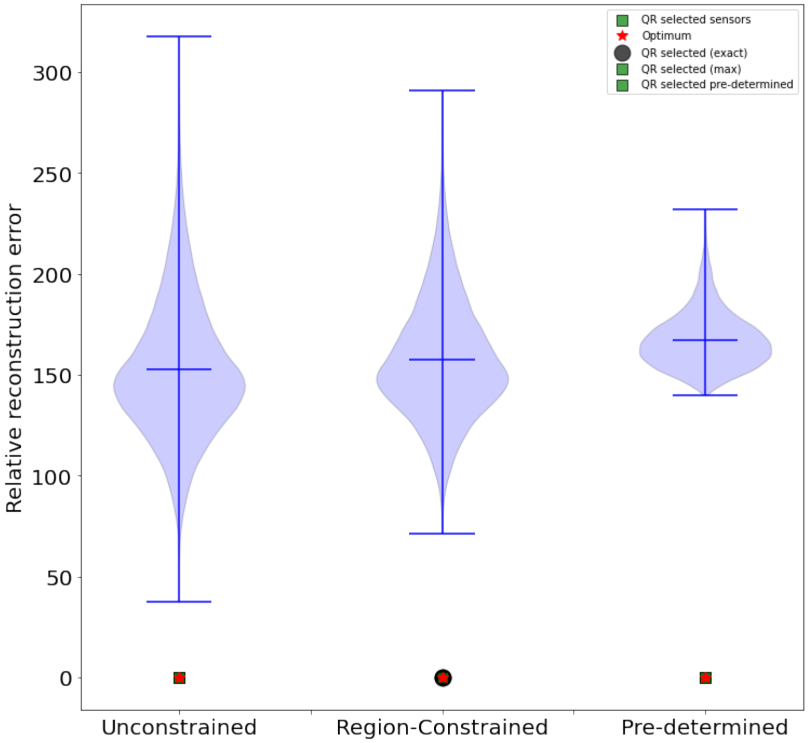

Figure 3.3: Proximity between the brute-force optimum and QR selected sensors for unconstrained, region-constrained, and predetermined sensor placement leads to orders of magnitude lower reconstruction error ($\epsilon \sim \mathcal{O}(10^{-15})$) compared to random placements. Incorporating constraints results in accuracy comparable to that of the optimal placement (red stars).

placements illustrate the inverse relationship between the objective function and performance: the lower the log determinant, the higher the reconstruction error. However, this system was randomly generated, and the dynamics do not evolve according to localized features in state space that allow one sensor to capture information on spatially correlated states. Next, we demonstrate the algorithm on a heat diffusion model that allows for spatial and physical interpretation of the resulting sensors.

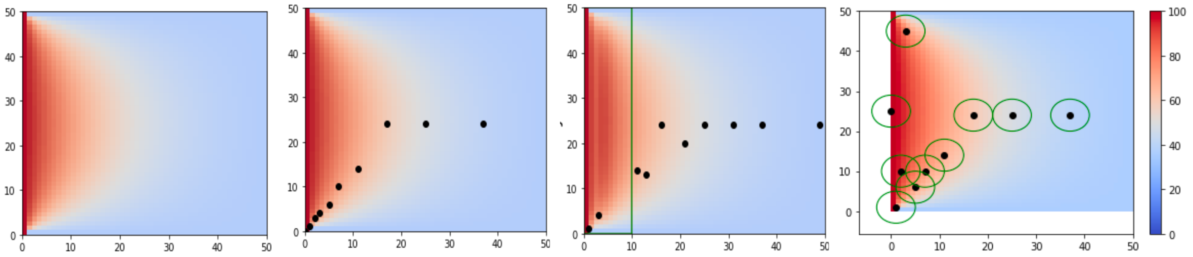

(a) Ground Truth (b) QR $\epsilon = 0.0064$ (c) Exact,Max $\epsilon = 1.5085$ (d) Distance $\epsilon = 0.0103$

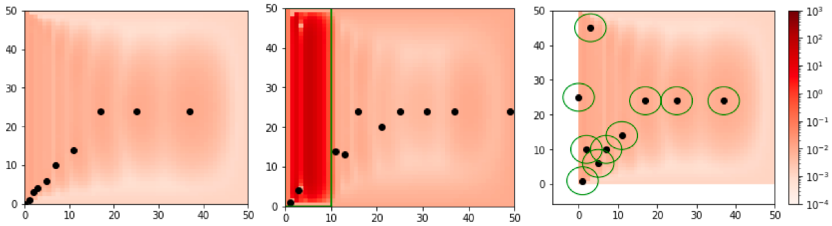

(e) QR (f) Exact,Max (g) Distance

Figure 3.4: Uncertainty heatmaps (e,f,g) correspond to placements/reconstructions (b,c,d) respectively. Reconstruction of the temperature field at $t = 1000$, based on the different constraints demonstrate that constraining sensors far away from the heater region result in higher reconstruction error (c,d) and higher uncertainty (f,g) than unconstrained optimization (b,e) respectively, which favors sensors adjacent to the heat source.

3.6.2 2D Heat Flow through a Thin Plate

Temperature fields are reconstructed via constrained/unconstrained sensor placement in a 2D plate undergoing thermal diffusion from a heat source, based on a simplified model of the OPTI-TWIST diffusion. Temperatures at the boundaries are fixed at 100°C at $x = 0$, and 36°C elsewhere in ∂D. The initial temperature throughout the domain D at $t = 0$ is also

36°C. Heat transfer from the heat source over the domain is governed by the heat equation

$$\begin{aligned} &u_t = \alpha(u_{xx} + u_{yy}) && x, y \in D \\ &u(x, y, t) = 36 && x, y \in \partial D \setminus x = 0 \\ &u(0, y, t) = 100 && \end{aligned}$$

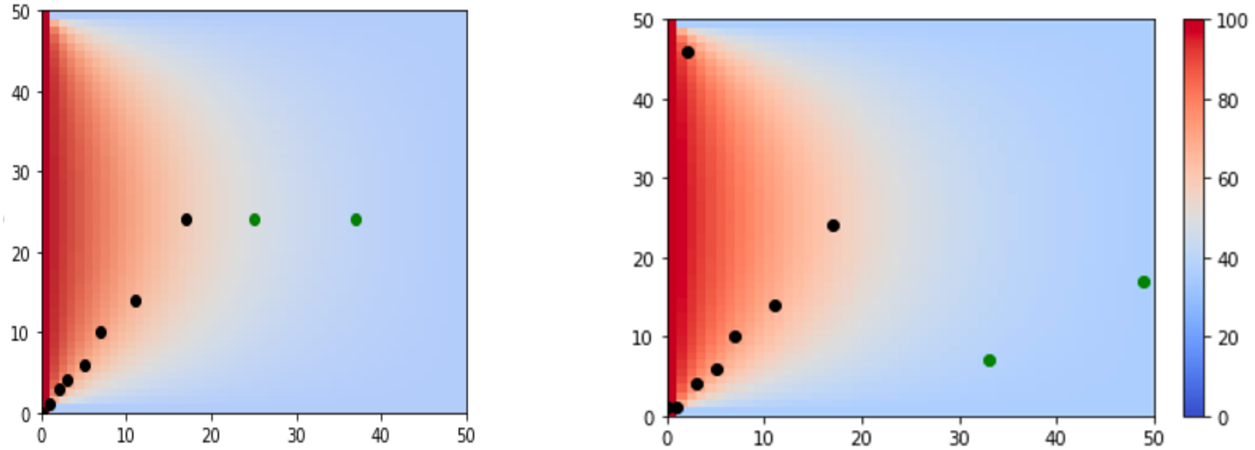

(a) Pre $\epsilon = 0.0127$

(b) Pre $\epsilon = 0.0111$

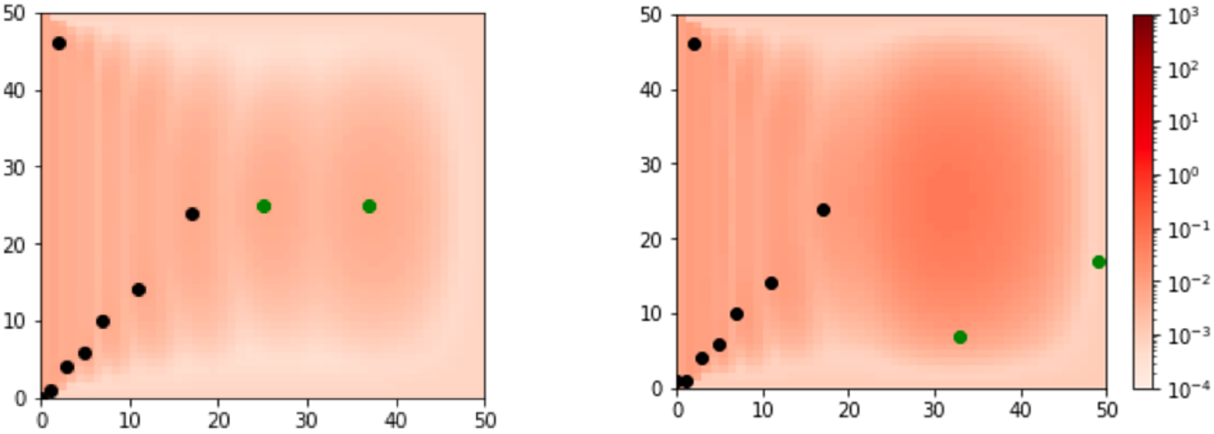

(c) Pre

(d) Pre

Figure 3.5: Two different pre-determined sensor layouts (a,b-shown in green) may lead to similar reconstruction errors (a,b) but increase reconstruction uncertainty (d) when sensors are distant from QR-optimal locations (c).

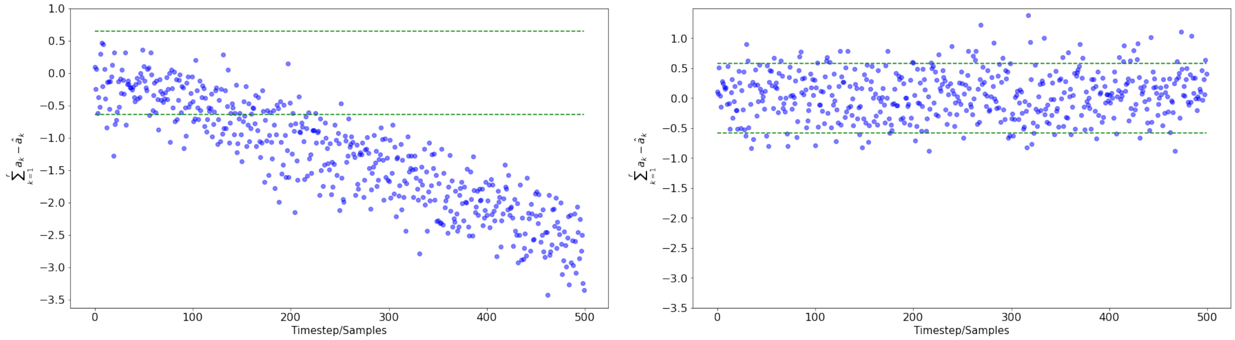

(a) Rank 10 model (b) Rank 20 model

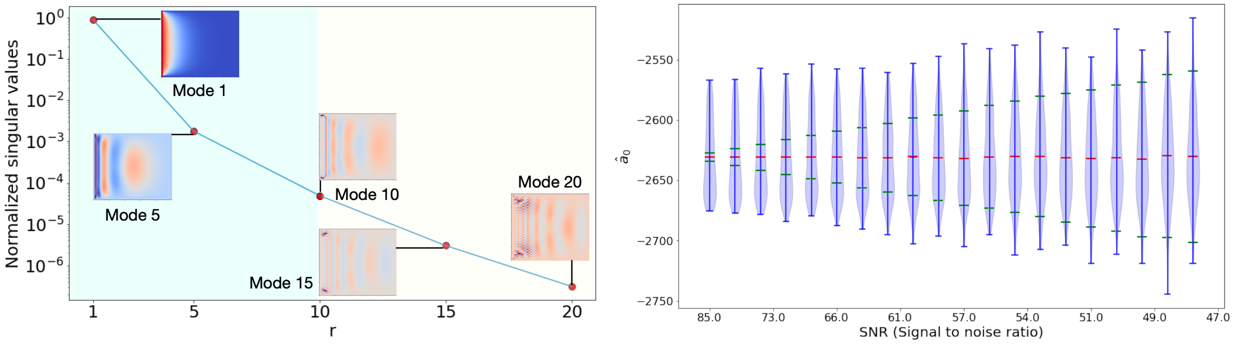

(c) Leading POD modes by energy contribution. (d) Uncertainty in $\hat{\mathbf{a}}_k$ estimates rise as SNR decreases.

Figure 3.6: Uncertainty estimation reveals rank 10 models are not sufficiently descriptive of dynamics after t =100s (a) under noisy measurements. A higher rank 20 approximation is required (b) despite the leading 10 POD modes capturing 99% of the energy (c). Predicted statistics of the estimated coefficients, such as the standard deviation 3σ (green) and mean (red) effectively bound the estimated $\hat{\mathbf{a}}_0$ under increasing noise.

where u is the desired temperature and $\alpha = 2\,(\mathrm{mm}^2/\mathrm{s})$ is the thermal diffusivity constant. The solution of the partial differential equation is simulated for 1000 time steps using finite differences with $\Delta x, \Delta y = 1$ and $\Delta t = 0.125$. We reconstruct the temperature fields and analyze the uncertainty in reconstruction of each pixel due to adding i.i.d. Gaussian noise $\boldsymbol{\eta} \sim \mathcal{N}(0, 0.01)$ to the measurements for the unconstrained, constrained (Figure 3.4), and predetermined optimized sensor placements (Figure 3.5). A total of $r = 10$ sensors are selected for reconstruction, and $s = 2$ sensors are allowed in the constrained region or are predetermined. Distance constraints impose a Euclidean distance of at least 2 between selected sensors.

Similar to the nuclear OPTI-TWIST (subsection 3.6.3), optimized placements favor sensors near the heat source. Constraining sensors away from the heat source results in higher reconstruction errors and uncertainty than unconstrained optimization. In this example, both region-constrained max and exact ($s = 2$ within $x < 10$) optimization result in identical sensor placements (Figure 3.4c), with only two sensors near the heat source. This results in higher error because of high-energy modal contributions adjacent to the heater (Figure 3.6c). Removing heater adjacent sensors results in higher uncertainty of approximately 10°C near the heater (Figure 3.4f). The distance-constrained sensor placements, which also placed six sensors near the heat source, result in the lowest reconstruction error under constraints (Figure 3.4d). When predetermined sensor locations are close to the unconstrained optimal locations as in Figure 3.5a, the reconstruction errors and uncertainty are low (Figure 3.5c). Optimized sensor locations (unconstrained) are placed along the propagating wavefront, as in the two rightmost sensors. Fixing predetermined sensor locations away from this wavefront results in a noticeable increase in reconstruction uncertainty in the right half of the domain (Figure 3.5d), and strengthens the case for data-driven placement strategies. The optimized sensors reflect the highest energy amplification in the POD modes, which occur near the heat source (Figure 3.6c). The leading POD modes capture this diffusion of heat from the heat source boundary to the rest of the domain (Figure 3.6c). Approximately 96% of the cumulative energy is captured by the leading two POD modes, while the remainder capture only 4%.

Gappy POD was used to estimate the rank 10 and rank 20 model coefficients from noisy measurements (test dataset of 500 snapshots), and compare estimation errors with our predicted uncertainty analysis to test the descriptive capability of the different rank truncations. The standard deviations σ_i computed from the diagonal entries of the covariance matrix $\mathbf{\Sigma}_{ii}$ measures the uncertainty in predicting the ith component. Approximately 498.5 out of 500 reconstruction errors should lie within $3\sigma_i$ of the mean. As more modes are included in the POD approximation, the selected sensors capture more information about the underlying physics of heat diffusion. As seen in Figure 3.6, the rank 10 POD model fails to capture the underlying physics after time interval $t = 100$, whereas the rank 20 model is more descriptive of the dynamics over a longer time interval $t = 500$. With more modes and sensors, the error covariance in each component narrows and the 3σ bounds become tighter.

When clean measurements or ground truth coefficients are unavailable, bounds on distributions of estimated $\hat{\mathbf{a}}$ are useful to inform recalibration of digital twins. The uncertainty estimation for any POD coefficient, for example $\hat{\mathbf{a}}_0$, can be bounded using the predicted standard deviation or 3σ (Equation 3.21, shown in green in Figure 3.6d) and mean (Equation 3.19, shown in red in Figure 3.6d). As the SNR decreases, the dynamics of heat diffusion are corrupted by noise, resulting in wider distributions of the estimated state. Note that predicted uncertainty bounds are more accurate at higher noise levels due to numerical rank approximation error overwhelming the low noise contribution to error. In other words, uncertainty analysis is more accurate under larger ratios of measurement noise to model error.

In summary, when uncertainty in sensor measurement is known, this framework enables estimation of the expected error distribution as a function of measurement noise, as well as study of the growth in error as the sensor noise increases. When sensor uncertainty is unknown, filtering and Bayesian inference techniques may be used for uncertainty quantification with these linear embeddings. The developed algorithm can handle reconstruction of flow fields in the presence of constraints and noise with high accuracy. Uncertainty analysis of predicted states plays a key role in detecting erroneous readings in digital twins. In the next example we reconstruct temperature flow field for a gravitational advection driven physical system, OPTI-TWIST.

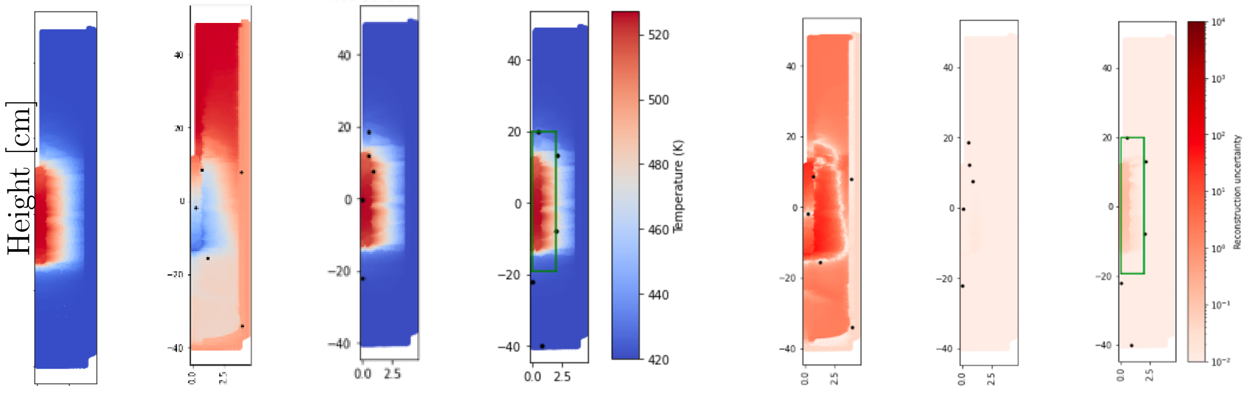

(a) Truth (b) Random (c) QR (d) Constrained (e) Random (f) QR (g) Constrained

Figure 3.7: Unconstrained optimization places sensors near the heater region (c), resulting in highly accurate reconstruction with $\epsilon = 0.168$ (a), with constrained optimized sensors resulting in comparably high accuracy $\epsilon = 0.174$ (d). Random sensor placement (b) results in inaccurate reconstructions ($\epsilon = 25.24$) and large estimation uncertainty (e) compared to that of optimized sensor locations (f,g).

3.6.3 Steady-state Simulation of the OPTI-TWIST Prototype

The next example follows the new design paradigm suggested by digital twins. In traditional design practice, modeling and simulation insights are often leveraged at the experimental design stage in order to build physical models and place sensors. However, limitations regarding space, installation, cost, and signal fidelity of the experimental device pose challenges in deploying the desired number of sensors. Our holistic approach integrates experimental constraints, Computational Fluid Dynamics (CFD) simulations, and optimization objectives (reconstruction) in a principled way to optimize the placement of sensors in the design phase of the digital twin.

Here, our sensor placement optimization is demonstrated on the OPTI-TWIST prototype, which is electronically heated to mimic the neutronics effect of TWIST prior to insertion into a reactor at INL. Temperature is the field of interest, and point thermocouples will be used as the sensors. The OPTI-TWIST prototype was designed to simulate thermal-hydraulics behavior of TWIST during irradiation in the reactor, as well as to measure the effect of loss of coolant on the fuel rodlet temperature. In OPTI-TWIST, the fuel-rod specimen is replaced by an instrumented electric cartridge heater, and loss of coolant is controlled by a quick-opening valve at the bottom of the capsule. To provide the temperature fields necessary to train the sparse sensing algorithm, a simplified 2D CFD model of the OPTI-TWIST geometry is developed using StarCCM+ (Figure 3.8) [125].

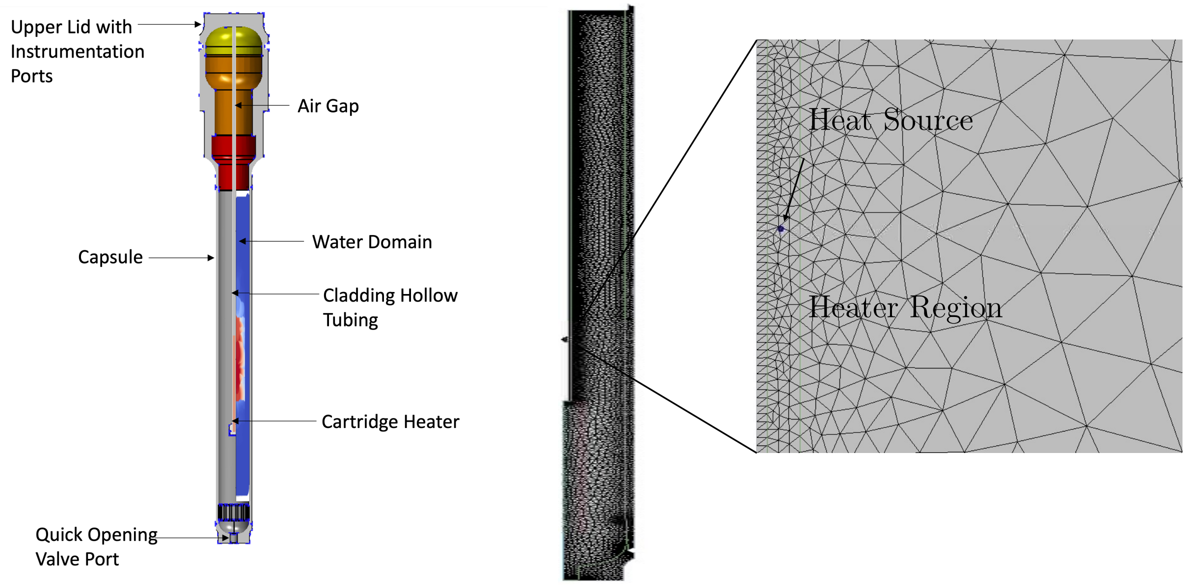

(a) Schematic (b) Mesh

Figure 3.8: The axial symmetry of the OPTI-TWIST is exploited by simulating only half the domain as the cartridge heater is placed at the center of the capsule. The geometry and mesh reveal richer dynamics near the heater region.

The CFD model accounts for steady-state turbulent natural circulation conditions, including two controlled parameters: heater power ($\dot{q}$) and outer surface temperature (T_{sur}). These two controlled parameters (i.e., heater power and surface temperature) were varied,

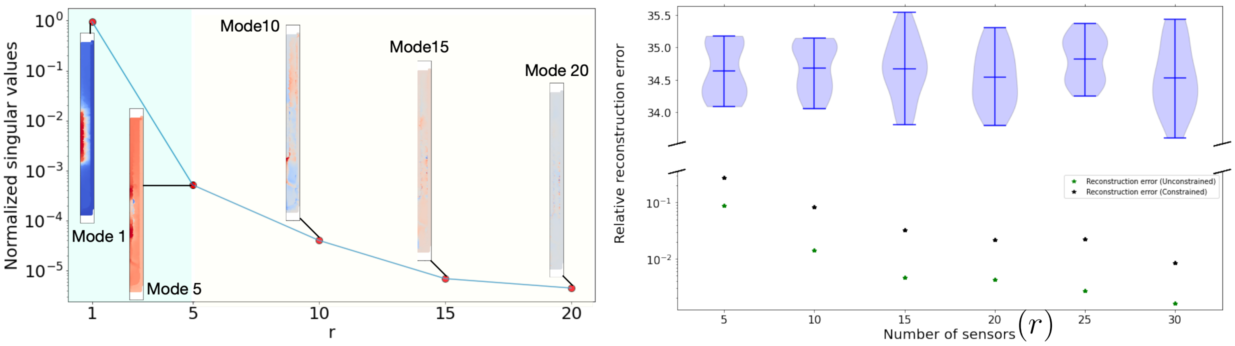

(a) Leading POD modes and energy contribution.

(b) Error Study

Figure 3.9: An informed trade-off between reconstruction accuracy and number of sensors is possible for QR optimized sensors. The leading POD modes capture 99% of energy content and just 5 sensors are enough to obtain a accurate reconstruction with $\epsilon \sim \mathcal{O}(10^{-1})$ (a). QR selected sensor accuracy increases with an increase in the number of sensors as compared to random placements that produce orders of magnitude larger relative reconstruction errors (b).

while keeping the initial temperatures ($T_0 = 300$K) and the system pressure ($P_{sys} = 2250$psi) constant throughout. The data are comprised of 49 steady-state temperature fields resulting from seven heater powers and surface temperatures uniformly sampled at 350–650W and 240–420K, respectively. The convergence criterion was the maximum liquid temperature, which showed negligible fluctuations after 2000 time steps. First, our optimization is run on the steady-state temperature fields, resulting in the unconstrained optimal placement shown in Figure 3.7c. Unconstrained optimization selects three sensors near the heater (Figure 3.7c); however, space restrictions make these heater-adjacent locations experimentally infeasible. Enforcing sensor constraints to lie outside the heater region results in a reconstruction error of $\epsilon = 0.174$—an increase of only .006. Figure 3.7b contrasts these optimized sensor reconstructions with ensembles of randomly placed sensors. Observe that $\epsilon_{unconstrained} < \epsilon_{constrained} \ll \epsilon_{random}$, i.e. placing sensors in random locations leads to significantly larger reconstruction errors (Table 3.2).

Gaussian i.i.d. noise $\boldsymbol{\eta} \sim \mathcal{N}(0, 0.01)$ is added to the measurements to analyze the uncertainty heatmaps in reconstruction of the true temperature profile. Removing sensors from heater-adjacent locations leads to an increase of approximately 0.5K in the uncertainty in reconstruction of the flow field close to the heater (Figure 3.7g) compared to uncertainty resulting from unconstrained sensor placement (Figure 3.7f). The uncertainty in reconstruction is higher by 40-50K throughout the domain when sensors are placed randomly (Figure 3.7e). Stratified contours of reconstruction errors occur where random sensors fail to accurately capture the transition between hot and cold (Figure 3.7b). Therefore, randomly placed sensors fail to capture heater-correlated fluctuations and result in higher reconstruction errors and uncertainty.

The leading two POD modes, which drive approximately 99% of the energy content, capture the heat advection from the heat source. Thus, only five sensors—corresponding to the first five POD modes—are required to reconstruct the flow with high accuracy. The cumulative energy content, along with a visualization of the first three POD modes, is given in Figure 3.9a. These POD modes capture the interfaces between lower and higher temperatures as the advection flow progresses for different operating ranges. Sensors placed at random locations fail to capture the underlying physics of the system. Increasing the number of

Sensor Placement	Optimization Objective	Reconstruction Error (ϵ)
Unconstrained	5.432829081027846e-10	0.168
Constrained	4.534195929074569e-11	0.174
Random	1.026196077627373e-12	25.24

Table 3.2: Summary of the relative reconstruction error (ϵ) and optimization criteria ($\log|\det \mathbb{S}\boldsymbol{\Psi}_{\boldsymbol{r}}|$) for sensor placement given in Figure 3.7.

random sensors selected does not significantly improve the reconstruction of the flow field. An ensemble of sensors placed at random locations produces large relative reconstruction errors that average approximately 35 as the number of sensors is increased from 5 to 30, as seen in Figure 3.9b. Random placement of sensors increases the reconstruction error by ten orders of magnitude. The random placement strategy alludes to data-agnostic sensor placement at best-guess locations for reconstructing temperature fields.

Unconstrained optimization favors locating sensors close to the heat source, due to the richer dynamics that exist there. Imposing sensor constraints within QR results in a near-optimal placement outside this region, as well as negligible loss of reconstruction performance. Moreover, the error decreases with more optimized sensors (unconstrained or constrained); however, random placements still suffer from high error even with additional sensors. Therefore, placing or adding sensors without optimizing them in regard to the underlying flow or deployment constraints can introduce large errors in the corresponding digital twins especially in the presence of noisy sensor measurements—and may even cause sensor damage. Incorporating such considerations prior to setting up a physical experiment enables precise uncertainty quantification and helps validate the predictions of a digital twin.

3.6.4 Transient Simulation of the OPTI-TWIST Prototype

Analyzing the effect of power transients on reactor core coolant temperature, pressure, and velocity is essential for real-time safety monitoring and control of a nuclear reactor. Here, we optimize sensor placements to capture the dynamics of the heat flow when the heater power is varied as a transient. During transients it is essential to capture the instance when sensor readings start diverging from predicted metrics in the presence of noise. This can signal the need for model recalibration and can prevent accidents caused by power surges at a nuclear facility. The data is obtained from the 2D CFD model described in subsection 3.6.3 which runs for 600s, and is comprised of 1000 temperature fields sampled at every 0.6s. The heater transient power profile $P(t)$ can be described by

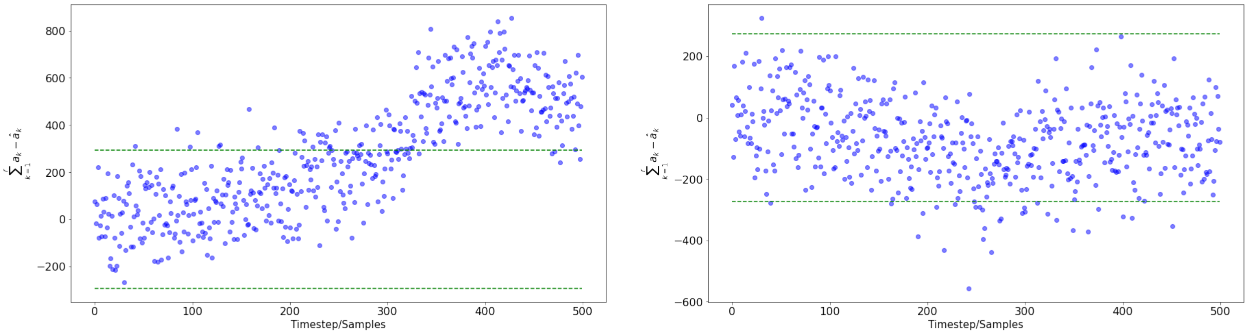

(a) Rank 10 model

(b) Rank 20 model

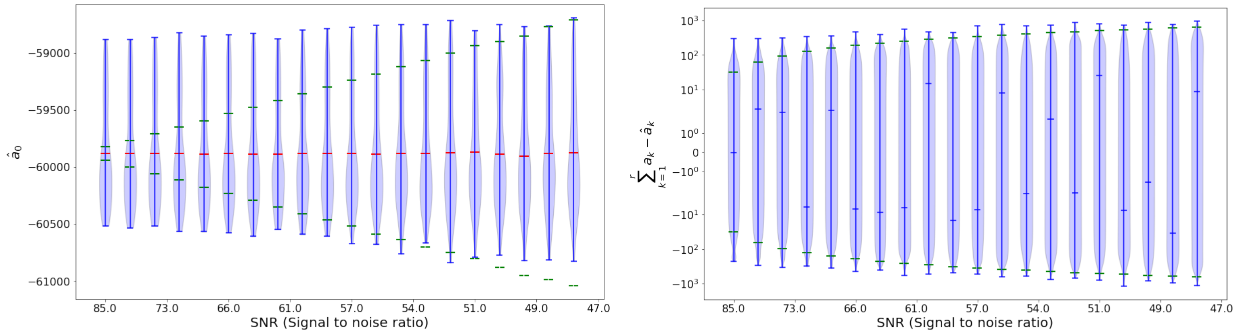

(c) Increasing uncertainty in estimation of $\hat{\mathbf{a}}_k$ with a decreasing SNR.

(d) Increase in estimation errors with a decreasing SNR.

Figure 3.10: (a) Uncertainty estimation reveals that a rank 10 model is not sufficiently descriptive of dynamics after t =300 under sensor noise. The rank 20 approximation (b) is valid over a longer time horizon of 500s of test data. As the SNR decreases, (c) POD coefficient variance increases, which propagates to an increase in uncertainty of estimation errors (d).

$$\begin{aligned}
&P(t) = P_o, \text{ if } t \leq t_1,\\
&P(t) = P_o + \frac{P_2 - P_o}{t_2 - t_1} * (t - t_1), \text{ if } t_1 \leq t \leq t_2, \qquad (3.24)\\
&P(t) = P_2, \text{ if } t_2 \leq t \leq t_3,
\end{aligned}$$

where $P_o = 10W, P_2 = 250W, t_1 = 200s, t_2 = 2t_1 \text{and}, t_3 = 3t_1$. Similar to the steady state temperature profile, richer dynamics are located in heater adjacent regions (Figure 3.11a). The unconstrained sensor layout shows a number of sensors near the heater (Figure 3.11c), however due to spatial constraints all sensors must be located away from the heater (Figure 3.11b). The increase in reconstruction error due to imposing constraints is as low as 1%. The algorithm is trained on the first 500 timesteps and reconstructs the temperature profiles at the last 500 timesteps from optimized sensors readings with additive i.i.d . Gaussian noise $\boldsymbol{\eta} \sim \mathcal{N}(0, 0.9)$.

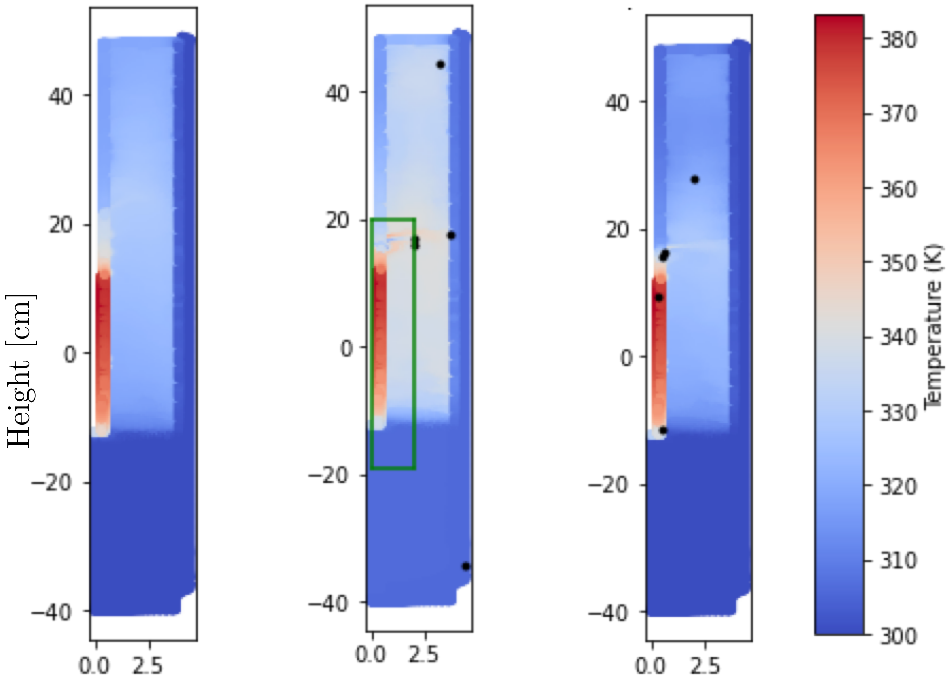

(a)Ground Truth (b)Constraint (c) QR

Figure 3.11: Heater-adjacent temperature fluctuations result in (c) sensors optimized close to the heater and a corresponding low reconstruction error $\epsilon = 1.026$. When constraints are imposed, sensors are placed outside the green constraint region (b), resulting in higher reconstruction error $\epsilon = 2.042$.

We study the reconstruction uncertainty using the predicted distribution of estimation coefficients in section 3.5. As shown in Figure 3.10, the rank 10 gappy POD model is insufficient to characterize the transient behavior in test data and reconstruction errors increase beyond the established bounds at $t = 200s$, whereas the rank 20 model captures the dynamics more effectively over the entire time horizon. When information regarding the true state is available, model recalibration can be signaled by bounds established for the error distribution in the presence of increasing noise (Figure 3.10d). When true coefficients are unavailable, the bounds established for the distribution of estimated POD coefficients $\hat{\mathbf{a}}_i$ can be used to flag erroneous readings. This uncertainty estimation of the flow field during transients ensures safe operating conditions during experimentation and testing of nuclear reactors.

3.7 Conclusion and Outlook

The reconstruction of reactor core flow fields using a limited budget of sensors has emerged as a critical enabler for real-time monitoring of nuclear assets. However, achieving near-optimal sensing in high-dimensional real-world systems extends beyond the nuclear industry and encompasses diverse fields such as biology, physics, aviation, and automotive industries. Engineering systems are subject to different constraints and limitations on sensors, making the selection and optimal placement of sensors while considering these constraints a crucial aspect of algorithm development. In this study, we have developed strategies for placing sensors to satisfy constraints related to sensor proximity, regional limitations on sensor quantity, and design or user prescribed locations. Through these strategies, we have demonstrated the effectiveness of adaptive sensor placement in satisfying constraints while maintaining optimality and accuracy of the reconstructed responses of interest. Moreover, we showcase the scalability and broad applicability of the algorithms on a variety of applications and constraints.

Nevertheless, more complex constraints may arise in nuclear, fluid, or aerospace applications in which the capability to achieve flow reconstruction based on sparse measurements is indispensable. For instance, in each reactor region the maximum number of allowable sensors is usually design-specific and cannot be exceeded. Moreover, an emerging practice during nuclear fuels tests is the use of distributed sensors (e.g., fiber-optic sensors or multipoint thermocouples). In fiber bragg grating (FBG), the refraction index changes along the sensor length and provides distributed measurements. Designing fiber optic sensors—which act as line sensors with different measurements at each point—is a novel challenge, as line sensors can be topologically shaped along various structures in engineering systems. Optimizing such topologies is another future direction for adaptive sensor placement. Fiber optic bundles are used for recreating high-quality images in both nuclear engineering and neuroscience. Optimizing the locations for these bundles to capture the best quality images is another interesting research direction.

Furthermore, it might be very costly to place sensors in certain areas of the reactor, due to the need for specially designed sensors capable of withstanding harsh working conditions. Other areas may entail spatial constraints. Thus, multi-objective optimization based on optimizing the sensor cost, spatial locations, as well as predicted dynamics will be essential. Time-dependent dynamics and the study of transients is invaluable in the nuclear field. Sensor placement based on time-dependent data from OPTI-TWIST and the use of dynamic mode decomposition or a nonlinear embedding such as autoencoders can help generalize to new physics scenarios, and will require new uncertainty estimates that can handle bias inherent to these types of models.

The ultimate goal is to extend the algorithms to inform users of optimal locations and timesteps to collect spatiotemporal sparse measurements to reconstruct core flow profiles during power transients. This should naturally evolve to the capability of performing optimal sensor placement for multi-class classification, where the algorithm must select the sensor network capable of predicting which accident scenario is more likely to occur faster than real time. Examples of such accident scenarios include Loss of Coolant Accident (LOCA), Reactor Initiated Accidents (RIA), and loss of power. These scenarios can be easily realized in a non-destructive fashion within the TWIST prototype by opening a valve, or suddenly shutting the heater power off. Data-driven sensing frameworks have the potential to identify sensor maps capable of detecting off-normal conditions, anomalies, and injected signals, enhancing resilience and security of the physical twin against cyber-attacks.

In the next chapter, we demonstrate the application of the constrained sensing and uncertainty estimation methodology to nuclear power plant components such as a steam generator, fuel capsules, and rodlets, to reconstruct heat flux, pressure and velocity.

Chapter 4

EXTENDING CONSTRAINED SENSOR OPTIMIZATION FOR MULTI-PARAMETER MONITORING IN NUCLEAR POWER PLANTS

Sensors and instrumentation are indispensable for nuclear power plants (NPPs) as they play an important role in nuclear safety, remote monitoring, model predictive control, as well as regulatory and reliability considerations. A typical pressurized water reactor (PWR)-type NPP consists of various systems, structures, and components such as the fuel, control rods, moderators, coolants, pressurizers, heat exchangers, steam generators, and condensers. These components function together to typically comprise the four subsystems within the NPP: reactor vessel, steam generator, coolant subsystem, and pressurizer subsystem, which require continuous monitoring and control. Accurate measurements and real-time data streaming capabilities of critical process responses such as power, coolant levels, temperature, velocity, pressure, neutron distribution are severely limited.

A nuclear fission chain reaction takes place in the reactor core, which contains the fuel, moderator, coolant, and control rods. Monitoring neutron flux is crucial for maintaining reactor power stability and controlling the reaction. The *reactor core monitoring system* uses neutron flux sensors to monitor core neutron flux under normal operation. It also detects conditions in the core that threaten the overall integrity of the fuel barrier due to excessive power generation. In PWRs and boiling water reactors (BWRs), ionization chambers and self-powered neutron detectors are used [126]. Temperature sensors such as thermocouples (TCs) and resistance temperature detectors (RTDs) monitor the core temperature to prevent overheating and ensure optimal performance [127].

The heat released by the nuclear reaction must be transferred from the fuel by the pri-

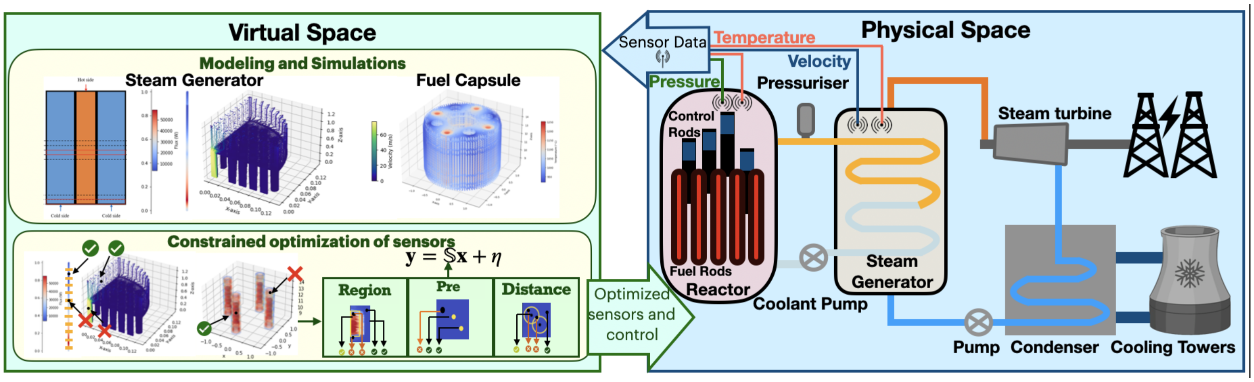

Figure 4.1: Optimized sensor placement in individual sub-systems of nuclear power plants allows real-time two-way communication between physical asset and it's digital twin.

mary coolant to maintain the fuel cladding temperature limit. In a PWR-type NPP, heat from the primary coolant is transferred to the secondary coolant in a steam generator to produce steam. Steam is then used to spin a turbine to generate electricity or for process heat applications.Within the *coolant circulation system*, ultrasonic and electromagnetic flow meters are used to measure coolant flow rates, ensuring proper cooling of the core [128]. Differential pressure transmitters and pressure gauges monitor the pressure within the coolant loop, preventing leaks or ruptures [112]. The heated coolant is used to generate steam that drives a turbine for electricity generation, as shown in Figure 4.1. In the *steam generation and turbine system*, microwave-based steam quality sensors assess the quality of steam generated, ensuring optimal efficiency in electricity production. Accelerometers and displacement sensors monitor turbine vibrations, preventing mechanical failures and ensuring operational safety.

Throughout the NPP, the *radiation monitoring system* is critical for personnel safety and environmental protection. Gamma and alpha/beta detectors detect and measure radiation levels in different areas of the plant. Sensor placement for control design and fault diagnosis of NPP subsystems is an integral part of instrumentation and control [129]. However, the complexity of the underlying physics, coupled with the constraints on sensor placements and their quantity, makes this task highly challenging [52]. To overcome these challenges, a directed graph-based approach based on observability and fault resolution is proposed to optimize sensor locations for efficient fault identification [130].This technique was extended to optimize sensor locations for anomaly detection and isolation in process systems, devices, and instrument channels [54].Another approach uses Bayesian networks for sensitivity analysis of available instrumentation and control components [131]. A technique employs principal component analysis for sensor fault detection and isolation in NPPs [132]. Information on the axial and radial flux distribution in the core of the reactor is essential to alert the operator regarding abnormal or unexpected occurrences in the core. An approach determined optimal sensor locations to inform instrumentation of the in-core systems by representing the nuclear reactor as a linear stochastic distributed parameter system [133]. The next generation of NPPs is expected to include fiber-optic and wireless sensors due to extreme core temperatures; thus, determining optimal sensor networks and configurations of fiber-optic cables are essential research areas [134].

In NPPs, the implementation of optimally positioned sensors within distinct units such as steam generators, reactor fuel capsules, and other downstream components is paramount for enhancing the efficacy and safety of operations. This integrated approach not only facilitates robust monitoring and reactor control but also minimizes the need for human intervention, thereby elevating both safety and operational efficiency [135]. Optimal sensor deployment across critical components enables the collection of vital real-time data that mirrors the dynamic processes occurring within the physical assets of the plant. This data is crucial as it feeds into the digital space, where sophisticated reduced order models recreate the operational dynamics of the plant. By providing a precise and continuously updated representation, the digital twin allows for the accurate reconstruction of operational fields and aids in differentiating between authentic operational signals and noise interference. For instance, sensors placed in the reactor core can monitor critical metrics like temperature changes, while sensors in steam generators assess fluid dynamics and heat transfer efficiencies, ensuring that the virtual model accurately reflects the cooling performance.

This work leverages computational models developed for nuclear subsystems to apply a constrained data-driven sensor optimization approach [136] to establish instrumentation during the design stage of NPPs. Our target application is the reconstruction of fields of interest from optimized sensor measurements of temperature, pressure, velocity, and heat flux during the service phase. The optimized sensors under constraints are demonstrated to provide highly accurate reconstructions, and uncertainty estimates under noisy measurements for high-dimensional fuel irradiation, various boiling regimes, and flow distributions in a steam generator. Our algorithm provides physics-revealing, interpretable models for flow field reconstruction, which can be used for the licensing, safety analysis and diagnosis of NPPs.

This following section details the models and simulations used for reactor vessels, fuel capsules, and steam generators, outlines the constraints of sensor instrumentation in each. The developed constrained sensor placement approach is applied to optimally distribute sparse sensors within these systems. Finally, uncertainty estimates are described under noisy sensor measurements to provide evaluation metrics for a certain sensor configuration.

4.1 Modeling and Simulation for Reactor Components

In this section we describe the physics models and simulations of reactor components that take into account boundary conditions, operation parameters, and experimentation regimes. These models are used as data for sensor placement in the design stage to leverage low-dimensional structure in the data for constrained, sparse sensing.

4.1.1 3D Modeling of Fuel Capsules

This case study will optimize TC locations for accurately predicting the TRISO fuel temperature for an irradiation experiment being placed in the northeast flux trap of the advanced test reactor (ATR) at INL. The experiment comprises several capsules, each of which is equipped with its own temperature control and fission gas monitoring systems. The temperature control is achieved by real-time temperature measurement using TCs and through the flow of different composition gas blends (a helium-neon mixture) for temperature adjustment.

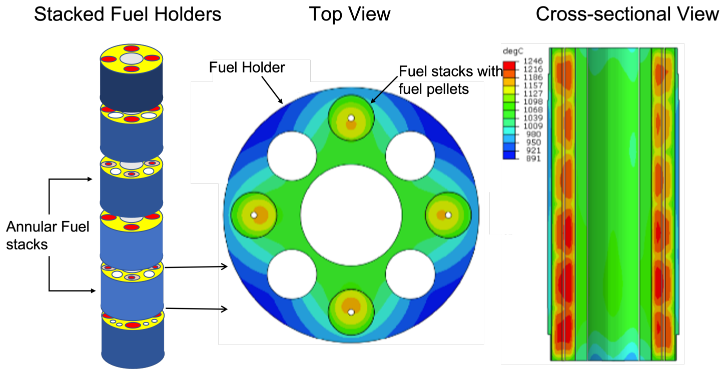

Figure 4.2: Irradiation of TRISO fuel experiment in the advanced test reactor.

To ensure independent temperature control for each capsule, a stainless-steel wall pressure boundary and bottom and top caps are used for physical separation. Two types of fuel pellets will be irradiated: solid and annular. The purpose of irradiating annular fuel is to get accurate temperature measurements as the solid fuel does not allow TC penetration. Fuel temperature must be derived from the surrounding graphite holder temperature measurement. If the TC positions in the holder are optimal, fuel temperature can be traced accurately. The annular fuel TCs then serve another function: comparison of the derived and measured fuel temperatures. Figure 4.2 shows the cross-section view of one of the annular fuel capsules. In the capsule, TCs will be inserted into the graphite holder or the center hole of the annular fuel.

The capsule wall has a uniform inner diameter larger than the holder thus leaving a convective heat gap between the holder and the capsule. The desired temperature of the fuel is achieved by adjusting the gap size. The convection influence on the fuel temperature evaluation has been investigated by a STAR-CCM+ simulation using a 2.54 mm (a bounding size that will not be exceeded) gap. As the temperature difference with or without convection is less than 1 K, without convective heat transfer, the experiment can be modeled by Abaqus, a finite element code. The fuel generates both neutron and gamma heating while the non-fuel parts generate only gamma heating. Analysis of these heating regimes are obtained by the reactor physics analysis. Forced convection cooling outside the capsule wall

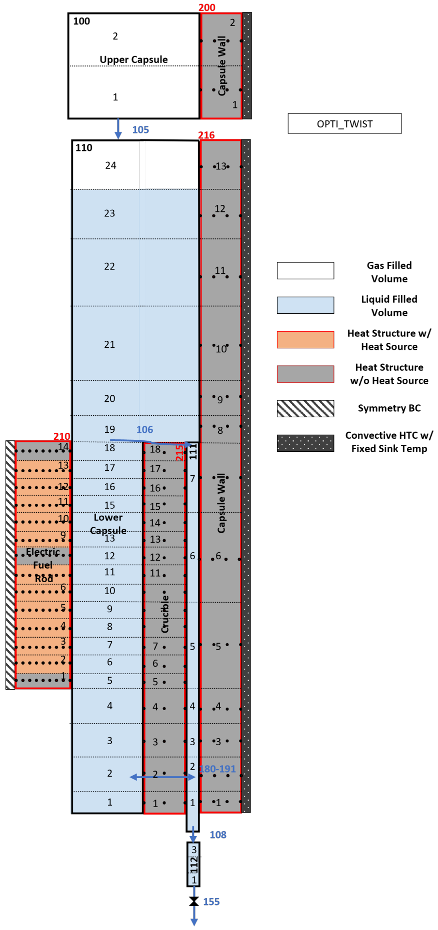

Figure 4.3: OPTI-TWIST RELAP nodalization for simulating thermal-hydraulic behaviour of test fuel rods.

is simulated through a convective (Neumann) boundary condition. The gas gap is affected by the holder and capsule thermal expansions and irradiation induced graphite dimensional change. The in-situ influence has been considered in the GAPCON subroutine of Abaqus. After obtaining the temperature field, this data is utilized to determine the optimal radial and axial coordinates for thermocouples, ensuring they are constrained within the holder to accurately reconstruct the fuel temperature.

4.1.2 Lumped-Parameter Model of OPTI-TWIST

The OPTI-TWIST (Out-of-Pile Testing and Instrumentation Transient Water Irradiation System) is an electrically heated system to prototype TWIST, a nuclear fuel test vehicle. OPTI-TWIST tests instrumentation that is used to qualify nuclear fuel under accident scenarios, like a loss of coolant accident (LOCA) or a reactivity insertion accident. Monitoring temperature through optimally placed TCs in OPTI-TWIST eliminates complications of irradiation effects while preserving extreme thermal-hydraulic conditions. A lumped-parameter code, the Reactor Excursion and Leak Analysis Program (RELAP5-3D) [137], was used to model the system's thermal-hydraulic parameters under transient operation.

Figure 4.3 shows the RELAP nodalization of OPTI-TWIST. The system (not drawn to scale) is made up of two cylindrical pressure vessels connected by a quick-acting blowdown valve to simulate a break in a LOCA. The model assumes axis-symmetric conditions. Hydrodynamic volumes capture the fluid parameters at various elevations, while heat structures represent the solid internal and external walls. The electric surrogate fuel rod is seen to be vertically discretized but also radially discretized to represent the larger thermal gradients present. Spatial constraints are imposed on sensor placement in the heater region due to restrictions on the number of TC's that can be placed within the compact heater. Data that captures the evolution of thermal gradients through the transient can be used to determine constrained TC locations.

4.1.3 1D Python Model of Steam Generator

Investigation of the thermal-hydraulic performance of the steam generator is essential for reactor normal operations and reactor safety during transients. Modeling and analyzing the single-phase liquid water flow (natural circulation) on the primary side and single-phase liquid water flow, subcooled boiling, saturated nucleate boiling, dispersed flow film boiling, and single-phase vapor/steam flow on the secondary side and the transition between these flow regimes is essential in predicting the SG performance. A Python code which uses 1D

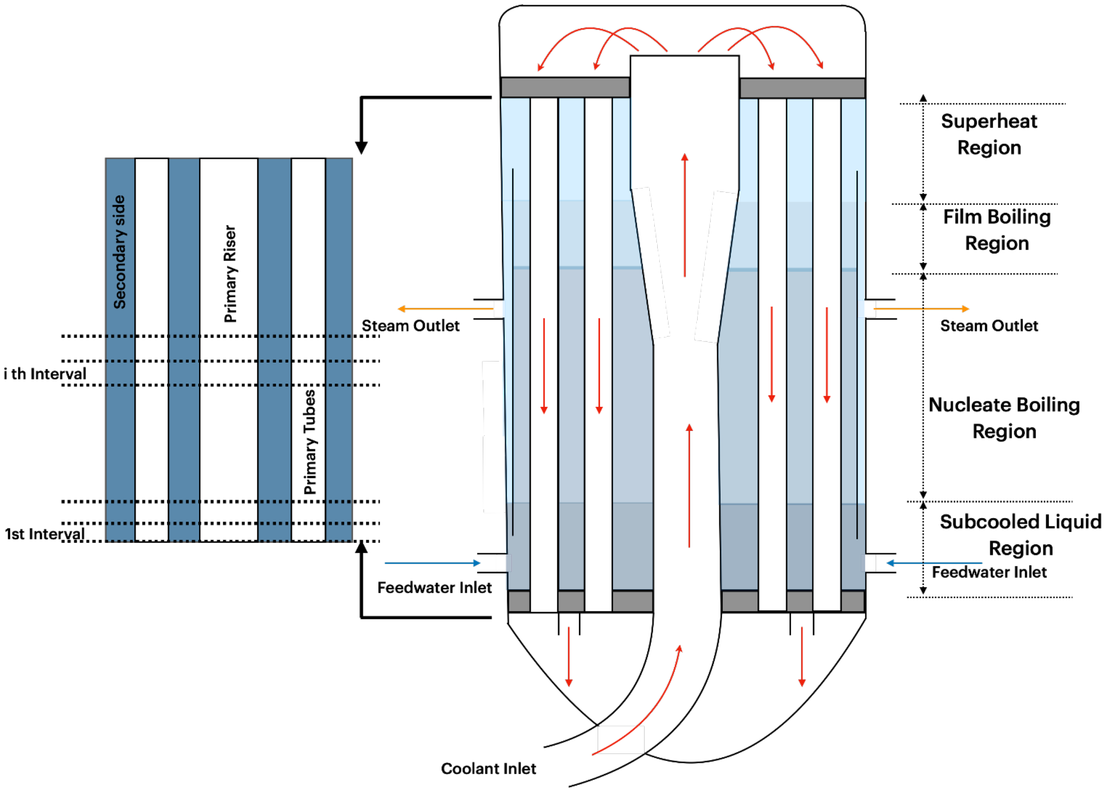

Figure 4.4: 1D Model of a steam generator which empirically simulates boiling phenomena occurring in the SG at different heights.

grids to discretize the long SG tubes into thousands of intervals and models phase transition regimes along the SG height, is developed for the thermal-hydraulic analysis of a vertical shell once through steam generator (OTSG) for a PWR.

The code starts the calculation from the bottom of the SG (first computational node), with an initial guess of the primary-side outlet temperature. Through these known fluid properties the boundary conditions for the second interval and the SG's overall heat transfer coefficient can be calculated from the effectiveness-NTU method. After looping through all computational nodes/intervals, the primary-side inlet temperature can be obtained and convergence criterion depends on difference between the computed value and the input parameter Monitoring phase transition within the steam generator tubes through optimal locations of

TC's, pressure taps and heat flux sensors along the height of the SG while considering spatial constraints is enabled through this 1D code.

4.1.4 3D CFD Model of Steam Generator

The previous 1D models nodalize and oversimplify fluid flow in the SG to 1D flow paths and sensor locations can only be determined along the height. Computational fluid dynamics (CFD) models in 3D are superior to their 1D counterparts in capturing the spatial distribution of velocity, pressure, and other fluid properties throughout the entire domain. This results in a more precise and detailed sensor optimization that captures flow phenomena such as turbulence, boundary layer effects, and fluid interactions with solid boundaries. Monitoring the flow distribution in the upper shell/plenum of the SG plays a critical role in predicting and preventing potential accidents that could jeopardize the structural integrity of the nuclear reactor. While multiple sensors can be mounted in the region of interest, they can impact the flow distribution and lead to high costs. Temperature distribution within the primary riser and secondary tubes is another field of interest captured through thermocouples. For temperature measurements, one of the SG tubes can be replaced with an instrumented tube. Ideally, multiple temperature measurements can be performed along the SG tube. However, the space available for the probes is constrained by the tube size and only a few sensors can be placed along it. Minimizing the number of sensors and strategically

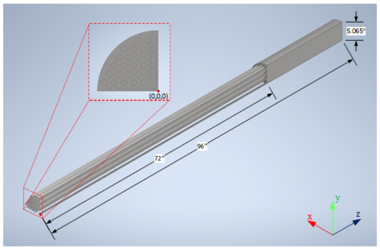

	Riser	**Upper Shell**	**SG Tubes**
Quantity	1	1	32
Inner Diameter (m)	0.021	0.257	0.013
Outer Diameter (m)	0.033	-	0.016
Length (m)	1.828	0.610	1.828

Figure 4.5: 3D CAD of the primary side which models 1/4th of the steam generator.

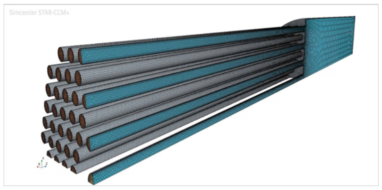

Boundary Conditions		
Inlet	Mass flow rate	0.1 to 3 kg/s
Outlet	Pressure outlet	Constant
Raiser	Wall: No Slip	Heat flux
Tubes	Wall: No Slip	Heat flux
Upper plenum	Wall: No Slip	Adiabatic
Mesh		
Mesh type	Polyhedral	Base size: 1 in.
Prism Layer	No. prism layers	3
	Prism layer thickness	25%

Figure 4.6: Discretization of SG geometry using a polyhedral mesh and boundary conditions generated in Star-CCM+.

placing them to capture the data required to provide insights into the flow distribution and thermal gradients is necessary.

Due to the large size of the SG, the geometry was simplified by excluding the shell's walls, baffles, lower head, etc. Instead, only the fluid volume of the upper shell, 1.828 meters (72 inches) of the riser's length, and partial tube length (1.828 meters) are modeled. The geometry's fluid domain is further reduced by modeling only a quarter of the steam generator, as illustrated in Figure 4.5 to reduce the computational cost of the CFD models. Figure 4.5 summarizes the dimensions used to generate the CAD model.

The geometry is discretized using a polyhedral mesh as illustrated in Figure 4.6. The inlet has a *Mass Flow Rate* boundary condition, while the tubes have a *Pressure Outlet* boundary condition. For purposes of this analysis, an adiabatic boundary condition is imposed on the outer walls of the upper shell. However, a *Convection* boundary condition is assigned to the riser and tubes. A summary of the assumed boundary conditions is presented in Figure 4.6

along with the mesh settings.

4.2 *Constrained Sensing Results*

This section illustrates the optimization of sensors for reconstructing key fields within the reactor and steam generator subsystems of the NPP. We account for various constraints arising from working conditions, manufacturing considerations, and spatial limitations during optimization. Our focus lies on reconstructing temperature, pressure, velocity, and heat flux within a steam generator, a TRISO fuel irradiation experiment, and an electrically heated fuel rod prototype capsule (OPTI-TWIST), using thermocouples, pressure taps, velocity probes, and heat flux sensors as described in section 4.1. We achieve minimal error in reconstructing the target response compared to randomly selected sensor locations and conduct uncertainty analysis on noisy measurements.

4.2.1 1D Steam Generator Model

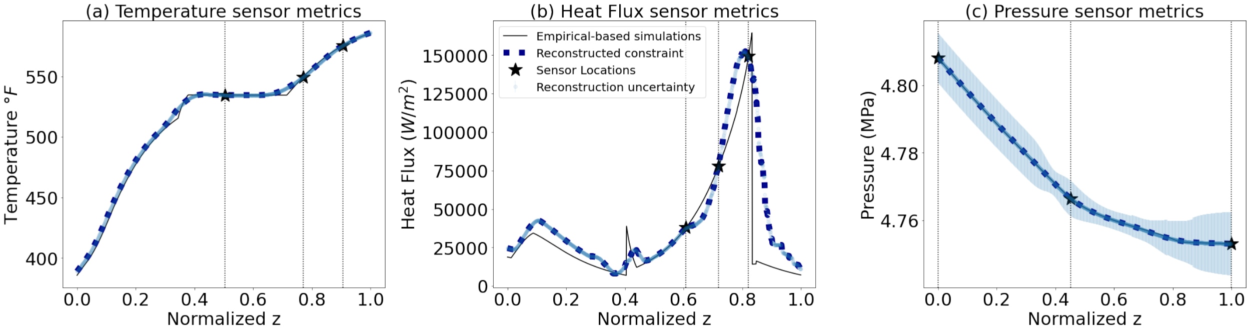

Figure 4.7: The secondary side temperature, flux, and pressure can be accurately reconstructed with minimal reconstruction uncertainty using only 3 QR constrained sensors. The sampling rate is ($p/n = 0.27\%$).

The 1D Steam Generator (SG) model, described in (subsection 4.1.3), offers a computationally efficient alternative to more complex Computational Fluid Dynamics (CFD) solvers.

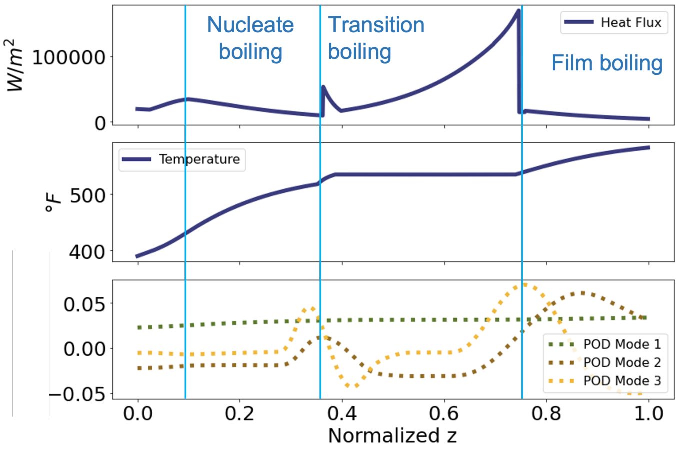

Figure 4.8: The leading three POD modes of secondary side temperature accurately approximate temperature fields with 99% of the energy content. The first mode captures the overall temperature profile, and the second and third modes capture heat flux variations along the normalized z-coordinates in the steam generator.

This model is particularly useful for estimating key parameters such as temperature, heat flux, and pressure within the steam generator. The model helps to estimate secondary side temperature, especially during the phase transition of water to steam. Temperature measurements are typically obtained using K and N type thermocouples (TCs) [138] which provide point-wise temperature readings. On the secondary side, the steam generator tubes are supported by 42 baffles evenly distributed along their length. These baffles maintain tube positioning during assembly and prevent vibration from flow-induced eddies during operation. Sensor placement is constrained by the need to avoid these baffles. The sensor placement algorithm is trained on 442 steady-state samples of secondary side temperature to determine optimal sensor locations while accounting for baffle constraints. Using p = 3 sensors, the field of interest is reconstructed for one test sample achieving a maximum reconstruction error (ϵ) of 0.9% compared to the ground truth (Figure 4.7). In the presence of noisy sensor measurements, state reconstruction uncertainty is low along the height of the SG with a maximum of 0.01 °F (Figure 4.7). Below $z = 0.4$ the temperature of water rises and remains constant between $z = 0.4, z = 0.8$ due to phase change from water to steam. Across the entire test set (162 samples), the maximum reconstruction error is 0.9% for QR selected sensors compared to ($\epsilon = 6.4$ %) for randomly placed sensors.

The relationship between the secondary side temperature and heat flux ($\dot{\mathbf{Q}}$) in the steam generator tubes was further analyzed. Optimized temperature sensors capture energy fluctuations in the POD modes. The leading POD mode represents the overall temperature profile, and the second and third modes capture the heat flux that causes the temperature variation (Figure 4.8). Heat flux, dependent on temperature gradients, can be estimated from TC-based temperature reconstructions outside the phase change region $z \in [0.4, 0.8]$. During phase change, temperature gradients vanish, and the heat flux is determined by the latent heat coefficient and the mass of the substance undergoing phase change. Heat flux for the different boiling regions is calculated separately, resulting in abrupt changes between boiling regimes. Further analysis of time-dependent data can allow for the inference of heat flux from temperature measurements.

Currently, the algorithm is trained on 442 steady-state samples of heat flux in the tubes and shell for locating baffle constrained optimal sensors. Heat flux can be measured using small square sensors attached to the steam generator's outer/inner wall [138]. The highest reconstruction error over all samples, compared to the ground truth is $\epsilon = 20.6\%$ for QR selected sensors (Figure 4.7). Higher error is due to modeling discontinuities in the training data for heat flux across different boiling regimes. Experimentally, heat flux decreases gradually after the phase change, as shown by sensor-based reconstructions, in contrast with the abrupt decrease caused by modeling discontinuities. For randomly placed sensors, the maximum error rises to $\epsilon = 48.9\%$. Under noisy sensor measurements, state reconstruction uncertainty is low for QR optimized sensors along the height of the SG with a maximum of 0.0099 W/m^2 (Figure 4.7).

Another important field of interest is secondary side pressure, measured locally with pressure taps on the steam generator shell [138]. Due to the low pressure variation ($\approx$ 0.04 MPa), QR selected sensors reconstruct the field with very high accuracy, achieving a maximum reconstruction error of $\epsilon = 0.002\%$ across all test samples (Figure 4.7). In contrast, randomly placed sensors fail to capture these small variations in pressure resulting in a maximum error of $\epsilon = 1\%$ (Figure 4.7). The maximum noise-induced uncertainty in pressure reconstruction is also low (0.009 MPa). Additionally, there is a linear relationship between secondary and primary side pressures, allowing regression techniques to infer one field from measurements of the other.

In conclusion, 3D CFD modeling of phase change phenomena is computationally expensive for complex systems such as steam generators. Using 1D nodalization provides an efficient alternative, offering real-time updates of multiple fields of interest. Optimized sensor locations derived from 1D modeling data can help uncover underlying physics of boiling regimes to estimate preliminary errors and uncertainties, aiding in the development of control regimes through digital twinning. Despite the advantages of 1D models, it's crucial to instrument specific tubes and place sensors in a 3D coordinate system. For licensing and safe operations, measuring flow distribution within the shell and tubes is essential. The next section explores a 3D model of the steam generator for optimizing temperature and velocity sensors.

3D Steam Generator Model

This section applies the sensor placement methodology to a 3D CFD model of the steam generator described in (subsection 4.1.4). The mass flow rate ($\dot{m}$) kg/s of the primary coolant varies between $\dot{m} \in [0.1, 3]$ with $\delta\dot{m} = 0.1$. As the mass flow rate increases, the temperature variation ($\Delta T = T_{maximum} - T_{minimum}$) decreases, given a constant heat flux boundary condition. Temperature measurements can be taken using K or N type point TCs or the Sporian ThermaFlow sensors described in [138]. These sensors can be placed within the shell, riser, and tubes of the SG. It is easier to place sensors in the shell as compared to the tubes and riser, as the flow within these narrow cylindrical bodies can be obstructed due to sensors. Instrumenting one tube or just the riser reduces sensor costs and allows normal flow development in the remaining tubes. The objective of optimizing sensor locations is to

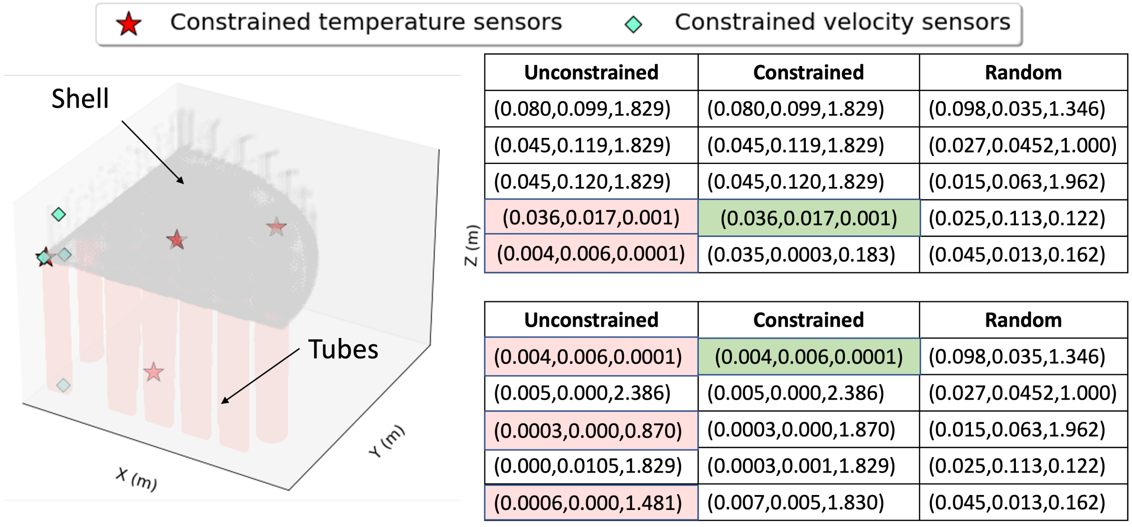

Unconstrained	Constrained	Random
(0.080,0.099,1.829)	(0.080,0.099,1.829)	(0.098,0.035,1.346)
(0.045,0.119,1.829)	(0.045,0.119,1.829)	(0.027,0.0452,1.000)
(0.045,0.120,1.829)	(0.045,0.120,1.829)	(0.015,0.063,1.962)
(0.036,0.017,0.001)	(0.036,0.017,0.001)	(0.025,0.113,0.122)
(0.004,0.006,0.0001)	(0.035,0.0003,0.183)	(0.045,0.013,0.162)

Unconstrained	Constrained	Random
(0.004,0.006,0.0001)	(0.004,0.006,0.0001)	(0.098,0.035,1.346)
(0.005,0.000,2.386)	(0.005,0.000,2.386)	(0.027,0.0452,1.000)
(0.0003,0.000,0.870)	(0.0003,0.000,1.870)	(0.015,0.063,1.962)
(0.000,0.0105,1.829)	(0.0003,0.001,1.829)	(0.025,0.113,0.122)
(0.0006,0.000,1.481)	(0.007,0.005,1.830)	(0.045,0.013,0.162)

Figure 4.9: Temperature and velocity sensor locations for unconstrained, constrained and randomly placed sensors. Unconstrained QR places 2 temperature and 3 velocity sensors in the tubes ($Z < 1.828$ m) highlighted by the red boxes. Physically, just one of the tubes is instrumented. Constrained QR restricts just one temperature and one velocity sensor within tubes (green boxes).

limit instrumentation to lie either within the shell or to just one of the tubes.

Optimized, unconstrained QR pivoting locates two sensors in the SG tubes (z ¡ 1.828 m in Figure 4.9) and achieves a reconstruction error of $\epsilon = 0.329\%$. In contrast, constrained optimization places only one sensor in the tube while maintaining a comparable reconstruction error of $\epsilon = 0.331\%$ (Figure 4.10b,Figure 4.10a). Optimal sensor reconstructions outperform randomly placed sensor reconstructions which have a maximum error of $\epsilon = 1.647\%$ (Figure 4.10c). In these figures we reconstruct temperature profiles developed by the nominal mass flow rate $\dot{m} = 1.2 m/s$. Additionally, reconstruction errors decrease with increasing mass flow rate (Figure 4.11) due to reduced temperature variation at higher mass flow rates (brown dots in Figure 4.11). Ensembles of randomly located sensors (error bars in Figure 4.11) fail to accurately capture the temperature field across the SG. A similar trend

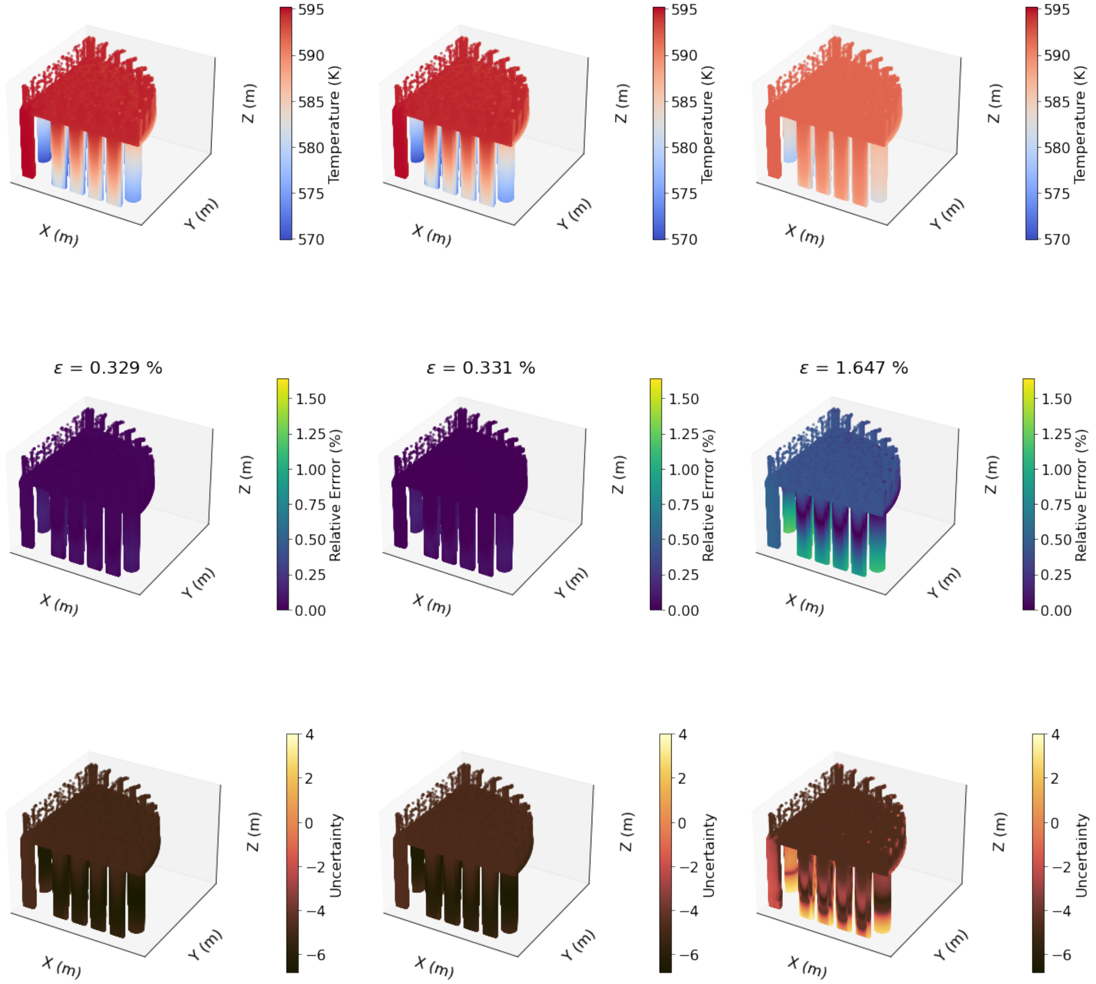

(a) Unconstrained (b) Constrained (c) Random

Figure 4.10: QR optimized sensors reconstruct the temperature field with high accuracy (a). Constraining a single sensor to lie within one of the steam generator tubes results in only a minimal increase in error and noise-induced uncertainty for temperature reconstruction (b), compared to the high error of randomly placed sensor reconstructions (c). (Top) Sensor-based reconstructions. (Middle) Relative reconstruction error. (Bottom) Noise-induced uncertainty heatmaps (log scale).

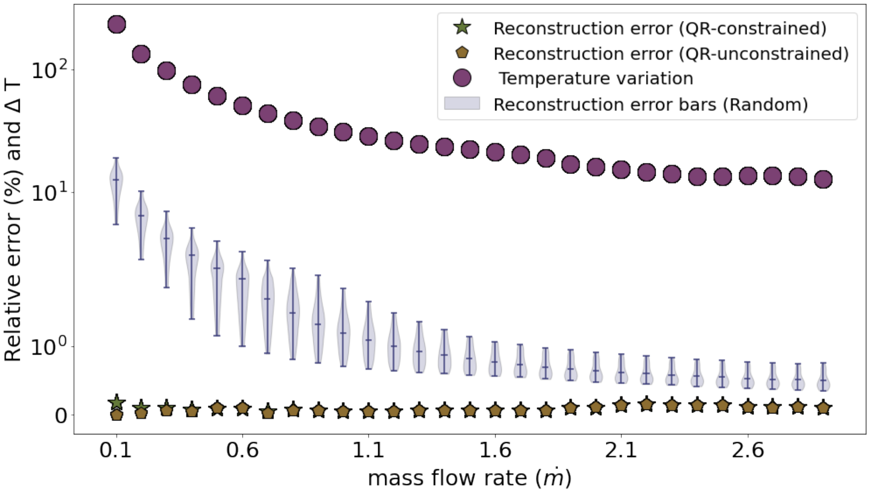

Figure 4.11: QR optimized sensors capture temperature variance within the SG, leading to higher reconstruction accuracy across all mass flow rates compared to random sensor placement. Optimized sensors achieve low reconstruction errors ($\epsilon \approx 0.34\%$), and random placements result in larger errors ($\epsilon \approx 2\%$).Plot is shown on a symbolic log scale to highlight differences in reconstruction errors.

is observed in noise-induced uncertainties, with QR-optimized sensors showing a maximum uncertainty of 0.010 °K, while random sensor placements result in uncertainties up to 20 % (seen in row 3 of Figure 4.10a,Figure 4.10b,Figure 4.10c).

Next, the algorithm was applied to velocity data of the 3D SG as the coolant flows through the riser, makes a 180° turn through the shell, and returns to the tubes. Measuring the distribution of coolant entering the various tubes is crucial for manufacturing and can be achieved using Sporian ThermaFlow sensors described in [138]. Similar to TC placement, instrumenting just one tube is key to allowing normal flow development in the others. Optimized unconstrained QR places three sensors among the tubes (z ¡ 1.828 m in Figure 4.9), achieving a maximum absolute reconstruction error of 0.005 m/s and a maximum noise-induced uncertainty of 0.010 m/s (Figure 4.12a). With constraints, only one sensor is placed in the tubes, with the rest in the shell, resulting in a maximum absolute reconstruction error

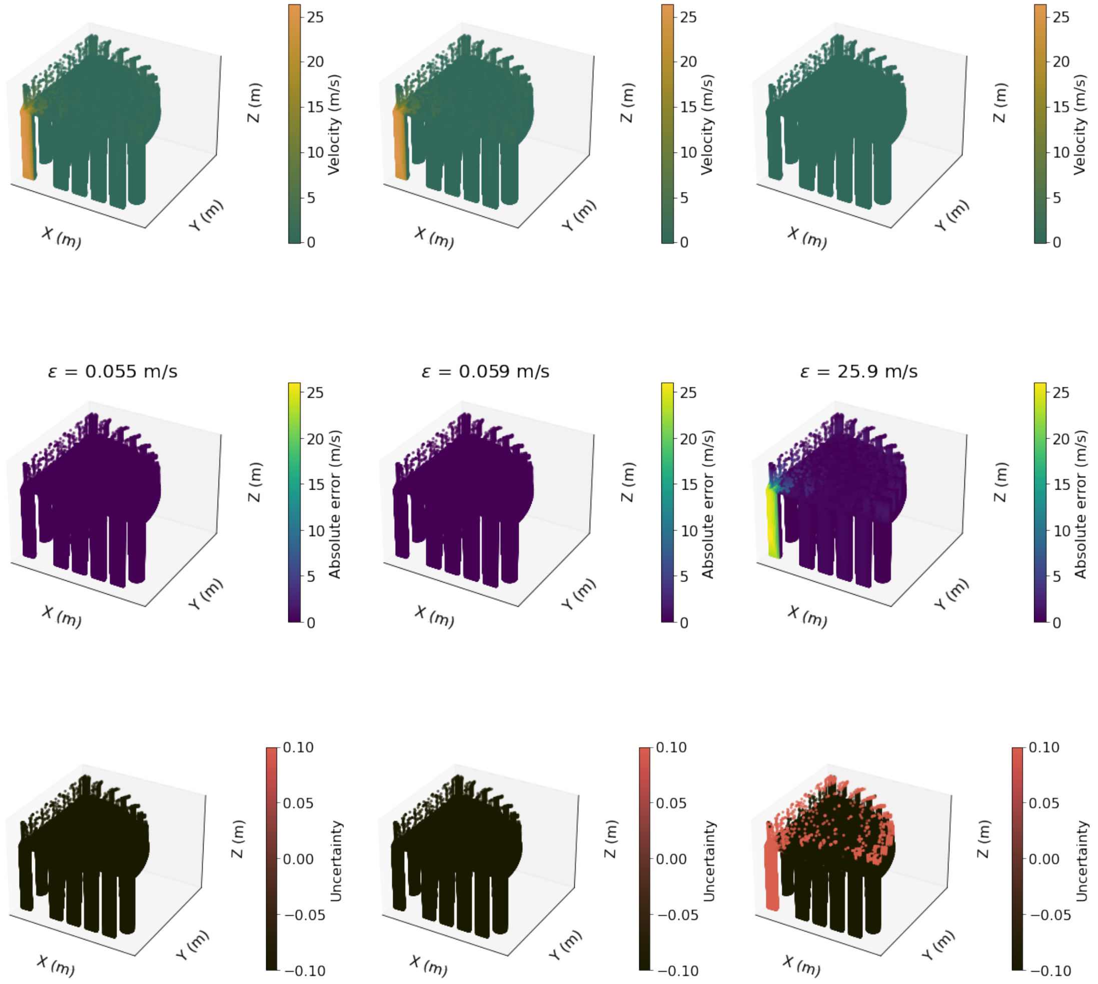

(a) Unconstrained (b) Constrained (c) Random

Figure 4.12: QR optimized sensors (both unconstrained and constrained) detect the underlying dynamics of coolant flow within the SG and reconstruct the velocity field with high accuracy and low noise-induced uncertainties (a, b). By contrast, random sensors are unable to reconstruct the field resulting in high errors and uncertainty (c). (Top) Sensor based reconstructions. (Middle) Relative reconstruction error. (Bottom) Noise-induced uncertainty heatmaps (log scale).

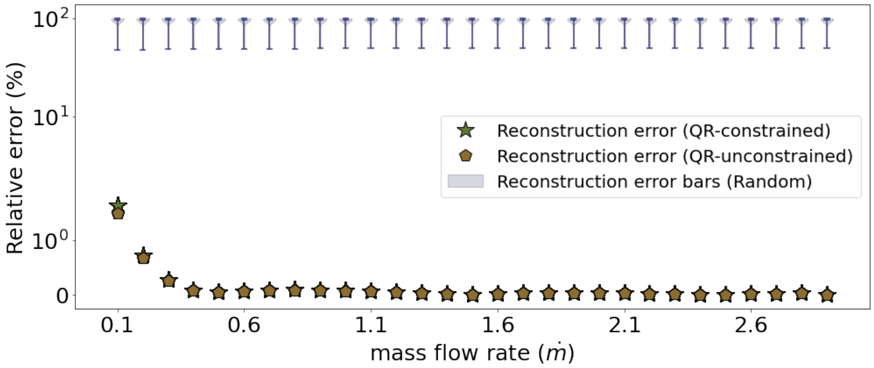

Figure 4.13: QR optimized sensors capture flow of the coolant through the riser as it make a 180 °turn through the shell, leading to higher reconstruction accuracy across all mass flow rates compared to random sensor placement. Optimized sensors achieve low reconstruction errors ($\epsilon \approx 0.05 m/s$), while random placements result in much larger errors ($\epsilon \approx 25 m/s$). Plot is shown on a symbolic log scale to highlight differences in reconstruction errors.

of 0.005 m/s and a comparable maximum uncertainty of 0.8 m/s (Figure 4.12b). Randomly placed sensors fail to reconstruct velocity accurately, and have a maximum absolute error of 25 m/s while uncertainty rises to 10^3 m/s(Figure 4.12c). Across all mass flow rates, QR-optimized sensors maintain a low reconstruction error of 0.05 m/s, whereas random sensors exhibit high errors as indicated by the blue error plots (25 m/s) (Figure 4.13).

Unconstrained optimization favors locating sensors within the tube and riser, due to the richer dynamics that exist there. Imposing sensor constraints within QR results in a near-optimal placement in the shell and one of the tubes, as well as negligible loss of reconstruction performance. The 3D CFD model of the steam generator, comprising 5,616,200 mesh points, provides the velocity and temperature data. QR-optimized sensors can reconstruct these high-dimensional fields using just five sensors ($p = 5$) with minimal errors which enables real-time monitoring of the SG. On the other hand, random placement of sensors within the SG introduce large errors and uncertainties. Therefore, placing sensors without optimizing them in regard to the underlying flow especially in the presence of noisy sensor measurements can introduce large errors in the corresponding digital twins. Informed planning of instrumentation for the steam generator can play a key role in real time digital twinning, monitoring steam quality, flow distributions and nominal working conditions while also preventing accidents and detecting anomalies.

4.2.2 Irradiation of TRISO Fuel

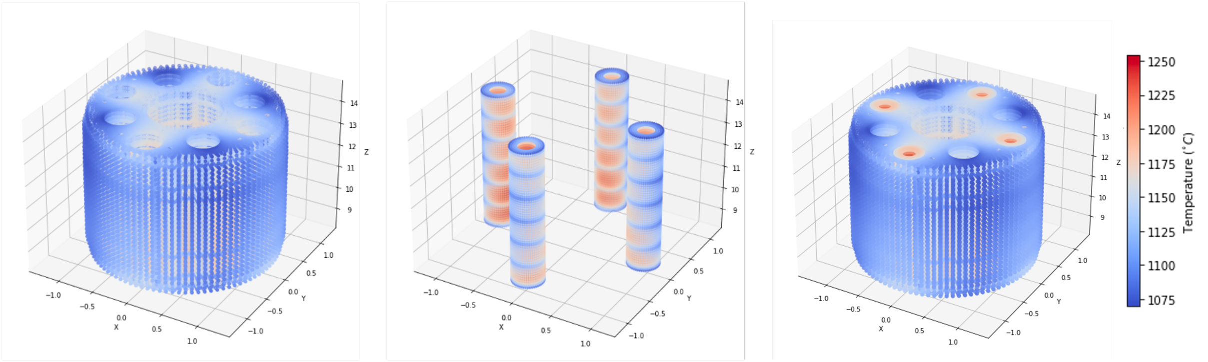

(a) Graphite Holder (b) Fuel (c) Holder with Fuel

Figure 4.14: Temperature profile of the fuel capsule at the end-of-cycle stage. The temperature in the fuel reaches 1250 °C (b),compared to around 1000 °C in the graphite holder (a). Accurate reconstruction of the temperature profile within the fuel through TC's is crucial due to the richer dynamics inside the TRISO fuel (c).

To support the next generation of reactors, testing, validation and performance assessment of new fuels under reactor working conditions are essential. Monitoring TRISO fuel temperature (Figure 4.14a) during irradiation experiments is challenging due to the extreme temperatures (1200 $^{\circ}C$ - 1300 ° C) inside the fuel. As detailed in [138], HTIR-TCs can withstand temperatures exceeding 1600 $^{\circ}C$.[139]. However, nuclear TC's eventually drift due to long-term exposure to neutron bombardment and high temperatures [140]. Placing sensors in the surrounding graphite holder (Figure 4.14b) allows accurate temperature reconstruction within the fuel stacks, reducing TC exposure to high temperatures, minimizing drift and extending sensor lifespan.

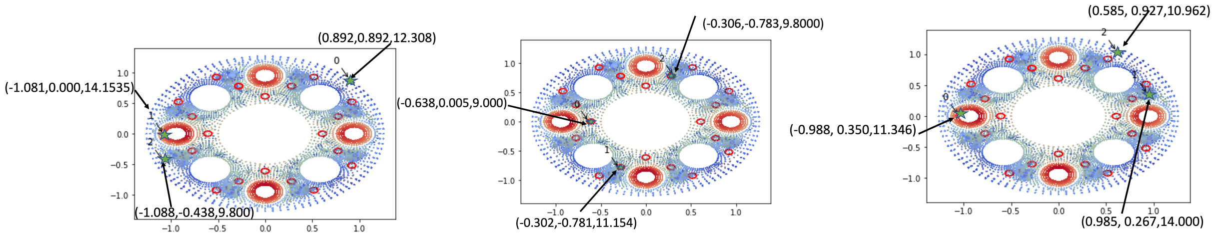

(a) Unconstrained placement (b) Constrained placement (c) Random sensors

Figure 4.15: The unconstrained sensor locations (a) are infeasible since one of the thermocouples is placed in the fuel. The developed algorithm constrains the TCs to lie within potential structural holes (red circles) (b), selecting drill locations where the drill depth is given by the Z coordinate, and the random sensor layout is shown in (c).

In the graphite holder, TCs cannot be placed at all locations due to constraints on drilling holes to accommodate sensors and inert gas inlets and outlets. (Figure 4.15) illustrates available drilling locations for TCs (red circles). The developed sensor placement algorithm must select three to four holes from the given 19 possibilities, with each hole accommodating just one sensor, while also determining the depth of the TC within the drilled holes. Data is derived from a 3D FEM model described in (subsection 4.1.1) representing the beginning (BOC) and end (EOC) of fuel irradiation cycle. Neutron and gamma heating information is obtained through reactor physics analysis, which is computationally intensive and time-consuming and can provide just 10 samples. The algorithm is trained using eight randomly selected samples of EOC and BOC data and tested on the remaining two samples.

Optimized, unconstrained QR pivoting selects sensors strategically within the fuel and along the edges of the capsule to capture maximum temperature variance (Figure 4.15a). However, due to constraints on drill locations for TCs within the capsules, these uncon-

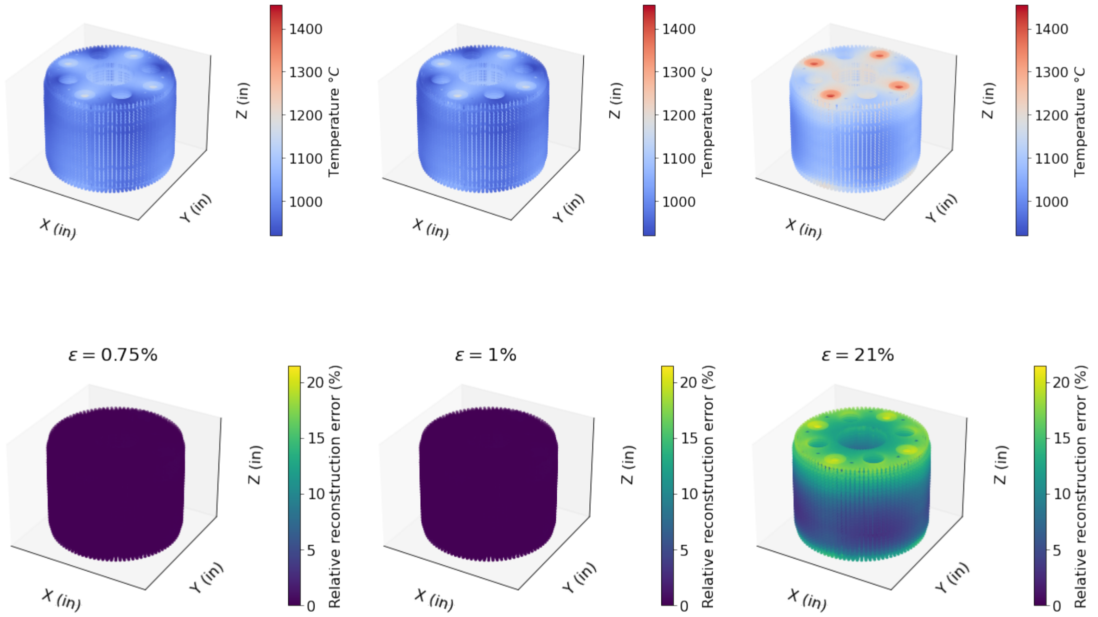

(a) QR unconstrained (b) QR constrained (c) Random

Figure 4.16: QR optimized sensors reconstruct temperature profile within the graphite holder (1^{st}, 2^{nd} row (a, b)) when compared to random sensor locations (**c**). (1^{st} row) Sensor based reconstructions. (2^{nd} row) Relative reconstruction error.

strained sensor placements are not feasible in a physical experiment. Thus, the developed algorithm constrains sensor optimization to points within the 19 possible drill locations (Figure 4.15b). Measurements at these constrained locations result in a maximum relative reconstruction error of 1% within the capsule, while the error is 0.39% within the fuel (Figure 4.16b,Figure 4.17b). Unconstrained reconstruction yields a maximum error of $\epsilon = 0.75\%$ in the capsule, and an error of 0.37% in the fuel (Figure 4.16a,Figure 4.17a). Random sensor placement (Figure 4.15c) refers to intuitive selection based on ease of maintenance and access, which leads to inaccurate reconstruction with higher errors $\epsilon = 25\%$ (Figure 4.16c,Figure 4.17c). To illustrate various random selections of sensors, 20 ensembles of random unconstrained sensor combinations were used to reconstruct temperature profile

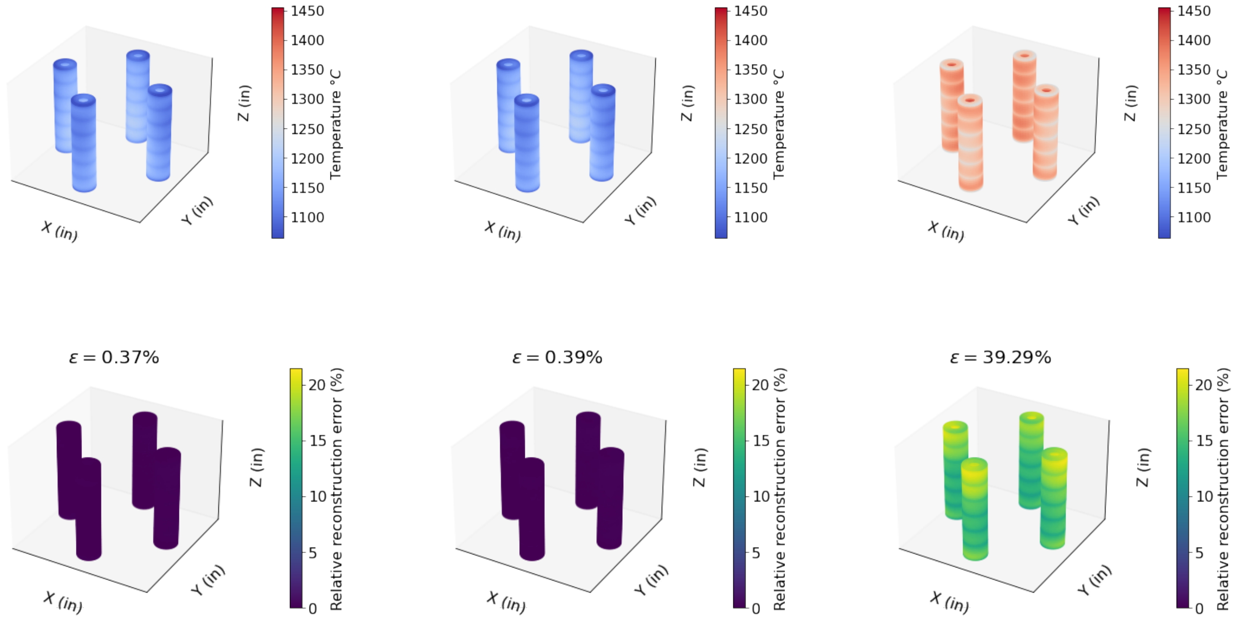

(a) QR unconstrained (b) QR constrained (c) Random

Figure 4.17: QR optimized sensors reconstruct temperature profile within the TRISO fuel (1^{st}, 2^{nd} row (a, b)) when compared to random sensor locations (c). (1^{st} row) Fuel reconstruction through sensors. (2^{nd} row) Fuel relative reconstruction error.

for all the samples. Comparison with QR-optimized sensors (1%) shows higher reconstruction errors for random ensembles (30%) (Figure 4.18).

Zero mean Gaussian noise with $\beta = 0.01$ is added to analyze uncertainty heatmaps for temperature reconstruction to illustrate noisy TC readings as in (Equation 3.17). The maximum uncertainty for constrained sensing is 0.0241 °C (Figure 4.19b) as compared to unconstrained sensor placement (Figure 4.19a) which has an uncertainty of 0.010 °C. Randomly placed sensors result in very high uncertainty for state reconstruction (9.8 °C) (Figure 4.19). In summary, the sensor placement framework accounts for design, manufacturing, and deployment constraints to optimize sensor placement. It provides error estimates and uncertainty for noisy sensor readings from modeling data, aiding in approximating errors in

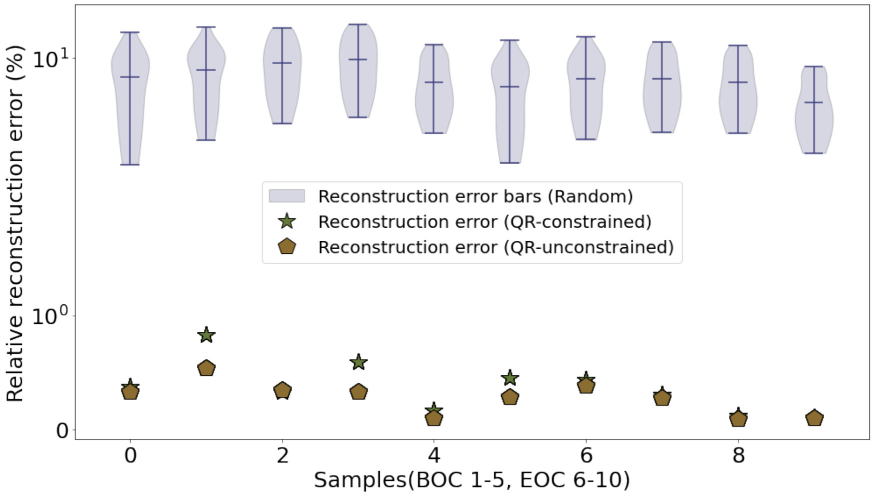

Figure 4.18: QR optimized sensors are the most accurate in capturing the neutron and gamma heating dynamics at both beginning-of-cycle and end-of-cycle stages. Optimized sensors reconstruct temperature fields with low errors ($\epsilon \approx 1\%$), whereas random placements result in significantly larger errors ($\epsilon \approx 30\%$).Plot is shown on a symbolic log scale to highlight differences in reconstruction errors.

physical experiments and establishing manufacturing parameters such as drill hole depths for TCs. Accurate reconstructions and uncertainty bounds (Equation 3.20) through sensors can help quantify TC drift due to long-term radiation exposure in TRISO fuel through digital twinning.

4.2.3 Electrically heated prototype capsule- OPTI-TWIST

In this section, thermocouple (TC) locations are optimized for reconstructing temperature within an electrically heated fuel rod (OPTI-TWIST), simulating the behavior of a nuclear fuel rod as described in (subsection 4.1.2). Analyzing the impact of power transients on reactor core coolant temperature, pressure, and velocity is crucial for real-time safety monitoring and control in a nuclear reactor. In this study, sensor placements were optimized to capture heat flow dynamics during power transients. It is important to detect when sensor

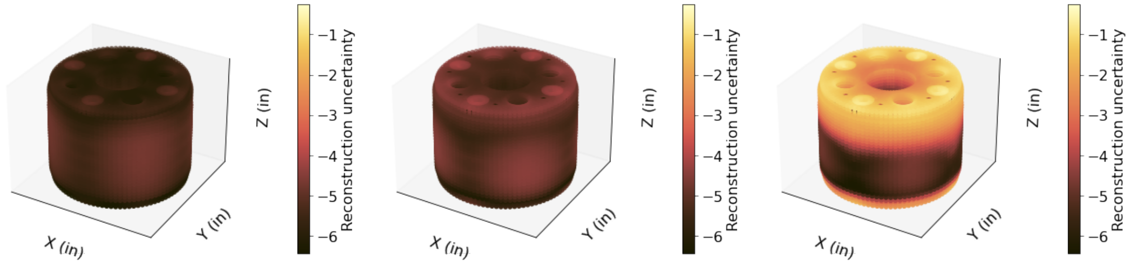

(a) Unconstrained (b) Constrained (c) Random

Figure 4.19: Optimized sensors result in lower estimation uncertainty in state reconstruction within the fuel when sensor measurements are corrupted by noise (a, b) compared to random placement (**c**). These estimation errors propagate through the digital twin and affect downstream control decisions. Plots are shown on a log scale to highlight regions of higher uncertainty.

readings diverge from predicted metrics in the presence of noise during transients. This early detection can signal the need for digital twin recalibration and prevent accidents caused by power surges at a nuclear facility. In this case the power surge is modeled as:

$$\begin{aligned} P(t) &= P_t, \text{ if } t \leq t_1, \\ P(t) &= P_n, \text{ if } t > t_1, \end{aligned} \tag{4.1}$$

where $P_t = 500W, P_n = 0W, t_1 = 15s$. The power rises to 500 W within the first 15 seconds and remains off for the next 85 seconds. Heat flow through the capsule during this transient is simulated by nodalization of the OPTI-TWIST geometry to capture temperature gradients in RELAP (described in subsection 4.1.2). K and N Type TC's are used for instrumentation of the rod [138], with their number restricted to $p = 3$. The unconstrained QR method places two sensors near the heater, as seen in (Figure 4.20a) capturing richer dynamics close to the heat source and resulting in a maximum relative reconstruction error of $\epsilon = 0.06$ % . However, spatial constraints limit TC placement to just one sensor in this region (Figure 4.20b) resulting in a comparable $\epsilon = 0.15$ %. POD modes, averaging over the time

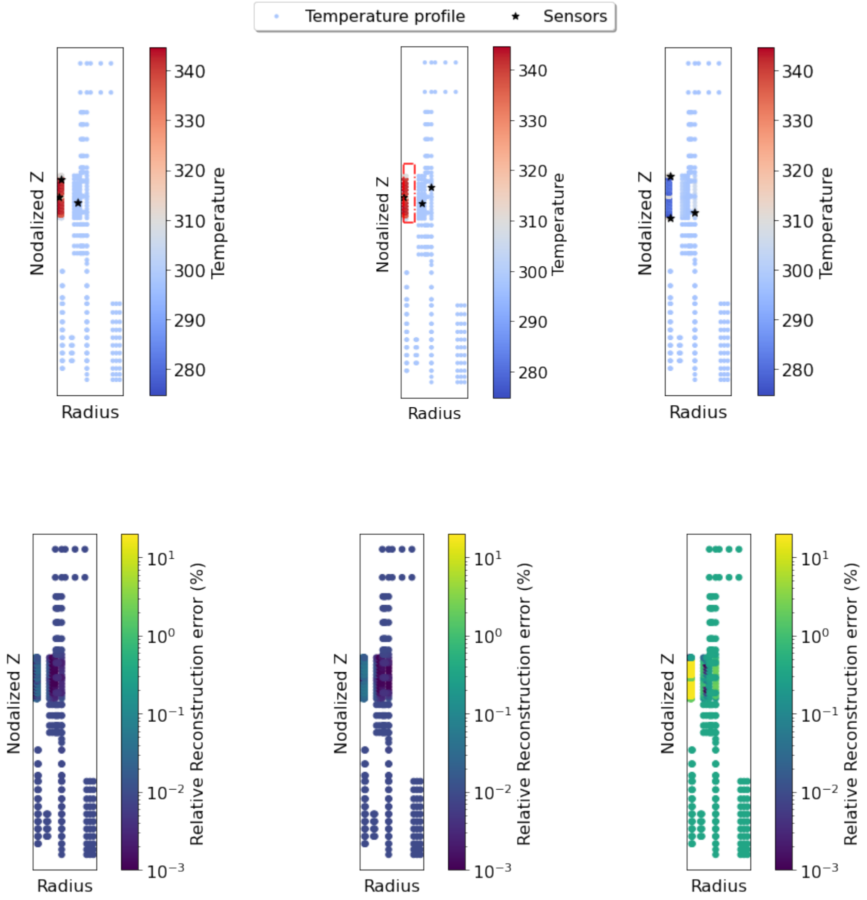

(a) Unconstrained (b) Constrained (c) Random

Figure 4.20: Richer dynamics close to the heat source result in selection of unconstrained sensors near the heater (a-top), achieving negligible reconstruction error $\epsilon = 0.06\%$ (a-bottom). However, these locations are unfeasible as the heater cannot accommodate multiple sensors. Constraining sensors to lie outside the heater region (b-top) produces a layout with comparable reconstruction errors $\epsilon = 1\%$ (b-bottom). Random sensor placement leads to inaccurate reconstructions (c-top) with high reconstruction errors $\epsilon \approx 10^{1}\%$ (c-bottom).

domain for time-dependent data, capture maximum variance in the temperature profile. When the heater power is at 500 W, the temperature variation is around 60 $^{\circ}C$ whereas it

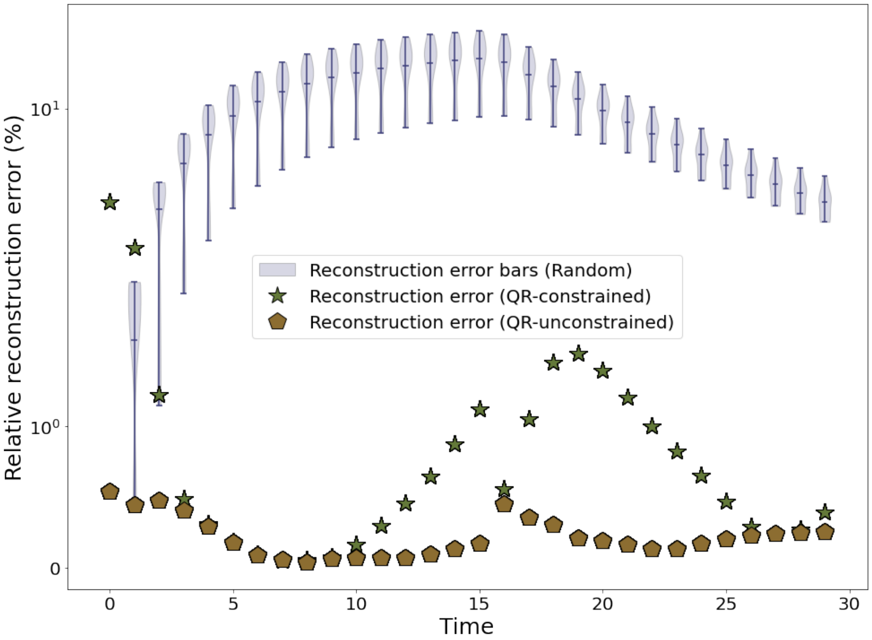

Figure 4.21: Constrained QR optimized sensors initially fail to capture temperature variation at t=0 due to the transient but achieve lower error as the transient progresses ($\epsilon \approx 0.5\%$). Once the transient ends at t=15, constrained QR reconstruction error briefly rises before capturing cooling down of the capsule. Reconstruction error for ensembles of randomly selected sesnors increases and then stays the same with time ($\epsilon \approx 75\%$) while unconstrained QR sensors placed in heater adjacent locations result in lowest error through the entire transient. Plot is shown on a symbolic log scale to highlight differences in reconstruction errors.

becomes negligible when the power is off. Randomly placed sensors, with two located near the heater, fail to capture this temperature variation, resulting in high errors ($\epsilon = 30\%$) reconstructing the OPTI-TWIST temperature profile (Figure 4.20c). Errors are calculated for the temperature profile at 8 seconds (mid-way through the transient). For the first two time-steps, the reconstruction error for an ensemble of 20 combinations of three randomly placed sensors (pink error bars) is comparable to QR placements (Figure 4.21). Subsequently,

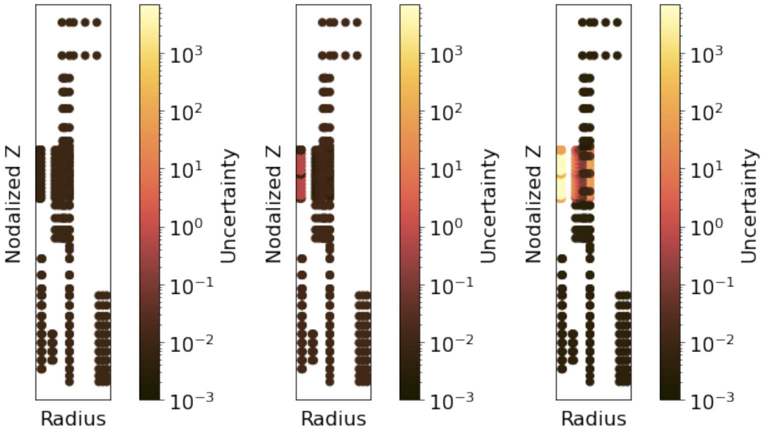

(a) Unconstrained (b) Constrained (c) Random

Figure 4.22: When sensors are constrained to lie outside the heater region (**b**), the uncertainty in the heater region increases slightly by 0.95 °K, and for randomly placed sensors, it can increase up to 1000 °K.

as the algorithm captures temperature variation, QR sensors result in significantly lower reconstruction errors ($\epsilon = 0.2$ %) as compared to randomly placed sensors ($\epsilon = 75$ %) over the transient domain. As the transient subsides, the error for both QR optimized and random sensors briefly increases as the capsule cools down and temperature differences diminish. While POD modes capture maximum temperature variance during the transient, further analysis using DMD, DMDc and time delayed embedding is needed to accurately model the transient's time-dependent nature..

The uncertainty in state reconstruction due to noisy measurements is calculated using (Equation 3.17). Adding Gaussian i.i.d noise $\boldsymbol{\eta} \sim \mathcal{N}(0, 0.01)$ results in higher uncertainty (0.825 °K) around the heater when sensors are constrained away from the heat source (Figure 4.22b) as compared to unconstrained heater adjacent sensors (0.009 °K)(Figure 4.22a). For three randomly selected sensors near the heater, the uncertainty in reconstruction is high (10^{3} °K) for regions adjacent to the heat source (Figure 4.22c). Optimizing sensor locations to capture underlying dynamics reduces reconstruction errors and uncertainty from TC readings in the presence of noise. This optimization enables the establishment of digital twins (DTs) for reliability and safety analysis of power transients and surges in nuclear fuel rods.

4.3 Conclusion

This work leverages computational models of NPP subsystems including steam generators, fuel capsules and fuel irradiation experiments to provide optimal sensor locations subject to inherent spatial limitations. The developed data-driven approach applied to preliminary 1D simulations of the steam generator establish sensor layouts that capture multiple fields of interest with high accuracy. They also provide interpretable models to study boiling regimes in steam generators. Further, TC locations identified by the algorithm for the 3D CFD model of the steam generator capture temperature variations as the mass flow rate of the primary coolant changes. Flow distribution within the shell and tube can be accurately reconstructed with just one instrumented tube and the rest of the sensors constrained to the shell. In TRISO fuel irradiation experiments, sensors constrained to lie in the graphite holder outside the fuel accurately reconstruct the temperature within the fuel with low noise-induced uncertainty. In the event of sudden increases in power during accident scenario testing in fuel rods, sensor layouts capture temperature variations across the transient while constraining sensors to lie outside the heater adjacent region. It is desirable to place the fewest number of sensors in locations that have extreme conditions (TRISO fuel) or where sensors would obstruct the development of nominal flow (SG tubes). We show that accurate reconstruction can be achieved with as few as 3 intrusive sensors. In conclusion, constrained sensor locations minimize reconstruction errors, provide statistical bounds for noise-induced uncertainties for high-dimensional nuclear applications that can be further used for safety analysis, licensing, accident scenario testing and reliability analysis of the NPP. Through CFD, FEM, and Python models, the effectiveness of adaptive sensor placement and accuracy of the reconstructed responses of interest has been demonstrated.

Chapter 5

SENSOR-BASED CLASSIFICATION AND RECONSTRUCTION: ANALYSIS OF POWER PERTURBATIONS FOR DIGITAL TWINS

Analyzing the effect of power perturbations and transients on reactor core coolant temperature, pressure, and velocity is essential for real-time safety monitoring and control of a nuclear reactor. Various types of fluctuations occur within the core of the reactor caused by mechanical vibrations, coolant boiling and the stochastic nature of nuclear reactions that can be designated as power perturbations [141]. On the other hand, a transient is defined as an event in which a plant transitions from a normal state to an abnormal one. In nuclear power plants (NPPs), early identification of perturbations and transient types is crucial for initiating timely and appropriate responses. Additionally, classifying novel transients as "unknown" when they fall outside the plant's existing knowledge base is essential for ensuring safety and guiding further analysis. [142].

Testing accident scenarios and the impact of power perturbations and transients on the reactor core, fuel rods, and coolant requires extensive simulations across a wide range of conditions. These simulations are time-consuming and costly, as they involve computational fluid dynamics (CFD) models that run for multiple days and demand access to high-performance computing resources. Reduced-order models that effectively capture the critical events and dynamics of these scenarios are therefore essential for efficient verification, validation, and testing. Furthermore, if a single, interpretable model can capture the effects of these perturbations, rather than relying on black-box approaches, it enables the classification of power inputs based solely on sensor measurements, thereby closing the loop between input and resulting field dynamics.

Additionally, nuclear power plants are complex systems managed by human operators, who must diagnose and address unplanned power perturbations, such as accidents, equipment failures, or external disturbances. The diagnosis relies on readings from numerous instruments, making it challenging, especially as anomalies often develop gradually. In some cases, early-stage anomalies may not produce clear signals, increasing the risk of delayed operator response, which could hinder efforts to mitigate or minimize potential negative consequences [143]. One approach utilizes probabilistic neural networks (PNNs) for diagnosing transients in nuclear power plants to classify novel events as “don’t-know” when they do not match any existing knowledge within the system’s database using evidence accumulation [144].

So far, in this thesis we have seen that the strategic placement of sensors critically enables reconstruction of latent reactor flow fields from sparse, heavily constrained measurements. In this chapter, to further enhance monitoring and control, we also address the effects of power perturbations on reactor core coolant temperature, pressure, and velocity—essential for real-time safety control. Our optimization procedure leverages ROMs, including dynamic mode decomposition with control, to uncover the underlying dynamics of complex systems, advancing the goal of a robust digital twin for nuclear assets. Moreover, our methodology adapts to transient conditions by optimizing sensor locations and sampling intervals. Tested on the OPTI-TWIST prototype vessel, this approach demonstrates the impact of different ROMs on sensor placement and flow reconstruction performance. Integrating linear discriminant analysis (LDA) and dynamic mode decomposition with control (DMDc) allows classification of transient regimes, enabling accurate monitoring of varying operational states. Overall, these contributions reinforce the digital twin’s ability to provide reliable, real-time insights, enhancing both safety and operational efficiency in nuclear-integrated systems.

We begin by presenting the methodologies of Dynamic Mode Decomposition with Control (DMDc) and Linear Discriminant Analysis (LDA), highlighting their application in optimizing sensor placement and classifying power input regimes. Our analysis first demonstrates these techniques applied to OPTI-TWIST CFD simulations at three distinct power levels, effectively classifying the inputs and revealing their temporal dependencies. We then demon-

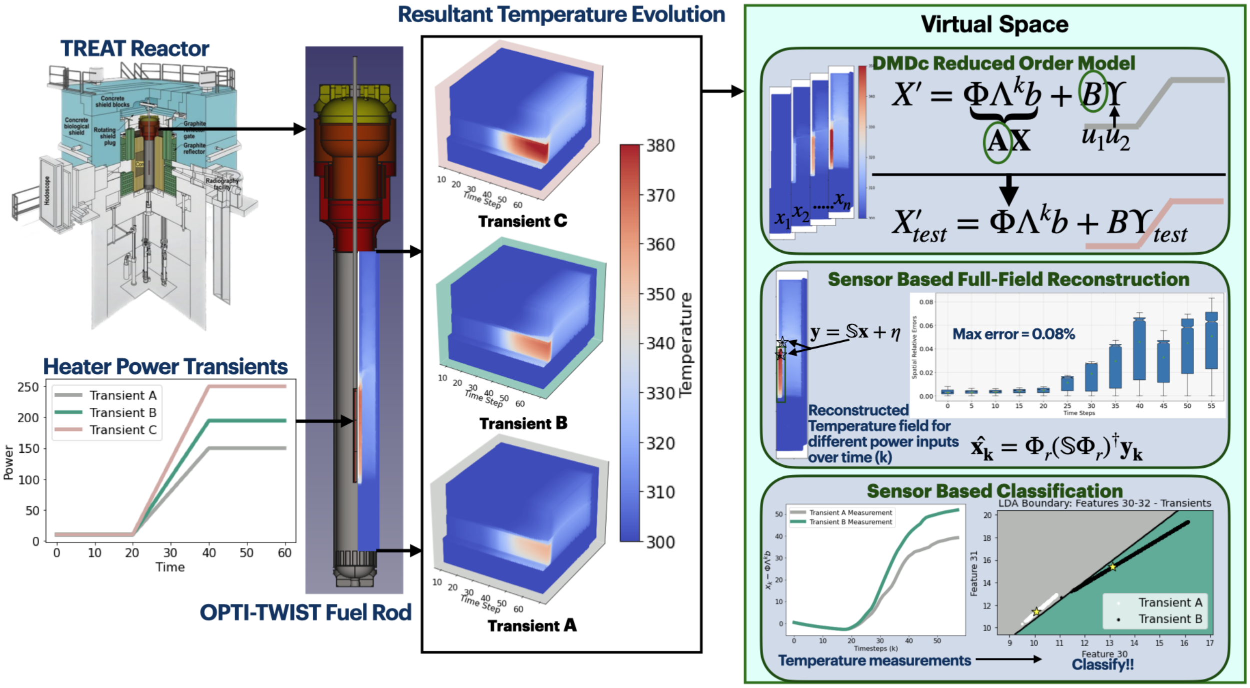

Figure 5.1: Power levels starting at 10 W and ramping up to 150 W, 200 W, and 250 W result in distinct temperature profiles that must be accurately captured by a unified model. Dynamic Mode Decomposition (DMD) offers this versatility by directly incorporating power variations into the system dynamics, enabling sensor optimization, accurate reconstruction of flow fields, and input classification to identify the factors driving different dynamic behaviors.

strate classification of power profiles using real-time infrared camera data from OPTI-TWIST experiments, distinguishing between 250W and 1200W power inputs through the developed methodology applied to thermal imaging data.

5.1 *Dynamic Mode Decomposition with control (DMDc)*

Dynamic Mode Decomposition with Control (DMDc) is an extension of the standard Dynamic Mode Decomposition (DMD) method, designed to incorporate control inputs into the system identification process as shown by Proctor et al [145]. The goal of DMDc is to decompose a system into dynamic modes while accounting for external control inputs. Consider the following discrete-time linear system with control:

$$\mathbf{x}_{k+1} = \mathbf{A}\mathbf{x}_k + \mathbf{B}\mathbf{u}_k, \tag{5.1}$$

where $\mathbf{x}_k \in \mathbb{R}^n$ is the system state and $\mathbf{u}_k \in \mathbb{R}^m$ is the control input at time step k, $\mathbf{A} \in \mathbb{R}^{n\times n}$ is the system matrix and $\mathbf{B} \in \mathbb{R}^{n\times m}$ is the control matrix. In DMDc, we aim to approximate $\mathbf{A}$ and $\mathbf{B}$ from data. Given a sequence of m snapshots of state data we have the state matrix $\mathbf{X}$, the time shifted snapshot matrix $\mathbf{X}'$ and $\boldsymbol{\Upsilon}$ the control input matrix that satisfies $\mathbf{X}' = \mathbf{A}\mathbf{X} + \mathbf{B}\boldsymbol{\Upsilon}$.

$$\mathbf{X} = \begin{bmatrix}\mathbf{x}_1 & \mathbf{x}_2 & \cdots & \mathbf{x}_{m-1}\end{bmatrix}, \quad \mathbf{X}' = \begin{bmatrix}\mathbf{x}_2 & \mathbf{x}_3 & \cdots & \mathbf{x}_m\end{bmatrix}, \boldsymbol{\Upsilon} = \begin{bmatrix}\mathbf{u}_1 & \mathbf{u}_2 & \cdots & \mathbf{u}_{m-1}\end{bmatrix},$$

Utilizing the three data matrices, approximations of the linear mappings $\mathbf{A}$ and $\mathbf{B}$ can be found. We outline the analysis and algorithm for when matrix $\mathbf{B}$ is unknown as the assumption that $\mathbf{B}$ is know suggests knowledge of how the control procedures affect the system. The dynamical system can be represented as:

$$\begin{bmatrix}\mathbf{X}'\end{bmatrix} \approx \begin{bmatrix}\mathbf{A} & \mathbf{B}\end{bmatrix}\begin{bmatrix}\mathbf{X}\\ \boldsymbol{\Upsilon}\end{bmatrix} = \mathbf{G}\boldsymbol{\Omega}.$$

where $\boldsymbol{\Omega}$ contains both the state and control snapshot information. We seek the best fit solution of the operator $\mathbf{G}$ which contains the process dynamics $\mathbf{A}$ and input matrix $\mathbf{B}$. The first step involves performing a singular value decomposition (SVD) as $\boldsymbol{\Omega} = \mathbf{U}\boldsymbol{\Sigma}\mathbf{V}^* \approx \tilde{\mathbf{U}}\tilde{\boldsymbol{\Sigma}}\tilde{\mathbf{V}}^*$. The approximation of $\mathbf{G}$ is given by the following description:

$$\mathbf{G} \approx \bar{\mathbf{G}} = \mathbf{X}'\tilde{\mathbf{V}}\tilde{\boldsymbol{\Sigma}}^{-1}\tilde{\mathbf{U}}^*$$

The linear operator $\tilde{\mathbf{U}}$ can be broken into two separate components to find approximations to $\mathbf{A}$ and $\mathbf{B}$ as:

$$\begin{aligned}[\mathbf{A}, \mathbf{B}] &\approx [\bar{\mathbf{A}}, \bar{\mathbf{B}}] && (5.2)\\ &\approx \left[\mathbf{X}'\tilde{\mathbf{V}}\tilde{\boldsymbol{\Sigma}}^{-1}\tilde{\mathbf{U}}_1^*, \mathbf{X}'\tilde{\mathbf{V}}\tilde{\boldsymbol{\Sigma}}^{-1}\tilde{\mathbf{U}}_2^*\right] && (5.3)\end{aligned}$$

where $\tilde{\mathbf{U}}_\mathbf{1} \in \mathbb{R}^{n\times p}$, $\tilde{\mathbf{U}}_\mathbf{2} \in \mathbb{R}^{m\times p}$ and $\tilde{\mathbf{U}} = [\tilde{\mathbf{U}}_\mathbf{1}^{*}\tilde{\mathbf{U}}_\mathbf{2}^{*}]^T$. For large dimensional systems where $n >> 1$, a dynamic model defined by $\bar{\mathbf{A}}$ and $\bar{\mathbf{B}}$ is computationally prohibitive and a reduced order model of rank $r << n$ is required where $\mathbf{x} = \mathbf{P}\tilde{\mathbf{x}}$ and $\tilde{\mathbf{x}} \in \mathbb{R}^r$. For DMD the left singular vectors $\tilde{\mathbf{U}}$ provide the linear subspace of dimension r on which the state space evolves and thus $\mathbf{P} = \tilde{\mathbf{U}}$. For DMDc the truncated left singular vectors of $\mathbf{\Sigma}$ define the input space and $\tilde{\mathbf{U}}$ cannot be used as the transformation operator. To define $\mathbf{P}$ we require the reduced-order subspace of the output space. A second singular value decomposition of the time-shifted data matrix $\mathbf{X}' = \hat{\mathbf{U}}\hat{\mathbf{\Sigma}}\hat{\mathbf{V}}^*$ with a truncation value r gives us the transformation $\mathbf{x} = \hat{\mathbf{U}}\tilde{\mathbf{x}}$ and reduced-order approximation of $\mathbf{A}$ and $\mathbf{B}$. The rank of truncation of the two SVDs is most likely different and $p > r$. The reduced matrices $\tilde{\mathbf{A}}$ and $\tilde{\mathbf{B}}$ are:

$$\tilde{\mathbf{A}} = \hat{\mathbf{U}}^*\bar{\mathbf{A}}\hat{\mathbf{U}} = \hat{\mathbf{U}}^*\mathbf{X}'\tilde{\mathbf{V}}\tilde{\mathbf{\Sigma}}^{-1}\tilde{\mathbf{U}}_1^*\hat{\mathbf{U}} \tag{5.4}$$

$$\tilde{\mathbf{B}} = \hat{\mathbf{U}}^*\bar{\mathbf{B}} = \hat{\mathbf{U}}^*\mathbf{X}'\tilde{\mathbf{V}}\tilde{\mathbf{\Sigma}}^{-1}\tilde{\mathbf{U}}_2^* \tag{5.5}$$

where $\tilde{\mathbf{A}} \in \mathbb{R}^{r\times r}$ and $\tilde{\mathbf{B}} \in \mathbb{R}^{r\times l}$. The dynamic modes of $\mathbf{A}$ are found through the eigenvalue decomposition $\tilde{\mathbf{A}}\mathbf{W} = \mathbf{W}\mathbf{\Lambda}$, where the diagonal of matrix $\mathbf{\Lambda}$ are also the eigenvalues of the full matrix $\mathbf{A}$. The columns of $\mathbf{W}$ are eigenvectors of the reduced matrix $\tilde{\mathbf{A}}$ and the DMDc modes $\mathbf{\Phi}$ which are the eigenvectors of the high-dimensional $\mathbf{A}$ matrix are given by the following equation:

$$\mathbf{\Phi} = \mathbf{X}'\tilde{\mathbf{V}}\mathbf{\Sigma}^{-1}\tilde{\mathbf{U}}_\mathbf{1}^{*}\hat{\mathbf{U}}\mathbf{W}$$

The system state can be expanded in terms of a data-driven spectral decomposition:

$$\mathbf{x_k} = \sum_{j=1}^{r} \boldsymbol{\phi}_j \lambda_j^{k-1} b_j + \mathbf{B}\mathbf{u}_{k-1} \tag{5.6}$$

where the vector $\mathbf{b}$ are the mode amplitudes generally computed as $\mathbf{b} = \mathbf{\Phi}^{\dagger}\mathbf{x_1}$ using the first snapshot to determine the mixture of DMDc mode amplitudes.

5.2 Linear Discriminant Analysis (LDA)

Linear Discriminant Analysis (LDA) is a dimensionality reduction technique commonly used for classification tasks. LDA seeks to find a linear combination of features that best separates two or more classes by maximizing the separability between them. It achieves this by minimizing the within-class scatter through matrix $\mathbf{S}_w$ shown in Equation 5.7 while maximizing the between-class scatter through matrix $\mathbf{S}_b$ as in Equation 5.8.

$$\mathbf{S}_w = \sum_{i=1}^{C} \sum_{j=1}^{N_i} (\mathbf{x}_j^{(i)} - \boldsymbol{\mu}_i)(\mathbf{x}_j^{(i)} - \boldsymbol{\mu}_i)^T \tag{5.7}$$

$$\mathbf{S}_b = \sum_{i=1}^{C} N_i (\boldsymbol{\mu}_i - \boldsymbol{\mu})(\boldsymbol{\mu}_i - \boldsymbol{\mu})^T \tag{5.8}$$

where $\boldsymbol{\mu}_i$ is the mean vector of class i and $\boldsymbol{\mu}$ is the overall mean vector of the entire dataset:

$$\boldsymbol{\mu}_i = \frac{1}{N_i} \sum_{j=1}^{N_i} \mathbf{x}_j^{(i)}, \boldsymbol{\mu} = \frac{1}{N} \sum_{i=1}^{C} \sum_{j=1}^{N_i} \mathbf{x}_j^{(i)} \tag{5.9}$$

The goal of LDA is to find a projection matrix $\mathbf{W}$ that maximizes the ratio of the determinant of the between-class scatter matrix to the determinant of the within-class scatter matrix after projection:

$$\mathbf{W} = \arg\max_{\mathbf{W}} \frac{|\mathbf{W}^T \mathbf{S}_b \mathbf{W}|}{|\mathbf{W}^T \mathbf{S}_w \mathbf{W}|} \tag{5.10}$$

This optimization problem reduces to solving the generalized eigenvalue problem $\mathbf{S}_b \mathbf{w} = \lambda \mathbf{S}_w \mathbf{w}$ where λ represents the eigenvalues, and the corresponding eigenvectors $\mathbf{w}$ form the columns of the projection matrix $\mathbf{W}$.

5.3 Power Input Classifier Trained on DMDc Twin

System Identification through DMDc provides an approximation to the state matrix $\mathbf{A}$, control matrix $\mathbf{B}$, and DMDc modes $\boldsymbol{\Phi}$. Consider sensors measurements of the field to be reconstructed given as $\mathbf{y} = \mathbb{S}\mathbf{x} + \eta$, where $\mathbb{S}$ is the selection matrix (Equation 5.11). Optimal locations for these sensors can be determined using POD modes $\boldsymbol{\Psi}$ as a basis, where, $\boldsymbol{\Psi}_\mathbf{r} = \mathbf{U}_\mathbf{r}$ are the left singular vectors of the singular value decomposition. However, as the sensor selection methodology developed in [13] can be used with any tailored basis, sensors can also be determined using the DMDc modes $\boldsymbol{\Phi}$. Near optimal sensor placements are determined using the D-optimal, greedy objective which is solved using QR-pivoting (Equation 5.12).

$$\mathbb{S} = \begin{bmatrix}\mathbf{e}_{\gamma_1} & \mathbf{e}_{\gamma_2} & \dots & \mathbf{e}_{\gamma_p}\end{bmatrix}^T, \tag{5.11}$$

$$\gamma_* = \underset{\gamma,|\gamma|=p}{\operatorname{argmax}} \ \log\det((\mathbb{S}\Phi_r)^T(\mathbb{S}\Phi_r)). \tag{5.12}$$

Dynamic Mode Decomposition excels at capturing time-dependent behavior and transient regimes more effectively than Proper Orthogonal Decomposition as it directly integrates temporal dynamics into the decomposition process, enabling the identification of coherent structures and their evolution over time without assuming orthogonality or static modes. DMDc also takes into consideration effect of control inputs on dynamics which can be seen in the data-driven spectral decomposition (Equation 5.6). Using sensor measurements determined through DMDc modes, the effect of the control input can be isolated and control trajectories can be classified through sensor measurements and reconstruction of the initial condition through $\mathbf{b} = \mathbf{\Phi}^\dagger \mathbf{x_1}$.

- **Classification from sensor measurements:** Based on sensor measurements of the initial state $\mathbf{y}_1 = \mathbb{S}\mathbf{x}_1$, the amplitudes of the DMDc modes can be approximated as $\mathbf{b} = \mathbf{\Phi}^\dagger \hat{\mathbf{y}}_\mathbf{1}$. The influence of control can be isolated as:

  $$\hat{\mathbf{y}}_k - \mathbf{\Phi\Lambda}^{k-1}\Phi^\dagger\hat{\mathbf{y}}_\mathbf{1} = \mathbf{B\Upsilon}_{k-1} \tag{5.13}$$

  A classifier such as LDA can be fit to the residual $\hat{\mathbf{y}}_k - \mathbf{\Phi\Lambda}^{k-1}\Phi^\dagger\hat{\mathbf{y}}_\mathbf{1}$ for every time-step and as the power perturbation occurs the trained classifier can determine which residual was caused by which power.

- **Classification from reconstruction:** The initial state can be reconstructed through gappy DMDc and the amplitudes of the DMDc modes can be approximated as $\mathbf{b} = (\mathbb{S}\Phi)^\dagger\mathbb{S}\hat{\mathbf{x}_\mathbf{1}}$. Subsequently, the influence of control can be isolated as:

  $$\mathbb{S}\mathbf{x}_k - \mathbb{S}\mathbf{\Phi\Lambda}^{k-1}(\mathbb{S}\Phi)^\dagger\mathbb{S}\hat{\mathbf{x}_\mathbf{1}} = \mathbf{B\Upsilon}_{k-1} \tag{5.14}$$

A classifier such as LDA can be fit to the residual $\mathbb{S}\mathbf{x}_k - \mathbb{S}\mathbf{\Phi}\mathbf{\Lambda}^{k-1}(\mathbb{S}\Phi)^{\dagger}\mathbb{S}\hat{\mathbf{x}_0}$ for every time-step and every location of the reconstructed field. As the power perturbation occurs the trained classifier can determine which residual was caused by which power.

5.4 Results

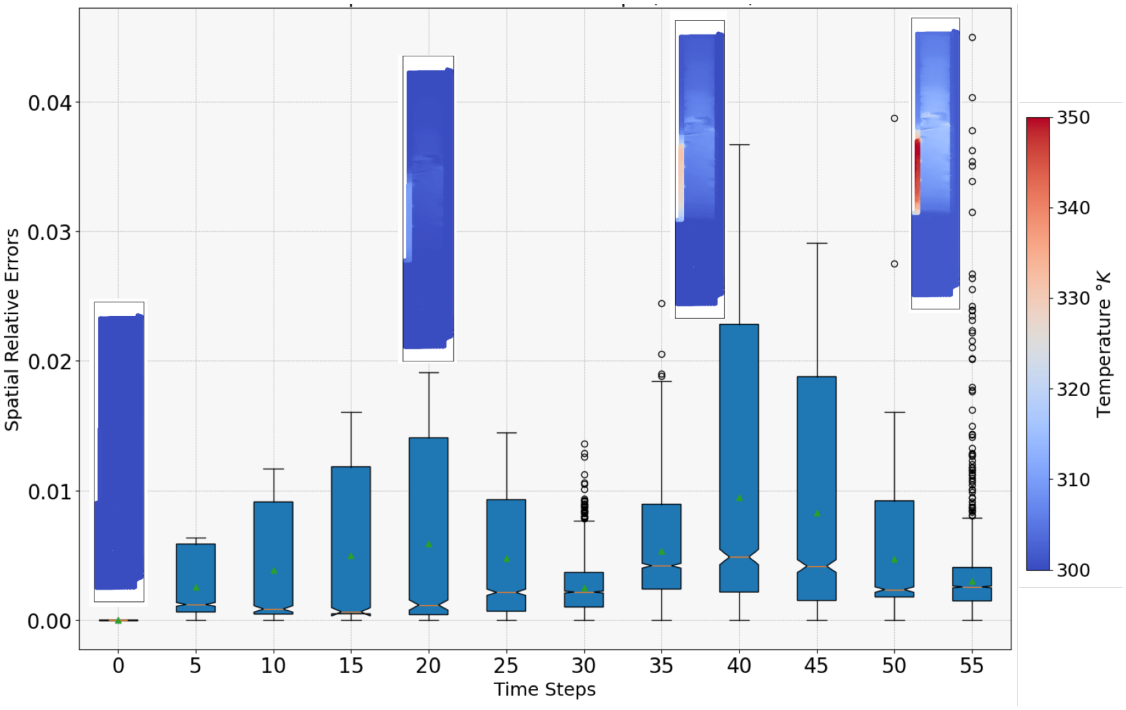

Figure 5.2: DMDc model captures flow dynamics with just 2 modes. The DMDc-based reconstruction of the temperature field across all time steps—spanning before, during, and after the power perturbation—achieves a maximum relative error of just 0.04.

This section demonstrates DMDc-based sensor placement for reconstruction and classification using reduced-order models applied to OPTI-TWIST CFD power transient simulations. Subsequently, we investigate power classification from real-world thermal imaging of the OPTI-TWIST capsule during experimentation, utilizing the same DMDc modeling approach.

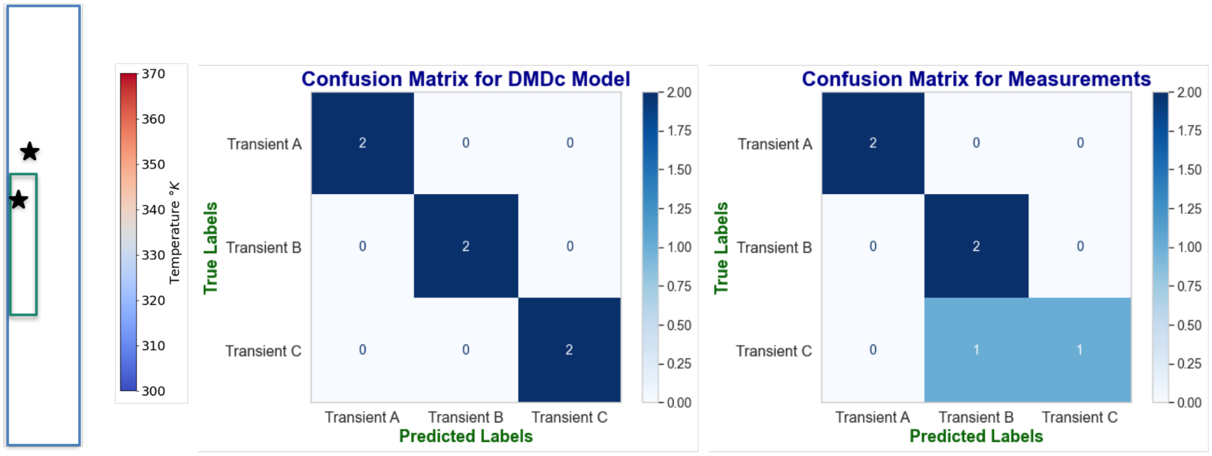

(a) Sensors (b) DMDc Model is essential. (c) Direct classification fails

Figure 5.3: The DMDc reduced-order model enables accurate classification of power inputs solely from sensor measurements (b), whereas direct classification based on the raw sensor data often leads to incorrect results (c). Sensor locations shown by (a).

5.4.1 CFD Simulation Power Transients Analysis

In this section, we present the DMDc based reconstruction, where the model is trained on transient A, characterized by a power ramp-up from 10 W to 150 W, as depicted in the Figure 5.1. Figure 5.2 illustrates the reconstruction results for a test case using transient B, which ramps from 10 W to 200 W. The maximum relative error observed is 0.04, as indicated by the error bars. The reconstruction demonstrates that just two modes are sufficient to accurately capture the heat transfer dynamics during the fuel rod heating process. This begins around $t = 20$, as power ramps up, and continues until the system stabilizes. During this period, the development of convection currents facilitates the progressive heating of the water due to heat transfer from the fuel rod, with temperatures continuing to rise until approximately $t = 60$.

Using the identified DMDc modes, we strategically place sensors as outlined in the earlier section 5.3, with their locations depicted in Figure 5.3a. The classification process begins by analyzing the residuals derived from approximating **b** using sensor measurements. As shown in the figure, the Linear Discriminant Analysis (LDA) classifier achieves 100% accuracy when trained on these residuals, effectively distinguishing between power transients A, B, and C Figure 5.3b. In contrast, direct classification without leveraging the intermediate DMDc model leads to misclassification between transients B and C, underscoring the advantage of incorporating the DMDc framework for improved classification Figure 5.3c. It is crucial to note that the DMDc model is trained on Transient A but has no information of Transient B or C and is successful in classifying all three of them.

Next, the reconstruction of the entire field is performed using two sensor measurements of the initial condition, which are then utilized to calculate the mode amplitudes **b** (Figure 5.4a). This enables classification not only based on the two sensor readings but for the entire field, comprising approximately 40,000 data points. An LDA classifier is then applied to the residuals of a randomly selected subset of data points from the three different

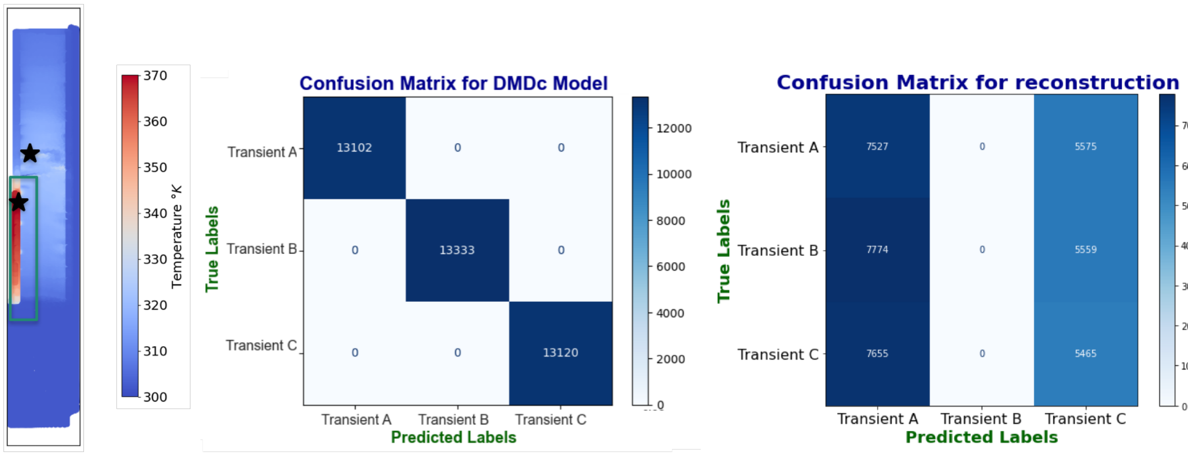

(a) Reconstruct (b) DMDc Model is essential. (c) Direct classification fails

Figure 5.4: The DMDc reduced-order model enables accurate classification of power inputs from reconstructed temperature field (b), whereas direct classification based on the raw reconstruction often leads to incorrect results (c). Sensor locations shown by (a).

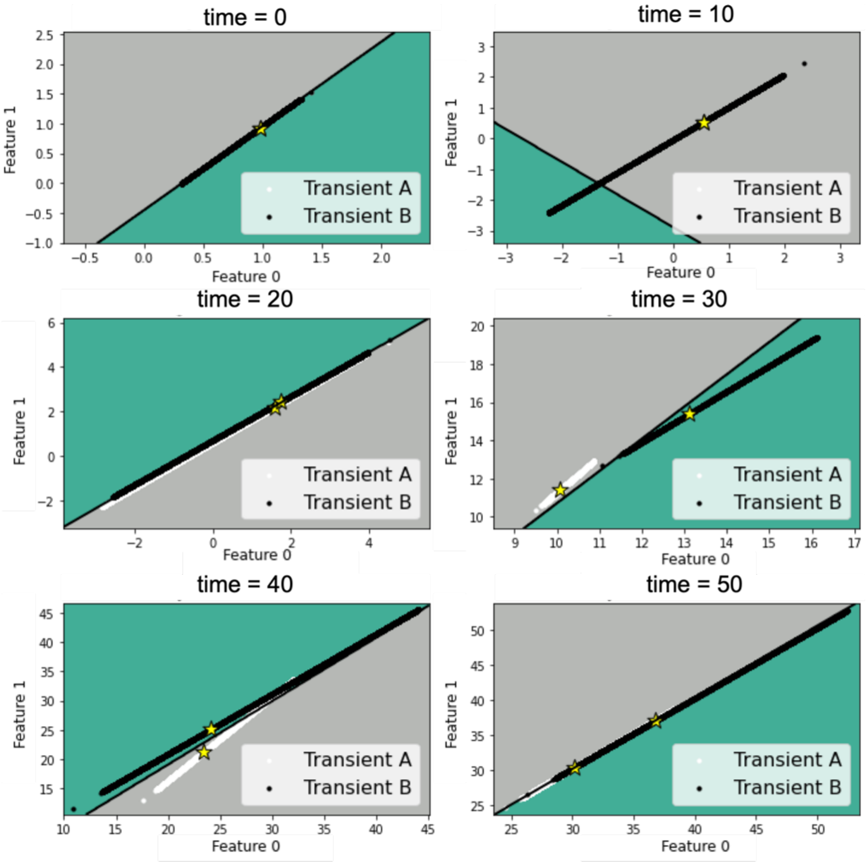

Figure 5.5: The LDA boundary between the two features, Transient A and Transient B, struggles to classify correctly when the power inputs are identical (at times 0, 10, and 20). However, as the power inputs diverge due to perturbations, the LDA boundary improves classification accuracy, as demonstrated at times 30 and 40.

transient reconstructions, as described in Equation 5.14. This approach achieves 100% classification accuracy (Figure 5.4b). However, when the classifier is directly applied to the raw measurements without leveraging the DMDc model, it results in significant misclassification errors (Figure 5.4c). An important observation is that the trained classifier struggles to differentiate between the residuals when the power levels for all three transients (A, B, and C) are identical at 10 W. However, as the power levels begin to diverge and ramp up around time = 30, the classifier trained on the residuals distinctly separates the reconstructed data points corresponding to the three profiles Figure 5.5. This behavior underscores the utility of digital twins: when power levels remain constant, it can be inferred that the system is operating under normal conditions. Conversely, when the LDA classifier begins to delineate boundaries between profiles, it indicates that the power has deviated, signaling a perturbation. This capability is instrumental in enabling real-time monitoring and control, ensuring timely detection and response to operational changes.

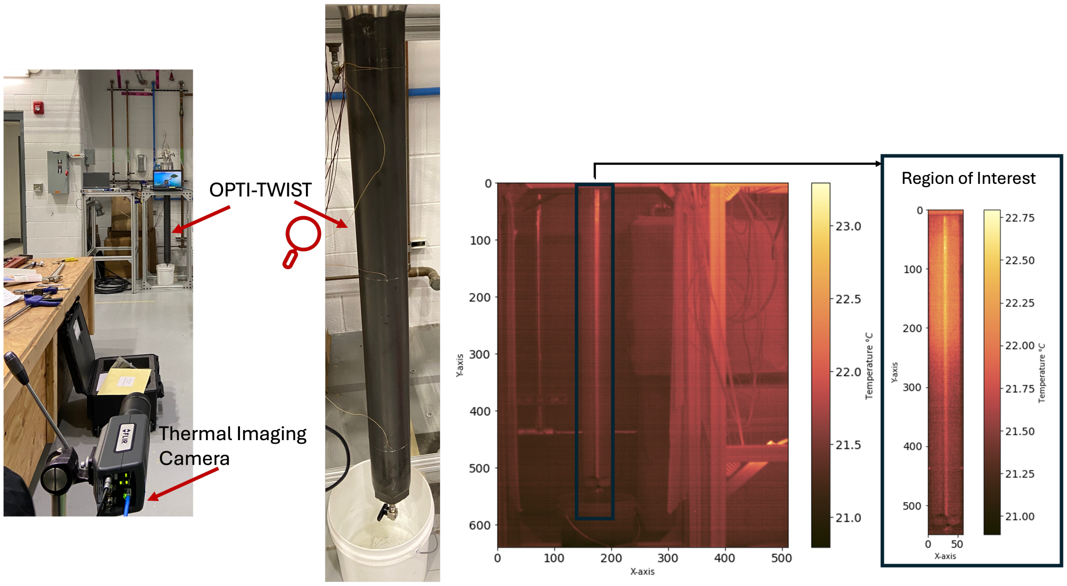

(a) Experimental Setup (b) Thermal Image with Region of Interest (ROI)

Figure 5.6: Thermal imaging of temperature fields from OPTI-TWIST heater power perturbations during experimentation (a), require preprocessing to identify regions of interest and optimal sensor locations for power input classification (b).

5.4.2 Experimental Thermal Imaging Analysis

This section investigates the classification of temperature profiles acquired through real-time thermal imaging during OPTI-TWIST experimentation, where heater power was systematically varied between 250W and 1200W across distinct experimental configurations. The temperature fields were captured using a thermal imaging camera as depicted in the Figure 5.6a, providing spatially-resolved thermal data for subsequent analysis (Figure 5.6b). A fundamental objective in digital twin development is the capability to distinguish between different power operating conditions based solely on temperature measurements. To achieve this classification goal, we initially determined optimal sampling locations within the thermal imaging dataset, with these sampling points representing strategic sensor placement positions for effective power state classification using DMDc.

The sampling points are selected through fitting a DMDc basis to the time-dependent thermal imaging dataset using Equation 5.12 shown by white circles in Figure 5.7a and Figure 5.7b . They also illustrate the temperature profiles for both power transients at the final temporal snapshot (t = 599). The maximum relative reconstruction error of the test set (250W) power profile is 0.25 as shown in Figure 5.7c while the subsequent figure displays the temperature measurements recorded at these sensor locations for the two distinct power operating conditions. The objective is to classify these power states based on the sensor measurements obtained at the optimally selected locations.

The storage and real-time classification of high-dimensional thermal imaging data presents significant computational challenges, necessitating strategic sampling approaches for effective system monitoring. As demonstrated in Figure 5.8c, classification based on random sampling from thermal imaging data results in three misclassifications of 1200W temperature profile data points as 250W conditions. Such classification errors pose substantial risks in real-time monitoring and control applications for digital twin systems in nuclear environments, where accurate power state identification is critical for operational safety and system integrity.

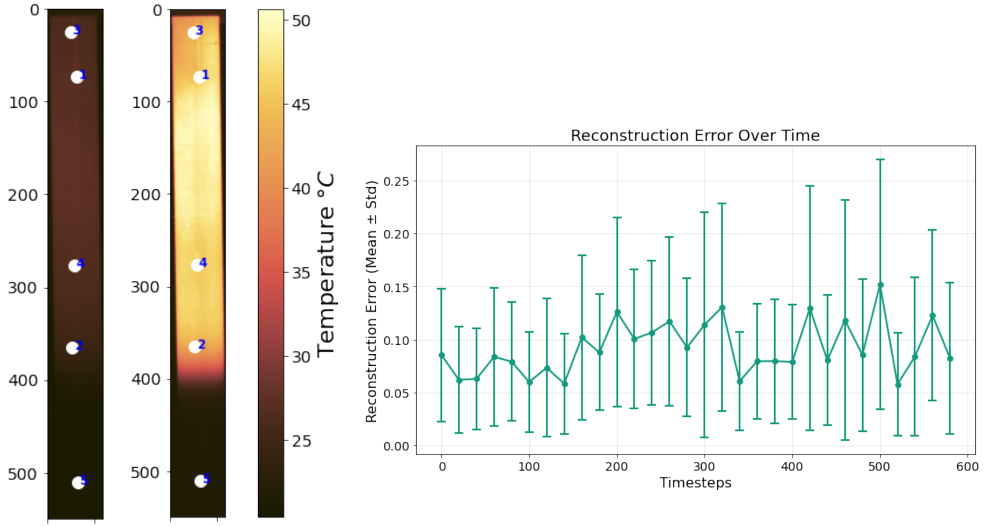

(a) 250W (b) 1200W (c) Sensor based reconstruction has maximum error = 0.25

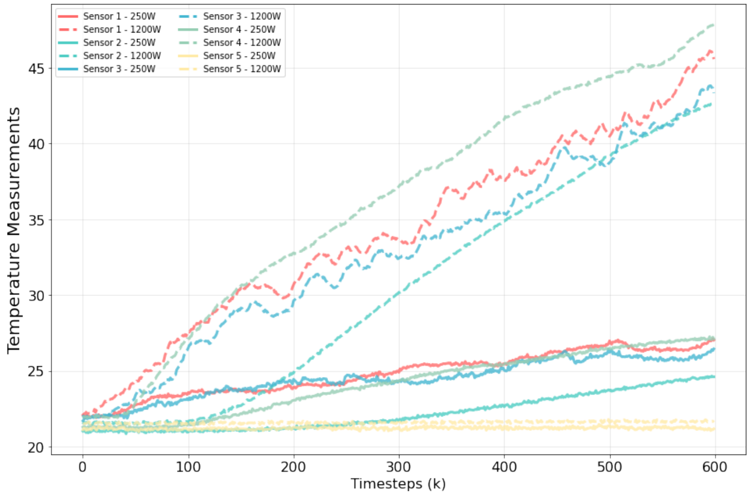

(d) Sensor measurements for 250W and 1200W power.

Figure 5.7: Optimal sampling locations (white dots) (a),(b) determined through sensor placement optimization for reconstruction as detailed in section 3.3, achieving a maximum reconstruction error of 0.25 for test power (250W) (c). Temperature measurements from these strategically positioned sensors are presented in (d) and serve as input data for power classification analysis.

In contrast, classification using optimally positioned sensor measurements reduces misclassification to a single instance, where one 1200W measurement is incorrectly identified as 250W (Figure 5.8a). However, the most robust classification performance is achieved through the application of classifiers trained on DMDc residuals, as detailed in Section X, which demonstrates 100% classification accuracy (Figure 5.8b). This superior performance stems from the DMDc framework's incorporation of the control matrix $\mathbf{B}$, enabling the model to effectively capture and learn the relationship between different control parameters and their corresponding influence on the temperature profile evolution. The inclusion of control-aware dynamics in the DMDc formulation provides a more comprehensive understanding of the system behavior under varying power conditions, thereby enabling precise discrimination between operational states.

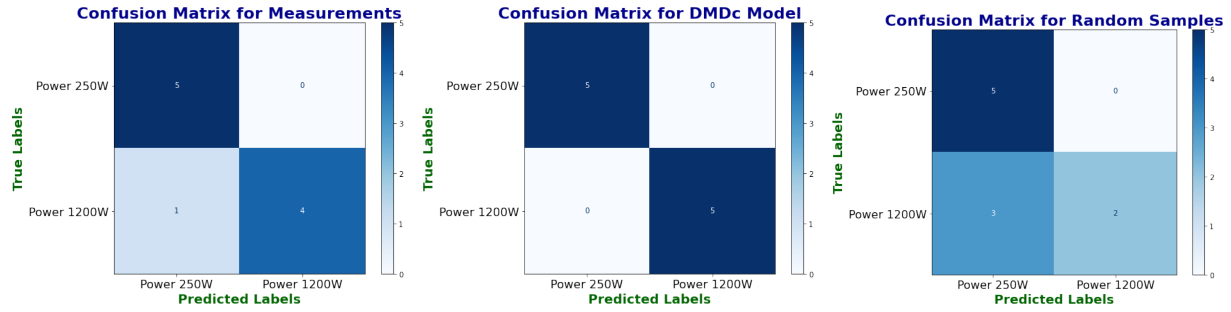

(a) Optimization essential (b) DMDc Model essential (c) Direct classification fails

Figure 5.8: Classification from strategically placed sensors results in a single misclassification among sensor readings (a), whereas classification using DMDc residuals from sensor measurements demonstrates perfect 100% accuracy. Conversely, random classification of thermal imaging data yields the poorest performance (c).

5.5 Conclusion

This work demonstrates the efficacy of combining Dynamic Mode Decomposition with Control (DMDc) and Linear Discriminant Analysis (LDA) for sensor placement, field reconstruction, and classification in transient systems. By leveraging DMDc-based reconstructions, we effectively captured the temporal and spatial dynamics of heat transfer in power ramp scenarios using minimal sensor data. The results show that as few as two modes are sufficient to model the system's behavior during transient heating phases, enabling accurate reconstructions even for large-scale fields with approximately 40,000 data points.

Through strategic sensor placement informed by DMDc modes, we achieved robust classification of power transients using LDA applied to residuals, demonstrating 100% accuracy. This underscores the advantage of coupling model-based reconstructions with data-driven classification techniques, as direct classification on raw measurements yielded significant errors. Furthermore, the classifier's inability to distinguish between transients at identical power levels highlights its capability to monitor normal operating conditions. Once the power levels began diverging, the classifier reliably identified deviations, enabling the detection of perturbed conditions.

The experimental validation using OPTI-TWIST thermal imaging data confirms that strategic sensor placement optimization significantly outperforms random sampling approaches for power classification tasks. While random classification of thermal imaging data resulted in substantial misclassification rates, with three 1200W temperature profile data points incorrectly identified as 250W conditions, the implementation of optimally positioned sensors reduced classification errors to a single misclassification instance. The superior performance achieved through DMDc-based classification of sensor measurement residuals, demonstrating 100% classification accuracy, highlights the critical importance of incorporating control-aware dynamics in the modeling framework.

These findings showcase how integrating reduced-order modeling with advanced sensing and classification methodologies facilitates real-time monitoring and control. This approach provides a framework for digital twins in engineering systems, ensuring efficient and accurate system analysis while supporting predictive maintenance and operational optimization.

To advance this work, it is essential to extend the approach to more complex flow scenarios, such as cavity-driven flows under turbulent conditions. This will provide deeper insights into the reconstruction capabilities of sensors identified by DMDc and POD, as well as the impact of orthogonality loss on uncertainty estimation and model performance.

Chapter 6

CONCLUSION AND OUTLOOK

In this thesis, we develop data-driven, scalable methodologies for sensor placement in nuclear energy systems, utilizing reduced-order models and constrained sensing techniques. Using ROMs based on modal decompositions introduced in [13], we efficiently capture the points of highest variance in the data using simple linear algebra methods such as gappy POD and QR pivoting. This allows the algorithms to operate in seconds, even for extremely high-dimensional systems $\mathcal{O}(10^7)$. We demonstrate that incorporating constraints into the QR pivoting procedure after the initial sensor placements ensures minimal loss of optimality while achieving reconstruction performance comparable to the unconstrained QR approach. We compare our near-optimal sensor placements to intuitive, randomly chosen placements, which are commonly used in engineering due to their practicality and ease of installation and maintenance. While such random placements are convenient, they often lack the precision needed for accurate global inference in complex systems. By incorporating the constrained procedure described above during the design phase of a physical system, it becomes possible to determine optimal sensor locations while accounting for practical considerations such as manufacturing constraints and experimental requirements. This approach ensures a balance between theoretical optimality and real-world feasibility.

These constraints can be tailored to specific user requirements, such as enforcing a fixed or maximum number of sensors within a given region, optimizing additional sensor placements after an initial set has been predetermined, or ensuring that sensors maintain a specified minimum distance from each other. The proposed algorithm is highly flexible and can accommodate additional constraints beyond those mentioned, making it adaptable to a wide range of real-world scenarios. Moreover, estimating errors from noisy sensor measurements is crucial for digital twins, as it enables twin recalibration and early detection of anomalies. Additionally, uncertainty heatmaps illustrate how imposing sensor placement constraints affects reconstruction uncertainty in specific regions, providing valuable insights necessary for building reliable and robust digital twins.

In Chapter 3 and Chapter 4, we demonstrate the application of constrained sensing to fuel rods, irradiation experiments, and steam generators by utilizing simulation data generated during the design phase to strategically place sensors. This approach aligns with the digital twin paradigm, where data collected throughout the product lifecycle is leveraged to develop reduced-order models and guide optimal sensor placement. Once the physical prototype is operational, real-time streaming measurements can be continuously compared with these models for real-time monitoring and validation. Additionally, within the steam generator, we show how patterns in other quantities, such as heat flux, can be inferred by analyzing temperature modes, offering a powerful tool for solving inverse problems and enhancing system understanding. Furthermore, uncertainty estimates provide essential guidelines on where measurements and subsequent reconstructions can be most trusted, improving the interpretability of digital twins and ensuring more reliable decision-making during operation.

In Chapter 5, we extended our methodology to enhance real-time monitoring and control by addressing the effects of power perturbations on key reactor core parameters such as coolant temperature, pressure, and velocity—critical for ensuring safety in nuclear systems. To achieve this, we employ Dynamic Mode Decomposition with Control (DMDc) developed by Proctor et al [145], to uncover the dominant dynamics governing complex systems. DMDc, in particular, enables the separation of internal state dynamics from external actuation effects, making it highly suitable for systems with active controls and for system identification.

Furthermore, by integrating Linear Discriminant Analysis (LDA) with DMDc, we facilitate the classification of transient regimes, enabling precise identification and monitoring of varying operational states. The ability to accurately classify power states from real-world experimental thermal imaging data, as demonstrated in this work, is critical for ensuring reliable system monitoring and operational safety in complex thermal systems. The integration of reduced-order modeling with optimized sensing strategies significantly enhances safety margins through real-time state identification capabilities, establishing a foundation for advanced monitoring and control applications in nuclear energy systems.

6.1 Open Source Code Contributions

To enhance the accessibility and adoption of data-driven sensor placement techniques within the broader engineering community, the development of comprehensive code packages is essential. Such packages enable widespread utilization of these methodologies by multiple practitioners and researchers across diverse applications, ranging from biological dataset analysis [61] to space debris modeling [146] and other complex engineering problems. `PySensors` is a Python package [147] dedicated to solving the complex challenge of optimal sensor placement in data-driven systems. It implements advanced sparse optimization algorithms that use dimensionality reduction techniques to identify the most informative measurement locations with remarkable efficiency [13, 6, 86].

`RAVEN` is a generic software framework for parametric and probabilistic analysis of complex system codes, originally developed for dynamic risk analysis at Idaho National Laboratory but now serving as a multi-purpose uncertainty quantification platform capable of interfacing with any system code [148]. The framework's robust capability to investigate system responses and explore input spaces through diverse sampling methodologies—including Monte Carlo, grid-based, and Latin hypercube schemes—creates an ideal foundation for advanced sensor placement optimization.

By integrating sensor placement capabilities into RAVEN, we unlock enhanced system observability, improved detection sensitivity, and robust digital twinning for nuclear applications. RAVEN's sampling algorithms efficiently identify optimal monitoring locations, creating strategically positioned sensor networks that feed high-fidelity data to digital twins. This synergy establishes a powerful feedback loop: digital twins gain predictive accuracy from targeted sensor data, while sensor placement optimization benefits from the twin's evolving system understanding. The result is more reliable virtual monitoring, predictive maintenance, and operational decision-making across nuclear systems.

6.1.1 Pysensors 2.0

The previous version of `Pysensors` incorporated two distinct sensor placement methodologies: (1) an unconstrained optimization approach utilizing `QR` decomposition, which allows sensor deployment at arbitrary locations throughout the computational domain, and (2) a cost-aware optimization framework implemented through `CCQR` that incorporates spatially-heterogeneous installation costs, thereby accounting for regions where sensor deployment incurs higher expenses.

To integrate the diverse constraint formulations detailed in section 3.4 into the sensing framework, we have developed a novel optimization module within Pysensors termed `GQR` (General QR). This approach is based on Algorithm 1 and provides a unified framework for accommodating various geometric and operational constraints in the sensor placement optimization process. Each subroutine detailed in Algorithm 2 is implemented within the `utils` module under the `_norm_calc.py` framework. For instance, the subroutine corresponding to *CONSTRAINTS = RegionConstrainedMax* is realized as the `max_n()` function in `_norm_calc.py`, following a consistent naming convention that maps algorithmic components to their respective implementation functions.

The implementation of spatial constraints within our sensor placement framework requires two fundamental steps: defining the geometric boundaries of the constraint region and identifying computational grid points that reside within these specified boundaries. This functionality is realized through dedicated classes and methods housed within the `_constraints.py` module of the `utils` package. The module encompasses constraint definitions for multiple geometric shapes, including `Circle`, `Ellipse`, `Polygon`, `Parabola`, `Line`, and `Cylinder`, as illustrated in Figure 6.1. For enhanced flexibility, `UserDefinedConstraints` functionality enables users to specify custom constraint geometries through either Python scripts `(.py)` containing shape definitions or mathematical expressions provided as equation

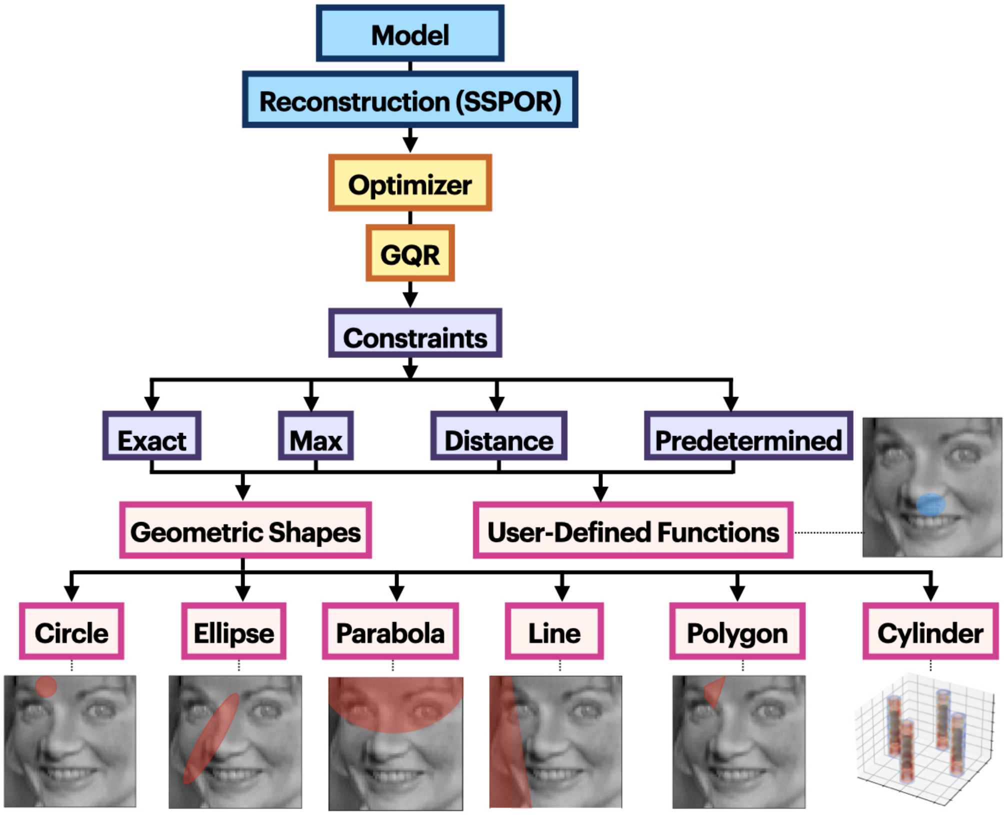

Figure 6.1: Spatial constraint geometries (circle, ellipse, parabola, line, polygon, cylinder and user-defined functions) and associated constraint type (exact,max, distance and predetermined) implemented in Pysensors for constrained flow field reconstruction using the `GQR` algorithm.

strings. The framework accommodates two primary data structures: image-based datasets characterized by pixel coordinates and tabular datasets organized as dataframes with explicit spatial coordinates. During class instantiation, users must supply input `data` in one of these formats: matrix form for image data or structured dataframe for tabular data. For the tabular format, additional keyword arguments `(kwargs)` must specify column identifiers for `X_axis`, `Y_axis`, `Z_axis`, and `Field` parameters, facilitating proper data extraction from the corresponding columns for downstream processing.

Following class instantiation, as demonstrated in the code example of Listing 6.1, several visualization methods become available: `draw_constraint()` renders the constraint geometry, `plot_constraint_on_data()` overlays the constraint region onto a data snapshot, and `plot_grid()` displays all candidate sensor positions. The `get_constraint_indices()` method serves as the core functionality for identifying sensors within constrained regions across different data formats, returning the indices of sensors positioned within the specified spatial boundaries. These indices are subsequently utilized in optimization algorithms to enforce adherence to physical or operational constraints during sensor placement.

Listing 6.1: Constrained sensor selection workflow: (1) Define circular constraint with center at (20,5) and radius 5, (2) Apply Generalized QR (GQR) optimization to select optimal sensor locations within the constraint, (3) Fit SSPOR model with SVD basis, and (4) Visualize selected sensors with constraint overlay.

```
circle = ps.utils._constraints.Circle(center_x = 20, center_y = 5, radius = 5,
     loc = 'in', data = X_train)
circle.draw_constraint()
circle.plot_constraint_on_data(plot_type='image')
circle.plot_grid(all_sensors=all_sensors)
const_idx, rank = circle.get_constraint_indices(all_sensors =
    all_sensors_unconst,info= X_train)
s = 4
optimizer = ps.optimizers.GQR()
optimizer_kwargs={'idx_constrained':const_idx,
          'n_sensors': r,
          'n_const_sensors': s,
          'all_sensors':all_sensors,
          'constraint_option':"exact_n"}
basis = ps.basis.SVD(n_basis_modes=n_sensors)
model = ps.SSPOR(basis = basis, optimizer = optimizer, n_sensors = r)
model.fit(X_train,**optimizer_kwargs)
top_sensors = model.get_selected_sensors()
dataframe = circle.sensors_dataframe(sensors = top_sensors)
```

```
circle.plot_constraint_on_data(plot_type='image')
circle.plot_selected_sensors(sensors = top_sensors, all_sensors = all_sensors)
circle.annotate_sensors(sensors = top_sensors, all_sensors = all_sensors)
```

The implementation shown in Listing 6.1 illustrates the application of the `General QR (GQR)` optimizer for managing spatial constraints through the `constraint_option` = `exact_n` parameter, which enforces the placement of precisely $s = 4$ sensors within the designated constraint region. Critical optimization parameters are conveyed through the `optimizer_kwargs` dictionary, encompassing constrained indices `(idx_constrained)`, total sensor count `(n_sensors)`, constrained sensor quantity `(n_const_sensors)`, complete sensor location set `(all_sensors)`, and the constraint specification. The `SSPOR` model incorporates both the basis functions and optimizer, with model training performed on the input dataset `X_train` using the designated optimizer parameters, resulting in optimal sensor configurations that achieve equilibrium between reconstruction fidelity and spatial constraint compliance.

Upon completion of the optimization process, the algorithm determines the optimal sensor configuration through the `get_selected_sensors()` function, which produces a sensor subset `(top_sensors)` identified as most effective under the given constraints. These selected sensors can be organized into a structured dataframe using the `sensors_dataframe()` method for comprehensive analysis. Visualization of the constraint configuration is accomplished via the `plot_constraint_on_data()` method, which creates a graphical representation overlaying constraint boundaries onto the underlying data field. For comparative evaluation purposes, the `plot_selected_sensors()` method provides visual distinction between optimal sensor positions and the complete sensor array, while the `annotate_sensors()` method applies descriptive metadata labels to individual sensor locations, facilitating straightforward interpretation of optimization outcomes.

6.1.2 RAVEN

RAVEN [148] represents a comprehensive software framework designed for conducting parametric and stochastic analyses through the evaluation of complex system code responses such as StarCCM+[125] or the Reactor Excursion and Leak Analysis Program (RELAP5-3D) [137]. The framework's flexible Application Programming Interfaces (APIs) enable seamless integration with any computational code, provided that perturbable parameters remain accessible through input files or Python interfaces. Given RAVEN's established role in complex system analysis and its proven ability to handle high-dimensional parameter spaces, the integration of constrained sensing functionality represents a natural and valuable extension to its capabilities. Constrained sensing algorithms can significantly enhance RAVEN's monitoring and characterization capabilities by providing optimal sensor placement strategies that respect physical, economic, and operational limitations.

Although RAVEN is built on a Python foundation, its XML input format ensures accessibility for non-programming users, including experimentalists and domain specialists, who can configure complex analyses through structured markup without requiring coding proficiency. Sensor placement has been included as `SparseSensing` into the `ravenframework` as a `PostProcessor` module within the `Models` component. Under the hood `SparseSensing` leverages the `Pysensors` package to perform sensor placement optimization operations. Users specify sparse sensing parameters through structured XML input files. More information on this can be found in [148]. We demonstrate the `SparseSensing` postprocessor in the Listing 6.2 block below.

Listing 6.2: XML configuration for SparseSensing PostProcessor in RAVEN framework. The configuration specifies a reconstruction goal using SVD basis with 4 modes, QR optimization for placing 4 sensors, and temperature field reconstruction based on spatial coordinates (X, Y) and temperature features.

```
<Models>
<PostProcessor name=”mySPSL” subType=”SparseSensing” verbosity=”debug”>
  <Goal subType=”reconstruction”>
```

```
      <features>X (m),Y (m),Temperature (K)</features>
      <target>Temperature (K)</target>
      <basis>SVD</basis>
      <nModes>4</nModes>
      <nSensors>4</nSensors>
      <optimizer>QR</optimizer>
    </Goal>
  </PostProcessor>
</Models>
```

The XML configuration defines a `PostProcessor` with subType `SparseSensing` and debug-level verbosity for comprehensive output logging. The `Goal` element specifies whether the sensor placement objective is `reconstruction` or `classification` of the target field. The `features` tag identifies the spatial coordinates and field variable (X (m), Y (m), Temperature (K)), while the `target` element designates the reconstruction variable of interest (Temperature (K)). The dimensionality reduction approach is defined by the `basis` element set to `SVD` (Singular Value Decomposition), with `nModes` specifying the number of basis functions (4) to retain for reconstruction. The sensor placement strategy is controlled through `nSensors` (4 sensors) and `optimizer` (QR decomposition), establishing the algorithmic framework for optimal sensor selection within the specified spatial domain. Upon execution of the XML configuration, the output produces a dataframe containing the optimal sensor coordinates and corresponding target field values at those locations, along with a visualization displaying the selected sensor positions overlaid on a field snapshot.

6.2 Outlook

While we have established foundational steps—optimizing sensors under spatial constraints, providing uncertainty bounds, and classifying power profiles from temperature fields—significant challenges remain. Our current reconstruction and sensor placement techniques are limited to linear approaches and do not address critical control procedures needed once measurements are obtained, particularly during anomalous or transient conditions. The following sections outline our roadmap for addressing these limitations and advancing toward a complete monitoring and control framework.

6.2.1 Extension to non-linear sensor optimization

In this thesis, we focus on sensor placement strategies guided by linear reduced-order models and reconstruction methods to reconstruct flow fields and classify control inputs driving the observed dynamics. These linear methods are adequate for the problems discussed above, offering uncertainty estimation and interpretability, particularly for reactor commissioning and testing. However, some real-world systems exhibit inherent nonlinearity, whereas existing approaches to feature selection and sensor placement typically rely on linearity assumptions or overly simplistic statistical models. Otto et al. highlight that when these assumptions fail, conventional techniques may lead to unnecessary sensing costs without guaranteeing the recovery of the desired information from the measurements. [149].

Mutual information is a powerful statistical measure that quantifies the total correlation between variables, capturing both linear and nonlinear relationships. Unlike traditional correlation measures, which may only identify linear dependencies, mutual information provides a more comprehensive view by accounting for all types of statistical dependencies, including nonlinear ones [150]. This makes it an invaluable tool for understanding the intricate relationships between variables [151]. Some studies have leveraged mutual information for sensor placement, recognizing its potential to optimize sensor configurations based on the amount of shared information. However, many of these approaches assume an underlying Gaussian distribution due to the computational complexity of directly calculating mutual information, particularly for high-dimensional systems [3, 152, 153]. As a result, despite its theoretical advantages, practical implementations often simplify or approximate the problem to make it more tractable.

Belghazi et al [154] developed an alternative approach using the Mutual Information Neural Estimator (MINE), that estimates mutual information between high-dimensional continuous random variables, through gradient descent optimization on neural networks.

A future direction for sensing would be to develop an innovative nonlinear framework for sensor placement and field reconstruction, leveraging mutual information as the optimization criterion. This is a critical metric for evaluating sensor configurations as it captures nonlinear correlations between selected sensors and unmeasured locations. To address this, we designed an alternative approach using the Mutual Information Neural Estimator (MINE), which involves training a neural network across various sensor configurations. This method enables the identification of optimal sensor placements, even in cases where measured locations do not capture the highest signal variance, necessitating nonlinear reconstruction. This framework opens new possibilities for efficient, data-driven sensor placement in complex, high-dimensional systems.

6.2.2 Extension to real-time control for digital twins

Real-time control decisions, such as optimizing dispatch in an integrated energy system based on sensor data from wind and solar production, are essential for maximizing nuclear profitability while ensuring a safe and reliable power supply. Interpretable data-driven models enable the digital twin to analyze this complex data effectively, providing actionable insights for efficient, cost-effective operations. Determining optimal dispatch configurations further enhances the digital twin's ability to guide operational strategies, as the transparency of the models ensures that engineers understand the reasoning behind recommendations, fostering trust and facilitating implementation. These elements are essential to unlocking the full potential of digital twinning in nuclear-integrated energy systems, ensuring both profitability and reliability are achieved through informed, data-driven decisions. We have developed a reinforcement learning-based controller to optimize energy dispatch within an integrated energy system, using both historical and synthetic data from the Electric Reliability Council of Texas (ERCOT) on solar and wind generation, grid demand, and electricity prices. The agent is trained on synthetic data and tested on real-time data to ensure reliable, optimal dispatch decisions. Additionally, seasonal trends in wind, solar, and demand outputs are incorporated to enable the agent to make more informed decisions that respect the underlying dynamics of the data. To enhance interpretability, the controller generates mappings between grid demand, wind generation levels, and the corresponding energy drawn from thermal energy storage. These mappings make the digital twin's dispatch decisions transparent and comprehensible for human operators, supporting more effective real-time decision-making.

BIBLIOGRAPHY

[1] Zhe Dong, Zhonghua Cheng, Yunlong Zhu, Xiaojin Huang, Yujie Dong, and Zuoyi Zhang. “Review on the recent progress in nuclear plant dynamical modeling and control”. In: *Energies* 16.3 (2023), p. 1443.

[2] Samuel E Otto. *Advances in data-driven modeling and sensing for high-dimensional nonlinear systems*. Princeton University, 2022.

[3] Andreas Krause, Ajit Singh, and Carlos Guestrin. “Near-optimal sensor placements in Gaussian processes: Theory, efficient algorithms and empirical studies.” In: *Journal of Machine Learning Research* 9.2 (2008).

[4] Siddharth Joshi and Stephen Boyd. “Sensor selection via convex optimization”. In: *IEEE Transactions on Signal Processing* 57.2 (2008), pp. 451–462.

[5] Tyler H Summers, Fabrizio L Cortesi, and John Lygeros. “On submodularity and controllability in complex dynamical networks”. In: *IEEE Transactions on Control of Network Systems* 3.1 (2015), pp. 91–101.

[6] Bingni W Brunton, Steven L Brunton, Joshua L Proctor, and J Nathan Kutz. “Sparse sensor placement optimization for classification”. In: *SIAM Journal on Applied Mathematics* 76.5 (2016), pp. 2099–2122.

[7] Kevin K Chen and Clarence W Rowley. “H2 optimal actuator and sensor placement in the linearised complex Ginzburg–Landau system”. In: *Journal of Fluid Mechanics* 681 (2011), pp. 241–260.

[8] B Yildirim, C Chryssostomidis, and GE Karniadakis. “Efficient sensor placement for ocean measurements using low-dimensional concepts”. In: *Ocean Modelling* 27.3-4 (2009), pp. 160–173.

[9] Karen Willcox. “Unsteady flow sensing and estimation via the gappy proper orthogonal decomposition”. In: *Computers & fluids* 35.2 (2006), pp. 208–226.

[10] Maxime Barrault, Yvon Maday, Ngoc Cuong Nguyen, and Anthony T Patera. “An ‘empirical interpolation’method: application to efficient reduced-basis discretization of partial differential equations”. In: *Comptes Rendus Mathematique* 339.9 (2004), pp. 667–672.

[11] Saifon Chaturantabut and Danny C Sorensen. “Nonlinear model reduction via discrete empirical interpolation”. In: *SIAM Journal on Scientific Computing* 32.5 (2010), pp. 2737–2764.

[12] Zlatko Drmac and Serkan Gugercin. “A new selection operator for the discrete empirical interpolation method—improved a priori error bound and extensions”. In: *SIAM Journal on Scientific Computing* 38.2 (2016), A631–A648.

[13] Krithika Manohar, Bingni W Brunton, J Nathan Kutz, and Steven L Brunton. “Data-driven sparse sensor placement for reconstruction: Demonstrating the benefits of exploiting known patterns”. In: *IEEE Control Systems Magazine* 38.3 (2018), pp. 63–86.

[14] Krithika Manohar, Thomas Hogan, Jim Buttrick, Ashis G Banerjee, J Nathan Kutz, and Steven L Brunton. “Predicting shim gaps in aircraft assembly with machine learning and sparse sensing”. In: *Journal of manufacturing systems* 48 (2018), pp. 87–95.

[15] Krithika Manohar, J Nathan Kutz, and Steven L Brunton. “Optimal sensor and actuator selection using balanced model reduction”. In: *IEEE Transactions on Automatic Control* 67.4 (2021), pp. 2108–2115.

[16] Emily Clark, Travis Askham, Steven L Brunton, and J Nathan Kutz. “Greedy sensor placement with cost constraints”. In: *IEEE sensors journal* 19.7 (2018), pp. 2642–2656.

[17] Dirk Hartmann, Matthias Herz, and Utz Wever. “Model order reduction a key technology for digital twins”. In: *Reduced-order modeling (ROM) for simulation and optimization.* Springer, 2018, pp. 167–179.

[18] Zhaojun Bai, Patrick M Dewilde, and Roland W Freund. “Reduced-order modeling”. In: *Handbook of numerical analysis* 13 (2005), pp. 825–895.

[19] Pankaj Wahi and Vivek Kumawat. “Nonlinear stability analysis of a reduced order model of nuclear reactors: A parametric study relevant to the advanced heavy water reactor”. In: *Nuclear engineering and design* 241.1 (2011), pp. 134–143.

[20] Dongli Huang, Hany Abdel-Khalik, Cristian Rabiti, and Frederick Gleicher. “Dimensionality reducibility for multi-physics reduced order modeling”. In: *Annals of Nuclear Energy* 110 (2017), pp. 526–540.

[21] Lawrence Sirovich. “Turbulence and the dynamics of coherent structures. I. Coherent structures”. In: *Quarterly of applied mathematics* 45.3 (1987), pp. 561–571.

[22] Karen Willcox and Jaime Peraire. “Balanced model reduction via the proper orthogonal decomposition”. In: *AIAA journal* 40.11 (2002), pp. 2323–2330.

[23] Bernd R Noack, Konstantin Afanasiev, MAREK MORZYŃSKI, Gilead Tadmor, and Frank Thiele. “A hierarchy of low-dimensional models for the transient and post-transient cylinder wake”. In: *Journal of Fluid Mechanics* 497 (2003), pp. 335–363.

[24] Jean-Christophe Loiseau, Bernd R Noack, and Steven L Brunton. “Sparse reduced-order modelling: sensor-based dynamics to full-state estimation”. In: *Journal of Fluid Mechanics* 844 (2018), pp. 459–490.

[25] Clarence W Rowley. “Model reduction for fluids, using balanced proper orthogonal decomposition”. In: *International Journal of Bifurcation and Chaos* 15.03 (2005), pp. 997–1013.

[26] Mohammad Abdo, Rabab Elzohery, and Jeremy A Roberts. “Modeling isotopic evolution with surrogates based on dynamic mode decomposition”. In: *Annals of Nuclear Energy* 129 (2019), pp. 280–288.

[27] R Elzohery, M Abdo, and J Roberts. “Comparison between gaussian processes and dmd surrogates for isotopic composition prediction”. In: *Transactions of the American Nuclear Society* 118 (2018), pp. 459–462.

[28] Mohammad Abdo, Rabab Elzohery, and Jeremy A Roberts. “Analysis of the LRA Reactor Benchmark Using Dynamic Mode Decomposition”. In: *Trans. Am. Nucl. Soc* 119 (2018), p. 683.

[29] Christian Franzke, Andrew J Majda, and Eric Vanden-Eijnden. “Low-order stochastic mode reduction for a realistic barotropic model climate”. In: *Journal of the atmospheric sciences* 62.6 (2005), pp. 1722–1745.

[30] DT Crommelin and AJ Majda. “Strategies for model reduction: Comparing different optimal bases”. In: *Journal of the Atmospheric Sciences* 61.17 (2004), pp. 2206–2217.

[31] Tilmann Wittig, Rolf Schuhmann, and Thomas Weiland. “Model order reduction for large systems in computational electromagnetics”. In: *Linear algebra and its applications* 415.2-3 (2006), pp. 499–530.

[32] S Koziel and S Ogurtsov. “Model management for cost-efficient surrogate-based optimisation of antennas using variable-fidelity electromagnetic simulations”. In: *IET Microwaves, Antennas & Propagation* 6.15 (2012), pp. 1643–1650.

[33] Serhat Yeşilyurt and Anthony T. Patera. “Surrogates for numerical simulations; optimization of eddy-promoter heat exchangers”. In: *Computer methods in applied mechanics and engineering* 121.1-4 (1995), pp. 231–257.

[34] HM Park and DH Cho. “The use of the Karhunen-Loeve decomposition for the modeling of distributed parameter systems”. In: *Chemical Engineering Science* 51.1 (1996), pp. 81–98.

[35] Richard Everson and Lawrence Sirovich. "Karhunen–Loeve procedure for gappy data". In: *JOSA A* 12.8 (1995), pp. 1657–1664.

[36] Bruce Moore. "Principal component analysis in linear systems: Controllability, observability, and model reduction". In: *IEEE transactions on automatic control* 26.1 (1981), pp. 17–32.

[37] Jer-Nan Juang and Richard S Pappa. "An eigensystem realization algorithm for modal parameter identification and model reduction". In: *Journal of guidance, control, and dynamics* 8.5 (1985), pp. 620–627.

[38] Mikhail Belkin and Partha Niyogi. "Laplacian eigenmaps for dimensionality reduction and data representation". In: *Neural computation* 15.6 (2003), pp. 1373–1396.

[39] Bernard O Koopman and J v Neumann. "Dynamical systems of continuous spectra". In: *Proceedings of the National Academy of Sciences* 18.3 (1932), pp. 255–263.

[40] Diederik P Kingma, Max Welling, et al. *Auto-encoding variational bayes.* 2013.

[41] M Grieves. "Digital Twin: Manufacturing Excellence through Virtual Factory Replication-A Whitepaper by Dr. Michael Grieves". In: *White Pap* (2015), pp. 1–7.

[42] Michael Grieves and John Vickers. "Digital twin: Mitigating unpredictable, undesirable emergent behavior in complex systems". In: *Transdisciplinary perspectives on complex systems.* Springer, 2017, pp. 85–113.

[43] Edward Glaessgen and David Stargel. "The digital twin paradigm for future NASA and US Air Force vehicles". In: *53rd AIAA/ASME/ASCE/AHS/ASC structures, structural dynamics and materials conference 20th AIAA/ASME/AHS adaptive structures conference 14th AIAA.* 2012, p. 1818.

[44] M Shafto, M Conroy, R Doyle, E Glaessgen, C Kemp, J LeMoigne, and L Wang. *NASA technology roadmap: modeling, simulation, information technology & processing roadmap technology area 11.* 2010.

[45] Eric J Tuegel, Anthony R Ingraffea, Thomas G Eason, and S Michael Spottswood. "Reengineering aircraft structural life prediction using a digital twin". In: *International Journal of Aerospace Engineering* 2011 (2011).

[46] Eric Tuegel. "The airframe digital twin: some challenges to realization". In: *53rd AIAA/ASME/ASCE/AHS/ASC structures, structural dynamics and materials conference 20th AIAA/ASME/AHS adaptive structures conference 14th AIAA*. 2012, p. 1812.

[47] Fei Tao, He Zhang, Ang Liu, and Andrew YC Nee. "Digital twin in industry: State-of-the-art". In: *IEEE Transactions on industrial informatics* 15.4 (2018), pp. 2405–2415.

[48] Christophe Varé and Patrick Morilhat. "Digital twins, a new step for long term operation of nuclear power plants". In: *Engineering Assets and Public Infrastructures in the Age of Digitalization*. Springer, 2020, pp. 96–103.

[49] Houde Song, Meiqi Song, and Xiaojing Liu. "Online autonomous calibration of digital twins using machine learning with application to nuclear power plants". In: *Applied Energy* 326 (2022), p. 119995.

[50] Linyu Lin, Han Bao, and Nam Dinh. "Uncertainty quantification and software risk analysis for digital twins in the nearly autonomous management and control systems: A review". In: *Annals of Nuclear Energy* 160 (2021), p. 108362.

[51] Adil Rasheed, Omer San, and Trond Kvamsdal. "Digital twin: Values, challenges and enablers from a modeling perspective". In: *Ieee Access* 8 (2020), pp. 21980–22012.

[52] J-P Argaud, Bertrand Bouriquet, F De Caso, Helin Gong, Yvon Maday, and Olga Mula. "Sensor placement in nuclear reactors based on the generalized empirical interpolation method". In: *Journal of Computational Physics* 363 (2018), pp. 354–370.

[53] Siyao Gu and Miltiadis Alamaniotis. “Radiation Sensor Placement using Reinforcement Learning in Nuclear Security Applications”. In: *2022 13th International Conference on Information, Intelligence, Systems & Applications (IISA)*. IEEE. 2022, pp. 1–6.

[54] Belle R Upadhyaya and Fan Li. “Optimal sensor placement strategy for anomaly detection and isolation”. In: *2011 Future of Instrumentation International Workshop (FIIW) Proceedings*. IEEE. 2011, pp. 95–98.

[55] Bernd R Noack, Marek Morzynski, and Gilead Tadmor. *Reduced-order modelling for flow control*. Vol. 528. Springer Science & Business Media, 2011.

[56] Mengnan Liu, Shuiliang Fang, Huiyue Dong, and Cunzhi Xu. “Review of digital twin about concepts, technologies, and industrial applications”. In: *Journal of Manufacturing Systems* 58 (2021), pp. 346–361.

[57] Hossein Darvishi, Domenico Ciuonzo, Eivind Roson Eide, and Pierluigi Salvo Rossi. “Sensor-fault detection, isolation and accommodation for digital twins via modular data-driven architecture”. In: *IEEE Sensors Journal* 21.4 (2020), pp. 4827–4838.

[58] Mariví Tello Alonso, Paco López-Dekker, and Jordi J Mallorquí. “A novel strategy for radar imaging based on compressive sensing”. In: *IEEE Transactions on Geoscience and Remote Sensing* 48.12 (2010), pp. 4285–4295.

[59] Yanwu Zhang and James G Bellingham. “An efficient method of selecting ocean observing locations for capturing the leading modes and reconstructing the full field”. In: *Journal of Geophysical Research: Oceans* 113.C4 (2008).

[60] Xiu Yang, Daniele Venturi, Changsheng Chen, Chryssostomos Chryssostomidis, and George Em Karniadakis. “EOF-based constrained sensor placement and field reconstruction from noisy ocean measurements: Application to Nantucket Sound”. In: *Journal of Geophysical Research: Oceans* 115.C12 (2010).

[61] Thomas L Mohren, Thomas L Daniel, Steven L Brunton, and Bingni W Brunton. "Neural-inspired sensors enable sparse, efficient classification of spatiotemporal data". In: *Proceedings of the National Academy of Sciences* 115.42 (2018), pp. 10564–10569.

[62] Tyler H Summers and John Lygeros. "Optimal sensor and actuator placement in complex dynamical networks". In: *IFAC Proceedings Volumes* 47.3 (2014), pp. 3784–3789.

[63] Vasileios Tzoumas, Luca Carlone, George J Pappas, and Ali Jadbabaie. "LQG control and sensing co-design". In: *IEEE Transactions on Automatic Control* 66.4 (2020), pp. 1468–1483.

[64] Romain Paris, Samir Beneddine, and Julien Dandois. "Robust flow control and optimal sensor placement using deep reinforcement learning". In: *Journal of Fluid Mechanics* 913 (2021), A25.

[65] Satoshi Shimomura, Satoshi Sekimoto, Akira Oyama, Kozo Fujii, and Hiroyuki Nishida. "Closed-loop flow separation control using the deep Q network over airfoil". In: *AIAA Journal* 58.10 (2020), pp. 4260–4270.

[66] Caterina Bigoni, Zhenying Zhang, and Jan S Hesthaven. "Systematic sensor placement for structural anomaly detection in the absence of damaged states". In: *Computer Methods in Applied Mechanics and Engineering* 371 (2020), p. 113315.

[67] Mahdi Jamei, Anna Scaglione, Ciaran Roberts, Emma Stewart, Sean Peisert, Chuck McParland, and Alex McEachern. "Anomaly Detection Using Optimally Placed μPMU Sensors in Distribution Grids". In: *IEEE Transactions on Power Systems* 33.4 (2017), pp. 3611–3623.

[68] Xue-Yang Pei, Ting-Hua Yi, Chun-Xu Qu, and Hong-Nan Li. "Conditional information entropy based sensor placement method considering separated model error and measurement noise". In: *Journal of Sound and Vibration* 449 (2019), pp. 389–404.

[69] Liam Paninski. “Asymptotic theory of information-theoretic experimental design”. In: *Neural Computation* 17.7 (2005), pp. 1480–1507.

[70] Shuo Wang, Xiaonan Lai, Xiwang He, Kunpeng Li, Liye Lv, and Xueguan Song. “Optimal sensor placement for digital twin based on mutual information and correlation with multi-fidelity data”. In: *Engineering with Computers* (2023), pp. 1–20.

[71] William F Caselton and James V Zidek. “Optimal monitoring network designs”. In: *Statistics & Probability Letters* 2.4 (1984), pp. 223–227.

[72] Xiao Lin, Asif Chowdhury, Xiaofan Wang, and Gabriel Terejanu. “Approximate computational approaches for Bayesian sensor placement in high dimensions”. In: *Information Fusion* 46 (2019), pp. 193–205.

[73] David L Donoho. “Compressed sensing”. In: *IEEE Transactions on information theory* 52.4 (2006), pp. 1289–1306.

[74] Emmanuel J Candes and Terence Tao. “Near-optimal signal recovery from random projections: Universal encoding strategies?” In: *IEEE transactions on information theory* 52.12 (2006), pp. 5406–5425.

[75] Vahab Akbarzadeh, Christian Gagné, Marc Parizeau, and Mir Abolfazl Mostafavi. “Black-box optimization of sensor placement with elevation maps and probabilistic sensing models”. In: *2011 IEEE International Symposium on Robotic and Sensors Environments (ROSE)*. IEEE. 2011, pp. 89–94.

[76] Haotian Zhang, Raid Ayoub, and Shreyas Sundaram. “Sensor selection for Kalman filtering of linear dynamical systems: Complexity, limitations and greedy algorithms”. In: *Automatica* 78 (2017), pp. 202–210.

[77] Sundeep Prabhakar Chepuri and Geert Leus. “Continuous sensor placement”. In: *IEEE signal processing letters* 22.5 (2014), pp. 544–548.

[78] Sijia Liu, Sundeep Prabhakar Chepuri, Makan Fardad, Engin Maşazade, Geert Leus, and Pramod K Varshney. “Sensor selection for estimation with correlated measurement noise”. In: *IEEE Transactions on Signal Processing* 64.13 (2016), pp. 3509–3522.

[79] Fu Lin, Makan Fardad, and Mihailo R Jovanović. “Design of optimal sparse feedback gains via the alternating direction method of multipliers”. In: *IEEE Transactions on Automatic Control* 58.9 (2013), pp. 2426–2431.

[80] Ulrich Münz, Maximilian Pfister, and Philipp Wolfrum. “Sensor and Actuator Placement for Linear Systems Based on H_2 and H_∞ Optimization”. In: *IEEE Transactions on Automatic Control* 59.11 (2014), pp. 2984–2989.

[81] Armin Zare, Hesameddin Mohammadi, Neil K Dhingra, Tryphon T Georgiou, and Mihailo R Jovanović. “Proximal algorithms for large-scale statistical modeling and sensor/actuator selection”. In: *IEEE Transactions on Automatic Control* 65.8 (2019), pp. 3441–3456.

[82] Neil K Dhingra, Mihailo R Jovanović, and Zhi-Quan Luo. “An ADMM algorithm for optimal sensor and actuator selection”. In: *53rd IEEE Conference on Decision and Control*. IEEE. 2014, pp. 4039–4044.

[83] Gal Berkooz, Philip Holmes, and John L Lumley. “The proper orthogonal decomposition in the analysis of turbulent flows”. In: *Annual review of fluid mechanics* 25.1 (1993), pp. 539–575.

[84] Krithika Manohar, Steven L Brunton, and J Nathan Kutz. “Environment identification in flight using sparse approximation of wing strain”. In: *Journal of Fluids and Structures* 70 (2017), pp. 162–180.

[85] Emily Clark, J Nathan Kutz, and Steven L Brunton. “Sensor selection with cost constraints for dynamically relevant bases”. In: *IEEE Sensors Journal* 20.19 (2020), pp. 11674–11687.

[86] Emily Clark, Steven L Brunton, and J Nathan Kutz. "Multi-fidelity sensor selection: Greedy algorithms to place cheap and expensive sensors with cost constraints". In: *IEEE Sensors Journal* 21.1 (2020), pp. 600–611.

[87] Krithika Manohar, Eurika Kaiser, Steven L Brunton, and J Nathan Kutz. "Optimized sampling for multiscale dynamics". In: *Multiscale Modeling & Simulation* 17.1 (2019), pp. 117–136.

[88] Andrei A Klishin, J Nathan Kutz, and Krithika Manohar. "Data-Induced Interactions of Sparse Sensors". In: *arXiv preprint arXiv:2307.11838* (2023).

[89] Katharina Bieker, Sebastian Peitz, Steven L Brunton, J Nathan Kutz, and Michael Dellnitz. "Deep model predictive flow control with limited sensor data and online learning". In: *Theoretical and computational fluid dynamics* 34 (2020), pp. 577–591.

[90] N Benjamin Erichson, Lionel Mathelin, Zhewei Yao, Steven L Brunton, Michael W Mahoney, and J Nathan Kutz. "Shallow neural networks for fluid flow reconstruction with limited sensors". In: *Proceedings of the Royal Society A* 476.2238 (2020), p. 20200097.

[91] Jan Williams, Olivia Zahn, and J Nathan Kutz. "Data-driven sensor placement with shallow decoder networks". In: *arXiv preprint arXiv:2202.05330* (2022).

[92] Jan P Williams, Olivia Zahn, and J Nathan Kutz. "Sensing with shallow recurrent decoder networks". In: *arXiv preprint arXiv:2301.12011* (2023).

[93] Kai Fukami, Romit Maulik, Nesar Ramachandra, Koji Fukagata, and Kunihiko Taira. "Global field reconstruction from sparse sensors with Voronoi tessellation-assisted deep learning". In: *Nature Machine Intelligence* 3.11 (2021), pp. 945–951.

[94] Suhas Lohit, Kuldeep Kulkarni, Ronan Kerviche, Pavan Turaga, and Amit Ashok. "Convolutional neural networks for noniterative reconstruction of compressively sensed images". In: *IEEE Transactions on Computational Imaging* 4.3 (2018), pp. 326–340.

[95] Kai Fukami, Byungjin An, Motohiko Nohmi, Masashi Obuchi, and Kunihiko Taira. "Machine-learning-based reconstruction of turbulent vortices from sparse pressure sensors in a pump sump". In: *Journal of Fluids Engineering* 144.12 (2022), p. 121501.

[96] Kai Fukami, Koji Fukagata, and Kunihiko Taira. "Super-resolution reconstruction of turbulent flows with machine learning". In: *Journal of Fluid Mechanics* 870 (2019), pp. 106–120.

[97] Kai Fukami, Koji Fukagata, and Kunihiko Taira. "Machine-learning-based spatio-temporal super resolution reconstruction of turbulent flows". In: *Journal of Fluid Mechanics* 909 (2021), A9.

[98] Zhaohui Luo, Longyan Wang, Jian Xu, Meng Chen, Jianping Yuan, and Andy CC Tan. "Flow reconstruction from sparse sensors based on reduced-order autoencoder state estimation". In: *Physics of Fluids* 35.7 (2023).

[99] Luning Sun and Jian-Xun Wang. "Physics-constrained bayesian neural network for fluid flow reconstruction with sparse and noisy data". In: *Theoretical and Applied Mechanics Letters* 10.3 (2020), pp. 161–169.

[100] Amirhossein Arzani, Jian-Xun Wang, and Roshan M D'Souza. "Uncovering near-wall blood flow from sparse data with physics-informed neural networks". In: *Physics of Fluids* 33.7 (2021).

[101] Han Gao, Luning Sun, and Jian-Xun Wang. "Super-resolution and denoising of fluid flow using physics-informed convolutional neural networks without high-resolution labels". In: *Physics of Fluids* 33.7 (2021).

[102] Yonghong Zhong, Kai Fukami, Byungjin An, and Kunihiko Taira. "Sparse sensor reconstruction of vortex-impinged airfoil wake with machine learning". In: *Theoretical and Computational Fluid Dynamics* (2023), pp. 1–19.

[103] Jochen Tautges, Arno Zinke, Björn Krüger, Jan Baumann, Andreas Weber, Thomas Helten, Meinard Müller, Hans-Peter Seidel, and Bernd Eberhardt. “Motion reconstruction using sparse accelerometer data”. In: *ACM Transactions on Graphics (ToG)* 30.3 (2011), pp. 1–12.

[104] Mário AT Figueiredo, Robert D Nowak, and Stephen J Wright. “Gradient projection for sparse reconstruction: Application to compressed sensing and other inverse problems”. In: *IEEE Journal of selected topics in signal processing* 1.4 (2007), pp. 586–597.

[105] Ali Girayhan Özbay and Sylvain Laizet. “Deep learning fluid flow reconstruction around arbitrary two-dimensional objects from sparse sensors using conformal mappings”. In: *AIP Advances* 12.4 (2022).

[106] Zhi Wang, Han-Xiong Li, and Chunlin Chen. “Reinforcement learning-based optimal sensor placement for spatiotemporal modeling”. In: *IEEE transactions on cybernetics* 50.6 (2019), pp. 2861–2871.

[107] Jean Rabault, Miroslav Kuchta, Atle Jensen, Ulysse Réglade, and Nicolas Cerardi. “Artificial neural networks trained through deep reinforcement learning discover control strategies for active flow control”. In: *Journal of fluid mechanics* 865 (2019), pp. 281–302.

[108] Konstantinos P Ferentinos and Theodore A Tsiligiridis. “Adaptive design optimization of wireless sensor networks using genetic algorithms”. In: *Computer Networks* 51.4 (2007), pp. 1031–1051.

[109] Shiyuan Jin, Ming Zhou, and Annie S Wu. “Sensor network optimization using a genetic algorithm”. In: *Proceedings of the 7th world multiconference on systemics, cybernetics and informatics.* 2003, pp. 109–116.

[110] Ying Huang, Simone A Ludwig, and Fodan Deng. "Sensor optimization using a genetic algorithm for structural health monitoring in harsh environments". In: *Journal of Civil Structural Health Monitoring* 6 (2016), pp. 509–519.

[111] Pattrick Calderoni, David Hurley, Josh Daw, Austin Fleming, and Kelly McCary. "Innovative sensing technologies for nuclear instrumentation". In: *2019 IEEE International Instrumentation and Measurement Technology Conference (I2MTC)*. 2019, pp. 1–6. DOI: `10.1109/I2MTC.2019.8827129`.

[112] Hashem Mehrdad Hashemian. "On-line monitoring applications in nuclear power plants". In: *Progress in Nuclear Energy* 53.2 (2011), pp. 167–181.

[113] Ting-Han Lin and Shun-Chi Wu. "Sensor fault detection, isolation and reconstruction in nuclear power plants". In: *Annals of nuclear energy* 126 (2019), pp. 398–409.

[114] Brendan Kochunas and Xun Huan. "Digital twin concepts with uncertainty for nuclear power applications". In: *Energies* 14.14 (2021), p. 4235.

[115] Bradley T Rearden and Matthew Anderson Jessee. *SCALE code system.* Tech. rep. Oak Ridge National Lab.(ORNL), Oak Ridge, TN (United States), 2016.

[116] Pradeep Ramuhalli, Guang Lin, Susan L Crawford, Bledar A Konomi, Jamie B Coble, Brent Shumaker, and Hash Hashemian. *Uncertainty quantification techniques for sensor calibration monitoring in nuclear power plants.* Tech. rep. Pacific Northwest National Lab.(PNNL), Richland, WA (United States), 2014.

[117] Morteza Aien, Ali Hajebrahimi, and Mahmud Fotuhi-Firuzabad. "A comprehensive review on uncertainty modeling techniques in power system studies". In: *Renewable and Sustainable Energy Reviews* 57 (2016), pp. 1077–1089.

[118] Ronald Aylmer Fisher. "Design of experiments". In: *British Medical Journal* 1.3923 (1936), p. 554.

[119] Kirstine Smith. “On the standard deviations of adjusted and interpolated values of an observed polynomial function and its constants and the guidance they give towards a proper choice of the distribution of observations”. In: *Biometrika* 12.1/2 (1918), pp. 1–85.

[120] Ashis Sengupta. “Generalized variance”. In: *Encyclopedia of statistical sciences* 3.1 (2004).

[121] Michael Friendly, Georges Monette, and John Fox. “Elliptical insights: understanding statistical methods through elliptical geometry”. In: (2013).

[122] Peter Businger and Gene H Golub. “Linear least squares solutions by Householder transformations”. In: *Numerische Mathematik* 7.3 (1965), pp. 269–276.

[123] Ming Gu and Stanley C Eisenstat. “Efficient algorithms for computing a strong rank-revealing QR factorization”. In: *SIAM Journal on Scientific Computing* 17.4 (1996), pp. 848–869.

[124] Benjamin Peherstorfer, Zlatko Drmac, and Serkan Gugercin. “Stability of discrete empirical interpolation and gappy proper orthogonal decomposition with randomized and deterministic sampling points”. In: *SIAM Journal on Scientific Computing* 42.5 (2020), A2837–A2864.

[125] Siemens Digital Industries Software. *Simcenter STAR-CCM+, version 2021.1.* Version 2021.1. Siemens 2021.

[126] IAEA Nuclear Energy Series. *Core Knowledge on Instrumentation and Control Systems in Nuclear Power Plants. No.* Tech. rep. NP.

[127] Alberto Fernandez Fernandez, Andrei I Gusarov, Benoı t Brichard, Serge Bodart, Koen Lammens, Francis Berghmans, Marc Decreton, Patrice Megret, Michel Blondel, and Alain Delchambre. “Temperature monitoring of nuclear reactor cores with multiplexed fiber Bragg grating sensors”. In: *Optical Engineering* 41.6 (2002), pp. 1246–1254.

[128] A Messai, A Mellit, I Abdellani, and A Massi Pavan. “On-line fault detection of a fuel rod temperature measurement sensor in a nuclear reactor core using ANNs”. In: *Progress in Nuclear Energy* 79 (2015), pp. 8–21.

[129] BR Upadhyaya, SRP Perillo, X Xu, and F Li. “Advanced control design, optimal sensor placement, and technology demonstration for small and medium nuclear power reactors”. In: *International Conference on Nuclear Engineering.* Vol. 43550. 2009, pp. 763–773.

[130] Fan Li and Belle R Upadhyaya. “Design of sensor placement for an integral pressurized water reactor using fault diagnostic observability and reliability criteria”. In: *Nuclear Technology* 173.1 (2011), pp. 17–25.

[131] Rahman Khalil Ur, Jinsoo Shin, Muhammad Zubair, Gyunyoung Heo, Hanseong Son, et al. “Sensitivity study on availability of I&C components using bayesian network”. In: *Science and Technology of Nuclear Installations* 2013 (2013).

[132] Wei Li, Minjun Peng, and Qingzhong Wang. “Improved PCA method for sensor fault detection and isolation in a nuclear power plant”. In: *Nuclear Engineering and Technology* 51.1 (2019), pp. 146–154.

[133] Deog Yeon Oh and Hee Cheon No. “Determination of the minimal number and optimal sensor location in a nuclear system with fixed incore detectors”. In: *Nuclear engineering and design* 152.1-3 (1994), pp. 197–212.

[134] HM Hashemian and Wendell C Bean. “Sensors for next-generation nuclear plants: Fiber-optic and wireless”. In: *Nuclear science and Engineering* 169.3 (2011), pp. 262–278.

[135] Rui He, Guoming Chen, Che Dong, Shufeng Sun, and Xiaoyu Shen. “Data-driven digital twin technology for optimized control in process systems”. In: *ISA transactions* 95 (2019), pp. 221–234.

[136] Niharika Karnik, Mohammad G Abdo, Carlos E Estrada-Perez, Jun Soo Yoo, Joshua J Cogliati, Richard S Skifton, Pattrick Calderoni, Steven L Brunton, and Krithika Manohar. “Constrained optimization of sensor placement for nuclear digital twins”. In: *IEEE Sensors Journal* (2024).

[137] RELAP5-3D© Code Development Team. *RELAP5-3D© Code Manual Volume II: User’s Guide and Input Requirements*. Tech. rep. Idaho National Lab.(INL), Idaho Falls, ID (United States), 2015.

[138] Niharika Karnik, Congjian Wang, Palash K Bhowmik, Joshua J Cogliati, Silvino A Balderrama Prieto, Changhu Xing, Andrei A Klishin, Richard Skifton, Musa Moussaoui, Charles P Folsom, et al. “Leveraging Optimal Sparse Sensor Placement to Aggregate a Network of Digital Twins for Nuclear Subsystems.” In: *Energies (19961073)* 17.13 (2024).

[139] S Curtis Wilkins. *Low cross-section Mo-Nb thermocouples for nuclear application: The state-of-the-art*. Tech. rep. EG and G Idaho, Inc., Idaho Falls, ID (USA), 1988.

[140] Richard Skifton. “High-temperature irradiation-resistant thermocouple instability model for in-pile reactor use”. In: *Frontiers in Energy Research* 11 (2023), p. 1099584.

[141] Fabio De Sousa Ribeiro, Francesco Calivá, Dionysios Chionis, Abdelhamid Dokhane, Antonios Mylonakis, Christophe Demaziere, Georgios Leontidis, and Stefanos Kollias. “Towards a deep unified framework for nuclear reactor perturbation analysis”. In: *2018 IEEE symposium series on computational intelligence (SSCI)*. IEEE. 2018, pp. 120–127.

[142] Khalil Moshkbar-Bakhshayesh and Mohammad B Ghofrani. “Transient identification in nuclear power plants: A review”. In: *Progress in Nuclear Energy* 67 (2013), pp. 23–32.

[143] IK Attieh, AV Gribok, JW Hines, and RE Uhrig. “Pattern recognition techniques for transient detection to enhance nuclear reactors’ operational safety”. In: *Proc. 25th CNS/CNA Annu. Student Conf.* 2000.

[144] Yair Bartal, Jie Lin, and Robert E Uhrig. “Nuclear power plant transient diagnostics using artificial neural networks that allow “don’t-know” classifications”. In: *Nuclear Technology* 110.3 (1995), pp. 436–449.

[145] Joshua L Proctor, Steven L Brunton, and J Nathan Kutz. “Dynamic mode decomposition with control”. In: *SIAM Journal on Applied Dynamical Systems* 15.1 (2016), pp. 142–161.

[146] Jasmine H Bekkaye and Navid H Jafari. “Application and comparison of remote sensing techniques for data-driven disaster debris quantification”. In: *International Journal of Remote Sensing* 45.8 (2024), pp. 2808–2831.

[147] Brian M de Silva, Krithika Manohar, Emily Clark, Bingni W Brunton, Steven L Brunton, and J Nathan Kutz. “PySensors: A Python package for sparse sensor placement”. In: *arXiv preprint arXiv:2102.13476* (2021).

[148] Cristian Rabiti, Andrea Alfonsi, Diego Mandelli, Joshua J Cogliati, Congjian Wang, Paul W Talbot, Daniel P Malijovec, Robert A Kinoshita, Mohammad Gamal Abdo, Sonat Sen, et al. *RAVEN user manual.* Tech. rep. Idaho National Lab.(INL), Idaho Falls, ID (United States), 2021.

[149] Samuel E Otto and Clarence W Rowley. “Inadequacy of linear methods for minimal sensor placement and feature selection in nonlinear systems: a new approach using secants”. In: *Journal of Nonlinear Science* 32.5 (2022), p. 69.

[150] Justin B Kinney and Gurinder S Atwal. “Equitability, mutual information, and the maximal information coefficient”. In: *Proceedings of the National Academy of Sciences* 111.9 (2014), pp. 3354–3359.

[151] Liam Paninski. "Estimation of entropy and mutual information". In: *Neural computation* 15.6 (2003), pp. 1191–1253.

[152] Brian J Julian, Sertac Karaman, and Daniela Rus. "On mutual information-based control of range sensing robots for mapping applications". In: *The International Journal of Robotics Research* 33.10 (2014), pp. 1375–1392.

[153] Chongjun Ouyang, Yuanwei Liu, Hongwen Yang, and Naofal Al-Dhahir. "Integrated sensing and communications: A mutual information-based framework". In: *IEEE Communications Magazine* 61.5 (2023), pp. 26–32.

[154] Mohamed Ishmael Belghazi, Aristide Baratin, Sai Rajeshwar, Sherjil Ozair, Yoshua Bengio, Aaron Courville, and Devon Hjelm. "Mutual information neural estimation". In: *International conference on machine learning*. PMLR. 2018, pp. 531–540.

[155] Panos Y Papalambros and Douglass J Wilde. *Principles of optimal design: modeling and computation*. Cambridge university press, 2000.

[156] Steven L Brunton, J Nathan Kutz, Krithika Manohar, Aleksandr Y Aravkin, Kristi Morgansen, Jennifer Klemisch, Nicholas Goebel, James Buttrick, Jeffrey Poskin, Adriana W Blom-Schieber, et al. "Data-driven aerospace engineering: reframing the industry with machine learning". In: *AIAA Journal* 59.8 (2021), pp. 2820–2847.

[157] Barbara Rita Barricelli, Elena Casiraghi, and Daniela Fogli. "A survey on digital twin: Definitions, characteristics, applications, and design implications". In: *IEEE access* 7 (2019), pp. 167653–167671.

[158] P Fernandes de Aguiar, B Bourguignon, MS Khots, DL Massart, and R Phan-Than-Luu. "D-optimal designs". In: *Chemometrics and intelligent laboratory systems* 30.2 (1995), pp. 199–210.

[159] Niharika Karnik, Mohammad G Abdo, Carlos E Estrada Perez, Jun Soo Yoo, Joshua J Cogliati, Richard S Skifton, Pattrick Calderoni, Steven L Brunton, and Krithika

Manohar. “Optimal Sensor Placement with Adaptive Constraints for Nuclear Digital Twins”. In: *arXiv preprint arXiv:2306.13637* (2023).

[160] Mohammad Sadegh Khorshidi, Mohammad Reza Nikoo, Narges Taravatrooy, Mojtaba Sadegh, Malik Al-Wardy, and Ghazi Ali Al-Rawas. “Pressure sensor placement in water distribution networks for leak detection using a hybrid information-entropy approach”. In: *Information Sciences* 516 (2020), pp. 56–71.

[161] Alex Krizhevsky, Ilya Sutskever, and Geoffrey E Hinton. “Imagenet classification with deep convolutional neural networks”. In: *Advances in neural information processing systems* 25 (2012).

[162] Ian Goodfellow, Yoshua Bengio, and Aaron Courville. *Deep learning*. MIT press, 2016.

[163] Steven L Brunton, Bernd R Noack, and Petros Koumoutsakos. “Machine learning for fluid mechanics”. In: *Annual review of fluid mechanics* 52 (2020), pp. 477–508.

[164] Franz Aurenhammer and Rolf Klein. “Voronoi Diagrams.” In: *Handbook of computational geometry* 5.10 (2000), pp. 201–290.

[165] georges Voronoi. “New applications of continuous parameters to the theory of quadratic forms. First thesis on some properties of perfect positive quadratic forms.” In: *Journal für die reine und angewandte Mathematik (Crelles Journal)* 1908 (133 1908), pp. 97–102.

[166] Ronald Aylmer Fisher. “Statistical methods for research workers”. In: *Breakthroughs in statistics: Methodology and distribution*. Springer, 1970, pp. 66–70.

[167] Brian M. de Silva, Krithika Manohar, Emily Clark, Bingni W. Brunton, J. Nathan Kutz, and Steven L. Brunton. “PySensors: A Python package for sparse sensor placement”. In: *Journal of Open Source Software* 6.58 (2021), p. 2828. DOI: `10.21105/joss.02828`.

[168] Palash K Bhowmik, Carlos E Estrada Perez, Joshua D Fishler, Silvino A Balderrama Prieto, Isaac D Reichow, Justin T Johnson, Piyush Sabharwall, and James E O'Brien. "Integral and separate effects test facilities to support water cooled small modular reactors: a review". In: *Progress in Nuclear Energy* 160 (2023), p. 104697.

[169] Joshua P Schlegel and PK Bhowmik. "Small modular reactors". In: *Nuclear Power Reactor Designs*. Elsevier, 2024, pp. 283–308.

[170] Hossam H Abdellatif, Palash K Bhowmik, David Arcilesi, and Piyush Sabharwall. "Accident event progression, gaps, and key performance indicators for steam generator tube rupture events in water-cooled SMRs: A review". In: *Progress in Nuclear Energy* 168 (2024), p. 105021.

[171] Hossam H Abdellatif, Walter Ambrosini, David Arcilesi, Palash K Bhowmik, and Piyush Sabharwall. "Flow Instabilities in boiling channels and their suppression methodologies—A review". In: *Nuclear Engineering and Design* 421 (2024), p. 113114.

[172] Cam Binh T Pham, Joe Palmer, Douglas W Marshall, Grant L Hawkes, Dawn M Scates, and Paul A Demkowicz. *AGR-5/6/7 Irradiation Test Final As-Run Report*. Tech. rep. Idaho National Lab.(INL), Idaho Falls, ID (United States), 2021.

[173] Sporian Microsystems, Inc. *ThermalFlow 700*. 2024.

[174] Kadierdan Kaheman, Eurika Kaiser, Benjamin Strom, J Nathan Kutz, and Steven L Brunton. "Learning discrepancy models from experimental data". In: *arXiv preprint arXiv:1909.08574* (2019).

[175] Megan R Ebers, Katherine M Steele, and J Nathan Kutz. "Discrepancy modeling framework: Learning missing physics, modeling systematic residuals, and disambiguating between deterministic and random effects". In: *arXiv preprint arXiv:2203.05164* (2022).

[176] Helin Gong, Sibo Cheng, Zhang Chen, and Qing Li. "Data-enabled physics-informed machine learning for reduced-order modeling digital twin: application to nuclear reactor physics". In: *Nuclear Science and Engineering* 196.6 (2022), pp. 668–693.

[177] AJ Palmer, RS Skifton, M Scervini, DC Haggard, and WD Swank. "Performance of custom-made very high temperature thermocouples in the advanced gas reactor experiment AGR-5/6/7 during irradiation in the advanced test reactor". In: *EPJ Web of Conferences*. Vol. 225. EDP Sciences. 2020, p. 04010.

[178] Michael Smith. *ABAQUS/Standard User's Manual, Version 6.9*. English. United States: Dassault Systèmes Simulia Corp, 2009.